学位論文

Structural and photoelectrochemical behavior of self-assembled Ag/Co nanostructures embedded in TiO_2 thin films

(TiO_2薄膜中の自己組織化Ag/Coナノ構造の構造及び光電気化学特性)

平成25年12 月博士（理学）申請

東京大学大学院理学系研究科

化学専攻

渡部　愛理

Structural and photoelectrochemical behavior of self-assembled Ag/Co nanostructures embedded in TiO_2 thin films

PhD Thesis
2015

Anri Watanabe

Department of Chemistry, School of Science,
The University of Tokyo

Contents

Abstract

Nanocomposite materials composed of metal nanoparticles and a dielectric matrix have attracted significant attention from both fundamental and application aspects because of their unique physical properties. Especially Ag nanostructures are well known as its large optical electric-field enhancement in the visible wavelength region, however, Ag nanoparticles easily and quickly sulfidate and oxidate in air. Recently, it was found that metal nanostructures can be embedded in anatase TiO_2 matrix, Co-TiO_2 and Ag-Co-TiO_2 films, by Pulsed Laser Deposition (PLD) method. I conceived that the Ag-Co-TiO_2 nanocomposite film system would effectively protect Ag nanostructures, which has potential applications in plasmonic devices such as biosensors and photovoltaic cells. The device performance is, in general, sensitive to the shape, size, and distribution of metal nanostructures. Thus, it is important to control the size and density of Ag-Co hybrid nanostructures during film growth.

In this study, I investigated the structural variation of Ag-Co nanostructures in $Ag_xCo_5(TiO_2)_{95}$ nanocomposite films with varying PLD conditions. Ag-Co nanomatch-like structures appeared only at a specific condition, and changed from rod-like to spherical with increasing *x*. A broad Ag LSPR peak systematically shifted to longer wavelengths with increasing *x*. In addition, I proposed the nanocomposite film with Ag-Co nanomatch-like structures embedded in TiO_2 matrix as a promising electrode material: this new structure does not merely protect Ag structure, but fresh Ag can be obtained when

needed.

I indeed made the Ag nanostructurs in contact with a supporting electrolyte, and subsequently observed photocurrent enhanced by plasmonic resonance of Ag nanorods. This Ag-Co-TiO_2 nanocomposite film would be useful in not only photoelectric conversion but also plasmonic sensors.

Chapter 1: General introduction

1-1. Motivation and outline of this work

Recent demand of the clean energy is increasing all over the world due to the shortage of fossil fuel; among many kinds of proposed natural energy, the solar energy is one of the most universally available candidates. To date, numbers of studies on the solar cells have made to improve their light-conversion efficiency, resulting in mass production of practical devices. However, the growth of efficiency is now reaching a plateau, as seen in Si-based solar cells, so that the development of high-efficency devices based on a new concept is highly desired in order to break the present status [M. A. Green, 1993-2014][EERE, 2011]. In this study, I especially focused on plasmonic structures which enhance the surrounding electromagnetic field. Plasmon resonance is an active and rapidly growing research field [J. A. Schuller, 2010], because the noble metal nanoparticles act as an antenna of the light energy, whose wavelength of absorbing/responding light is tunable by the nanostructure or surrounding environment even if the material components are same [K. A. Willets, 2006]. Indeed plasmon resonance has been applied not only to photovoltaic cells [S.Pillai, 2010] but also to highly sensitive optical sensors, lithography, chemical reaction (photo catalytic / organic reactions), lasers, etc [K. Ueno, 2013]. Although there are many kinds of metal showing the plasmonic behaviors, silver (Ag) in particular has large electromagnetic enhancement factor and its optical response is largely affected by the surrounding environment [E. J. Zeman, 1987].

Thus Ag nanoparticles have been extensively investigated with particular expectation for applicability to solar cells and biosensors. However Ag nanoparticles with large surface areas have a serious problem of chemical deterioration, similarly to cupper (Cu): the surface is easily to be sulfurized or oxidized in ambient atmosphere [T. E. Graedel, 1992]. It has been believed that silver is not suitable for practical uses in spite of the best performances; moreover the use of Ag nanoparticles is limited to the researchers who can prepare Ag nanoparticles just prior to their use because of the rapid deterioration in the time scale of a few days.

The aims of this study are to establish a technique for preparing Ag nanostructures that are protected from surface deterioration and to demonstrate their potential use in photoelectric conversion. Recently it was found that Ag nanostructures can be embedded in TiO_2 matrix by ablating a mixture target of Ag_2O, CoO, and TiO_2 using pulsed laser deposition (PLD) equipment [K. Ikemiya, 2014]. I decided to utilize this Ag-Co-TiO_2 nanocomposite films because of the following two reasons: firstly the combined system of TiO_2 and noble metal nanoparticles such as gold and silver is known to work as a plasmonic cell in the visible region. The other reason is that the Ag nanoparticles fabricated by PLD are expected to be more firmly sealed by the dielectric matrix than those by the conventional methods; in case of the metal nanoparticles prepared by the conventional methods, such as sol-gel method, an additional coating process is needed to protect them. Compared with such sequential methods in which Ag

nanoparticles are exposed to external air for a while, the PLD method can provide Ag nanoparticles automatically covered with TiO_2 matrix. However, few studies have been reported on the structural control of composite film during thin film deposition because of its experimental difficulty.

This motivated me to investigate Ag-Co-TiO_2 composite films, in which characteristic nanostructures composed of Ag and Co were reported to be buried in the TiO_2 matrix. I have attempted to regulate the sizes and shapes of Ag/Co nanostructures by thin film growth conditions and, as a result, I established a process to fabricate well-protected self-assembled Ag nanorods structure embedded in TiO_2 anatase matrix in a reproducible manner. Next I applied the Ag-Co-TiO_2 films containing Ag nanorods to a plasmonic photovoltaic cell. So far, researchers persuing high-efficiency solar cells have combined the plasmonic enhancement with conventional semiconductor or organic solar cells. In this study, I utilized the Ag-Co-TiO_2 system as an electrode in the solar cell. This photoelectrochemical study on Ag-Co-TiO_2 films revealed that the Ag nanostructures did not work while protected, whereas clear photoelectric conversion was observed after the Ag nanostructures were exposed to outer solution. Here I have developed the procedure to activate, i.e., ‘unseal’, the protected, i.e., ‘sealed’ Ag nanoparticles for the first time. This study paved the way for easy handling of Ag nanostructures, including preservation, portability, and unsealing of the Ag nanostructures, which will be effective in photovoltaic cells and biological sensors.

1-2. Localized Surface Plasmon Resonance (LSPR)

1-2-1. History

Nowadays, plasmonics is one of the most attractive research topics in nanophotonics. It opened the way to confine the light below the diffraction limit of light. Although the history of the plasmonic is old, the number of the researches on the interaction between the metal particles and the optical field is rapidly increasing.

More than 100 years ago, both theoretical and experimental approaches were reported about the electromagnetic field on metal. Gustav Mie solved the Maxwell equation [G. Mie, 1908], showing the behavior of plain wave scattering by the spherical particles theoretically. The parameters used in the theory were the size of spheres, and the relative dielectric function of sphere against that of the media. The theory explained the color of metallic colloid solutions. As is well known, gold nanospheres were used as a “vivid red pigment” of stained glass in churches in the Middle ages. However it is not until that nanoparticles having more complex shapes were practically utilized that computational analysis methods for electromagnetic properties of nanostructures were well developed.

At the same age of Mie theory, Wood experimentally found the phenomenon called anomalies [R. W. Wood, 1902]: the diffraction spectra had unexpected blight/dark bands, when the intensity variable light was introduced into the metal gratings. Interestingly, these bands were weakened by scrubbing the grating surface. In addition, this phenomenon was observed only when the polarization

of the introduced light was perpendicular to the lattice of the grating; it was not observed when the polarization was parallel to the lattice. These new bands could not be explained by the conventional diffraction theory. Soon after the findings, Rayleigh tried to describe it theoretically [O. M. Rayleigh, 1907]. He found that the electromagnetic field of diffraction at a certain wavelength showed characteristic anomalies. The wavelength is called “Reyleigh wavelength”, which is shorter than that treated in the Mie scattering theory. The high-order scattered light existed as an evanescent wave propagating along the surface of the grating, and it coupled with the electromagnetic field of metal surface. The band structure, which was not predicted by the original theory, was further studied by several researchers [U. Fano, 1938], [K. Artmann, 1942], [C. H. Palmer, 1961], [B. A. Lippmann, 1954], [A. Hessel, 1965].

Though the physics of small metal particles and metal surface had already been considered in the early 20th century, the field of plasmonics is rapidly progressing in these days. The main reasons for this are possibly as follows. One is that the progress in optical microscope enables us to see small structures with spatial resolution of sub micron scale. Such micron-scale investigations were soon followed by atomic-scale ones using STM [G. Binning, 1982]. These stimulated further microscopic works for improving their resolution. In 1980s Fischer and Pohl invented the near field microscope, and demonstrated that the diffraction limit of light can be overcome through direct observation of Au nanoparticles on Au thin film, [U. C. Fischer, 1989]. Kawata used a metallic

probe tip for near field microscopy, indicating the importance of surface plasmon [Y. Inouye, 1994]. Ebbesen discovered the phenomenon, “extraordinary transmission”, which also captured the interest of researchers in the field of nano-photonics [T. W. Ebbesen, 1998]. As widely known, metal mesh prevents the propagation of electromagnetic wave. Conventional theory of Bethe [H. A. Bethe, 1944] showed that the transmittance was proportion to $(r/\lambda)^4$, where r is the radius of the hole. However, when Ebbesen prepared an Ag film with holes smaller than the wavelength of light source, he found that the intensity of the transmitted light at λ = 1370 nm was twice larger than that of the light impinged directly to the holes. The transmittance was enhanced because the electromagnetic field around the holes effectively coupled with incident light. In other words, the hole array worked as not a passive but an active element.

Another reason of the rapid growth of plasmonics is the development of the modern techniques. Nanoscale metal structures are critical in plasmonic phenomena. However, it was not until recently that the micromachining was available. Focused ion beam lithography (FIB) enabled researchers to create fine and precise structures. FIB was first invented in 1970s; when a strong Ga ion beam was focused onto a fine spot of a sample surface through electrostatic lenses in a vacuumed chamber, the sample surface was sputtered. Scanning the focal point of Ga beam resulted in the patterning of arbitrary shapes [R. L. Seliger, 1979]. Therefore FIB technique enabled researchers to make three dimensional nanostructures with complicated shapes or simple structures with

sharp edges.

In addition, not only the nanotechnology but also the specification of computers was drastically improved in the last several decades. So far only models assuming simple shapes for nanostructures were mathematically solved. Calculations for more complicated structures need larger capacity memory devices and larger computation cost. Finite domain time difference (FDTD) and discrete dipole approximation (DDA) are major methods for the plasmonic analysis. The FDTD method, proposed by Yee in 1966, is now popular among the engineering field, since there is no limitation in the shape of the model; the calculation is performed on each spatially divided mesh [K. S. Yee, 1966]. The time dependence of the electromagnetic field can also be deduced. In the DDA method, proposed by Purcell and Pennypacker in 1973, the nanostructure is treated as an assembly of (n) elements, where each element was approximated as a dipole with a certain polarizability [E. M. Purcell, 1973].

1-2-2. Basic of surface plasmon [S. A. Maier, 2007][T. Okamoto, 2010]

In 1950's, the words "Plasmon" appeared in the paper of Pines [D. Pines, 1952], [D. Pines, 1956] and Ritchie [R. H. Ritchie, 1957]. In a bulk metal, conduction electrons move freely, which can be regarded as a kind of plasma. The collective oscillation of the free electrons is called plasmon, when it is quantized. The plasma oscillation frequency, ω_p, is given by

$$\omega_p = \sqrt{\frac{Ne^2}{\varepsilon_0 m}}, \quad (1)$$

where *N* is the electron density, *e* is the electron charge, ε_0 is the vacuum dielectric permittivity, and *m* is the electron effective mass [C. Kittel, 1976]. The dispersion of the wave propagating in the plasma whose oscillation frequency is ω, can be described as,

$$\varepsilon(\omega)\omega^2 = \varepsilon(\infty)\left(\omega^2 - \omega_p^2\right) = c^2k^2 \quad (2),$$

where ε is the dielectric permittivity, $\varepsilon(\infty)$ is the dielectric permittivity of positive ion of plasma at the high frequency limit, *c* is the light speed, *k* is the wave vector. On the other hand, the oscillation frequency of light in the bulk with diffractive index *n* is given by:

$$\omega = \frac{c}{n}k \quad (3).$$

The dispersion curve of volume plasmon (of free electron gas) and the light line never cross each other, i.e. there are no common *k* and ω values between volume plasmon and light, indicating that the plasma oscillation, as a compression wave, excited by the polarization cannot interact with propagating

wave directly. The plasmon dispersion is always below the light line, lying in the evanescent region.

Considering more practical models in metals, free electrons are easily polarized. When the free electrons are polarized in the +*z* direction, charges appear on the surface and the force due to the surface charge appears in the -*z* direction, resulting in the collective oscillation of the free electrons. As the practically used plasmon mode in metal is surface plasmon mode, the electromagnetic wave propagates along the interface between two materials with different dielectric constant. A simple model is described as follows, where a flat single interface between dielectric material ($z > 0$) and metal ($z < 0$) is assumed, as depicted in Figure I-1.

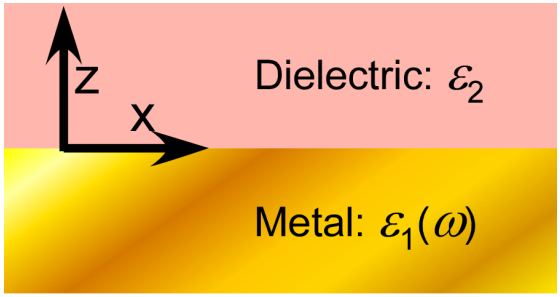

Figure I-1 Metal-dielectric interface.

The dielectric constant values for $z < 0$ and $z > 0$ are $\varepsilon_1(\omega)$ and ε_2, respectively. The real part of the dielectric constant of the metal, Re[ε_1], is negative, while ε_2 of non-absorbing dielectric is a positive real constant. Firstly the introduced TM modes of light are taken into account. Then, the electromagnetic equation set

can be written as,

(i) for $z < 0$,

$$H_y(z) = A_1 e^{i\beta x} e^{k_1 z} \quad \text{(i-1)},$$

$$E_x(z) = -iA_1 \frac{1}{\omega \varepsilon_0 \varepsilon_1} k_1 e^{i\beta x} e^{k_1 z} \quad \text{(i-2)},$$

$$E_z(z) = -A_1 \frac{\beta}{\omega \varepsilon_0 \varepsilon_1} e^{i\beta x} e^{k_1 z}, \quad \text{(i-3)}$$

(ii) for $z > 0$,

$$H_y(z) = A_2 e^{i\beta x} e^{-k_2 z} \quad \text{(ii-1)},$$

$$E_x(z) = iA_2 \frac{1}{\omega \varepsilon_0 \varepsilon_2} k_2 e^{i\beta x} e^{-k_2 z} \quad \text{(ii-2)},$$

$$E_z(z) = -A_2 \frac{\beta}{\omega \varepsilon_0 \varepsilon_2} e^{i\beta x} e^{-k_2 z} \quad \text{(ii-3)},$$

where $\beta = k_x$ is the propagation constant of the waves, $k_i \equiv k_{z,i}\ (i = 1, 2)$ is the wave vector component, perpendicular to the interface. Since the exponential factors are negative, the equations (i-2), (i-3), (ii-2), and (ii-3) imply that the electric field decay in evanescent manner, as the z becomes larger. The condition for the continuity of H_y and $\varepsilon_i E_z$,

$$A_1 = A_2 \quad \text{(4)},$$

and

$$\frac{K_2}{K_1} = -\frac{\varepsilon_2}{\varepsilon_1} \quad \text{(5)},$$

are derived. Note that when ε_2 is positive, Re[ε_1] should be negative. This implies that the modes bound to the surface, i.e., the evanescent field exists only at the interface and exponentially decays into the respective half space.

As the wave equation of TM modes,

$$\frac{\partial^2 H_y}{\partial z^2} + (k_0^2 \varepsilon - \beta^2) H_y = 0 \quad (6),$$

is adopted, k_i are written as,

$$k_1 = \beta^2 - k_0^2 \varepsilon_1 \quad (7),$$

$$k_2 = \beta^2 - k_0^2 \varepsilon_2 \quad (8).$$

From (5), (7) and (8), the propagating wave vector in *x* direction, k_x, is expressed as,

$$\beta = k_0 \sqrt{\frac{\varepsilon_1 \varepsilon_2}{\varepsilon_1 + \varepsilon_2}} = k_x \quad (9).$$

On the other hand, when TE modes are assumed, the electromagnetic equation set can be written as,

(iii) for $z < 0$,

$$E_y(z) = A_1 e^{i\beta x} e^{k_1 z} \quad \text{(iii-1)},$$

$$H_x(z) = i A_1 \frac{1}{\omega \mu_0} k_1 e^{i\beta x} e^{k_1 z} \quad \text{(iii-2)},$$

$$H_z(z) = A_1 \frac{\beta}{\omega \mu_0} e^{i\beta x} e^{k_1 z}, \quad \text{(iii-3)}$$

(iv) for $z > 0$,

$$E_y(z) = A_2 e^{i\beta x} e^{-k_2 z} \quad \text{(iv-1)},$$

$$H_x(z) = -i A_2 \frac{1}{\omega \mu_0} k_2 e^{i\beta x} e^{-k_2 z} \quad \text{(iv-2)},$$

$$H_z(z) = A_2 \frac{\beta}{\omega \mu_0} e^{i\beta x} e^{-k_2 z} \quad \text{(iv-3)}.$$

Due to the requirement of the continuity of E_y and H_z at the interface,

$A_1 = A_2$ (4),

thus

$A_1(k_1+k_2) = 0$ (10).

Here the confinement of Re[k_1] > 0 and Re[k_2] > 0 is satisfied only when A_1 = 0, indicating that

$A_1 = A_2 = 0$ (4')

It is clear that TE modes never exist in surface plasmon polaritons, that is, only TM modes are allowed.

In order to couple the surface plasmon mode and the light, they should have the same k_x and ω, corresponding to the momentum and energy of waves, respectively, otherwise the energy cannot be exchanged. However, the dispersion of surface plasmon mode described in equation (9) still does not cross the light line, as in the case of volume plasmon. One solution can be obtained by assuming evanescent waves. The evanescent wave is generated by introducing the incident light into a substance with large reflactive index under the total reflection condition, or by diffracting the incident light with a metal grating. Otto configuration is well known geometry, in which prism and metal surface are separated by a thin air layer, but close enough for the surface plasmon field and the evanescent TM wave field (from the total reflection at the air/prism interface) to spatially overlap [A. Otto, 1968]. The surface plasmon is excited and resonates with the evanescent wave when

$k_{sp} = \left(\frac{\omega}{c}\right) n_1 sin\theta_0$ (11),

is satisfied, where k_{sp} is the real part of the wave vector of the surface plasmon, n_1 is the refractive index of the prism, and θ_0 is the incident angle at which the light is incident to the prism. As shown in Figure I-2, Kretschmann configuration using a metal film instead of air layer is also famous, which contains two interfaces between dielectric and metal: metal/air and metal/prism surface [E. Kretchmann, 1968].

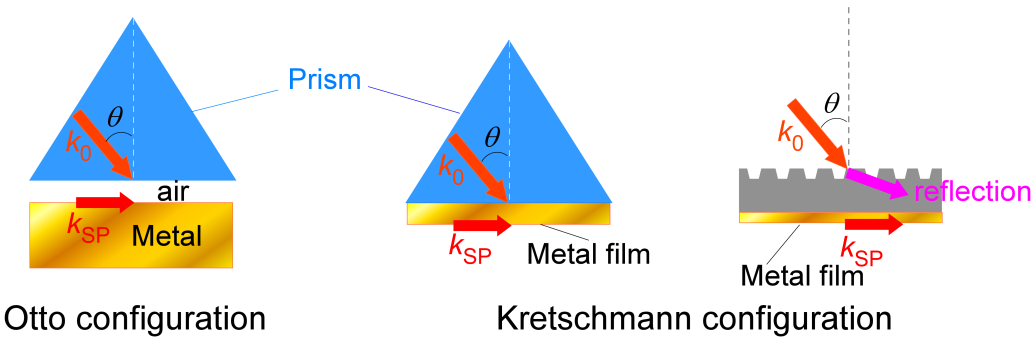

Figure I-2 Otto and Cretschmann configurations.

Since the light line cuts the dispersion relations of the surface plasmon oscillation at the interface of the metal/air, not at the interface of the metal/quartz, the plasmon resonance is excited only at the metal/air interface. In addition to prism coupling, grating coupling is also suitable for exciting coupled surface plasmon resonance. At the surface of dielectric grating, the light is totally reflected and an evanescent wave is generated, when the in-plain wave vector of reflected light, k_x, is larger than that of the incident light k_0;

$$k_x = k_0 sin\theta \pm \nu g \quad (12),$$

where ν is an integer (ν = 1, 2, 3…), g (= $\frac{2\pi}{a}$) is the reciprocal vector of the grating. The situation that can occur in Otto configuration and Kretchmann configuration is called attenuated total reflection (ATR). A clear dip is observed in the reflectivity spectra at the surface plasmon resonance angle, and the shape and the position of the dip are sensitive to the thickness, the material type of metal films. Since the dip of reflectivity spectra is very sensitive to the surrounding dielectric environment, it is often used in surface analysis; the substance absorbed on the waveguide is detected [E. Kretschmann, 1971][S. C. B. Gopinath, 2013].

1-2-3. Localized surface plasmon resonance

In order to induce the coupling between surface plasmon and incident light, metal nanoparticle with sub-wavelength scales are often used. Localized surface plasmon can be intuitively understood, when the metal/dielectric interface described in Section 1-2-2 continuously curves and forms a small nanosphere with a closed surface. Since the ratio of surface against volume is large, the electromagnetic property of the surface would be dominant compared with bulk case. The size of the sub-wavelength metal nanoparticles is of the order of penetration depth, so that the electromagnetic field associated with the incident light penetrates the particle. That is, the phase of the electromagnetic field associated with the incident light is constant in the entire particle, which oscillates with time. Hence a quasi-static model can be applied to the particle much smaller than the wavelength of incident light. Here non-propagating plasmon is excited, which is called localized surface plasmon resonance.

A homogeneous sub-wavelength-size metal sphere with dielectric function of $\varepsilon(\omega)$ and radius *a* is assumed to be placed in the static field of $\mathbf{E}_0$ as illustrated in Figure I-3. The surrounding medium is non-absorbing and isotropic with dielectric function of ε_m. An electrostatic approach to treat this situation is as follows [S. A. Maier, 2007].

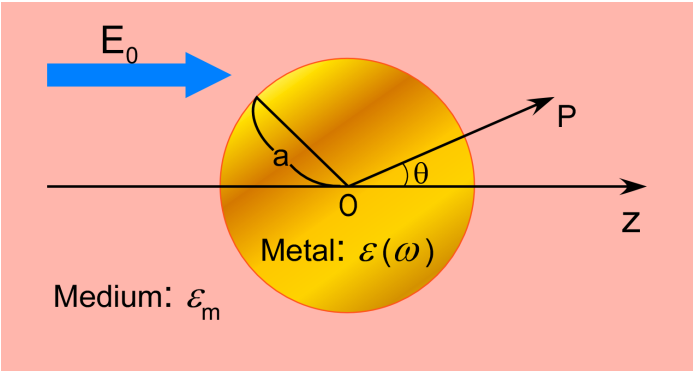

Figure I-3 Geometry of homogeneous metal sphere in an electro static field.

The potential of inside the sphere, Φ_{in} (r, θ), and that of outside the sphere, Φ_{out} (r, θ) can be described as,

$$\Phi_{in}(r,\ \theta)\ = \sum_{l=0}^{\infty} A_l r^l P_l(cos\theta) \qquad (13),$$

$$\Phi_{out}(r,\ \theta)\ = \sum_{l=0}^{\infty} \left[B_l r^l + C_l r^{-(l+1)}\right] P_l(cos\theta) \qquad (14),$$

where λ is the Legendre Polynomials of order, θ is the angle between position vector **r** and *z* axis. The boundary condition requires

$$\Phi_{in}\ (r,\ \theta)\ \rightarrow\ -E_0 r cos\theta\ \ (r \rightarrow \infty) \qquad (15),$$

$$B_1\ =\ -E_0 \qquad (16),$$

and

$$B_l\ =\ 0\ \ (l \neq 0) \qquad (17).$$

The other boundary condition at $r = a$ requires the gradient continuity in Φ with both θ and r ;

$$-\frac{1}{a}\frac{\partial \Phi_{in}}{\partial \theta}\Big|_{r=a} = -\frac{1}{a}\frac{\partial \Phi_{out}}{\partial \theta}\Big|_{r=a} \qquad (18),$$

and

$$-\varepsilon_0 \varepsilon \frac{\partial \Phi_{\text{in}}}{\partial r}|_{r=a} = -\varepsilon_0 \varepsilon_{\boldsymbol{m}} \frac{\partial \Phi_{\text{out}}}{\partial r}|_{r=a} \quad (19).$$

Equations (18) and (19) yield [J. D. Jackson, 1999];

$$\Phi_{\text{in}} = -\frac{3\varepsilon_{\boldsymbol{m}}}{\varepsilon+2\varepsilon_{\boldsymbol{m}}} E_0 r\cos\theta \quad (20),$$

$$\Phi_{\text{out}} = -E_0 r\cos\theta + \frac{\varepsilon-\varepsilon_{\boldsymbol{m}}}{\varepsilon+2\varepsilon_{\boldsymbol{m}}} E_0 a^3 \frac{\cos\theta}{r^2} \quad (21),$$

while $A_l = C_l = 0 \ \ (l \neq 0)$ (22).

Φ_{out} can be redefined as,

$$\Phi_{\text{out}} = -E_0 r\cos\theta + \frac{\mathbf{p}\cdot\boldsymbol{r}}{4\pi\varepsilon_0\varepsilon_{\boldsymbol{m}} r^3} \quad (23),$$

when the dipole moment **p** is introduced since Φ_{out} is the sum of the applied field and the dipole field. This dipole approximation is reasonable because an enough small sphere compared with wavelength is assumed. Comparing the equations of (21) and (23), **p** is written as

$$\mathbf{p} = 4\pi\varepsilon_0\varepsilon_m a^3 \frac{\varepsilon-\varepsilon_m}{\varepsilon+2\varepsilon_m} \boldsymbol{E}_0 \quad (24).$$

When dipole approximation is adapted, **p** is redefined as;

$$\mathbf{p} = \varepsilon_0\varepsilon_m \alpha \boldsymbol{E}_0 \quad (25),$$

since equation (15) indicates that the dipole is induced by $\mathbf{E}_0$. The parameter α is called polarizability. By comparing (24) and (25), α is written as;

$$\alpha = 4\pi a^3 \frac{\varepsilon-\varepsilon_m}{\varepsilon+2\varepsilon_m} \quad (26),$$

which is similar to Clausius-Mossity relation;

$$\alpha = \frac{3\boldsymbol{\varepsilon_0}}{\boldsymbol{N}} \frac{\boldsymbol{\varepsilon-\varepsilon_m}}{\boldsymbol{\varepsilon+2\varepsilon_m}} \quad (27),$$

where *N* is the number density of atoms. As seen from equation (26), a resonant feature appears when,

Re [$\varepsilon(\omega)$] = $-2\varepsilon_m$ (28),

which is called Fröhlich condition, leading to the dipole surface plasmon mode. Since electric field is described as $\boldsymbol{E} = -\nabla\Phi$, and both Φ_{in} and Φ_{out} in equation (20) and (21) contain the term $\varepsilon + 2\varepsilon_{\text{m}}$ in the denominators, similar to α, the dipole and internal field are enhanced at the resonance condition of α. Now the oscillating dipole moment ***p*** is written as;

$$\mathbf{p}(t) = \varepsilon_0\varepsilon_m\alpha\boldsymbol{E}_0\boldsymbol{e}^{-i\omega t} \quad (25').$$

The total electromagnetic field with oscillating dipole is described as;

$$\mathbf{H} = \frac{ck^2}{4\pi}(\mathbf{n}\times\mathbf{p})\frac{e^{ikr}}{r}\left(1-\frac{1}{ikr}\right) \quad (29),$$

$$\mathbf{E} = \frac{1}{4\pi\varepsilon_0\varepsilon_m}\left\{k^2(\mathbf{n}\times\mathbf{p})\times\mathbf{n}\frac{\boldsymbol{e}^{ikr}}{\boldsymbol{r}} + [3\mathbf{n}(\mathbf{n}\cdot\mathbf{p})-\mathbf{p}]\left(\frac{\mathbf{1}}{\boldsymbol{r}^3}-\frac{\boldsymbol{ik}}{\boldsymbol{r}^2}\right)\boldsymbol{e}^{ikr}\right\} \quad (30),$$

where $k = \frac{2\pi}{\lambda}$ and **n** is the unit vector in the direction of $\underset{OP}{\rightarrow}$ in Figure I-3. Supposing ($kr = \frac{2\pi r}{\lambda} \ll 1$), equations of (29) and (30) are approximated as;

$$\mathbf{H} = \frac{i\omega}{4\pi}(\mathbf{n}\times\mathbf{p})\frac{1}{r^2} \quad (31),$$

$$\mathbf{E} = \frac{3\mathbf{n}(\mathbf{n}\cdot\mathbf{p})-\mathbf{p}}{4\pi\varepsilon_0\varepsilon_m\boldsymbol{r}^3} \quad (32),$$

respectively, implying that electric field is predominant over the magnetic field, since the denominators in electric and magnetic field contains r^3 and r^2, respectively, where *r* is a very small value compared with wavelength of light. In addition, it is note worthy that the scattering cross section (C_{sca}) and absorption

cross section (C_{abs}) are enhanced by the polarizability, α. The calculation using Poynting vector based on equations (29) and (30) gives,

$$C_{sca} = \frac{k^4}{6}|\alpha|^2 = \frac{8\pi}{3}k^4a^6|\frac{\varepsilon-\varepsilon_m}{\varepsilon+2\varepsilon_m}|^2 \quad (33),$$

$$C_{abs} = k\mathrm{Im}[\alpha] = 4\pi ka^3\mathrm{Im}[\frac{\varepsilon-\varepsilon_m}{\varepsilon+2\varepsilon_m}] \quad (34).$$

For a sphere with a small radius of a ($a \ll \lambda$), the absorption (with factor of a^3) is dominant over scattering (with factor of a^6). The cross section of extinction, C_{ext}, is the sum of that of absorption and scattering cross sections;

$$C_{ext} = C_{abs} + C_{sca} = 9\frac{\omega}{c}\varepsilon_m^{\frac{3}{2}}V\frac{\varepsilon_2}{[\varepsilon+2\varepsilon_m]^2+\varepsilon_2^2} \quad (35),$$

where the dielectric function is described as $\varepsilon = \varepsilon_1 + i\varepsilon_2$.

The above equation is valid only for perfect spheres. When an ellipsoid particle is assumed, the polarizabilities along the principal axes are written as [C. F. Bohren, 1983],

$$\alpha_i = 4\pi a_1a_2a_3\frac{\varepsilon(\omega)-\varepsilon_m}{3\varepsilon_m+3L_i(\varepsilon(\omega)-\varepsilon_m)} \quad (36),$$

where the ellipsoid satisfies $\frac{x^2}{a_1^2}+\frac{y^2}{a_2^2}+\frac{z^2}{a_3^2}=1$ and $a_1 \le a_2 \le a_3$. L_i is the geometrical factor given by;

$$L_i = \frac{a_1a_2a_3}{2}\int_0^\infty \frac{dq}{(a_i^2+q)f(q)} \quad (37),$$

where

$$f(q) = \sqrt{(q+a_1^2)(q+a_2^2)(q+a_3^2)} \quad (38).$$

Note that the spatial “retardation” should be taken into account when the radius of the metal sphere becomes larger. In such case, the electrons in the

particle at the forward and back surface sides feel electromagnetic field with opposite directions. Thus quasi-static model cannot be used and, instead, Mie theory should be adopted.

1-2-4. Resonant wavelength

The plasmonic metal nanoparticles attract researchers because the electric field is substantially enhanced at various frequencies, depending on the shape and dimension of the nanoparticles, even if the same materials are used. This is in sharp contrast to conventional molecules such as organic complexes which absorb only particular wavelengths of light specific to the molecule. As shown in equations (36) and (37), the polarizability α differentiate by L_i and ε_m, thus the geometry of nanoparticles and the dielectric properties of surrounding substance affect the resonance frequency. Here I present examples of experimentally observed or theoretically calculated resonance peak shift on metal nanoparticles; which can be controlled by the size, shape, surrounding solvent/chemical modification, carrier density, near field coupling of plasmon resonance, and the constituent materials. Au nanorods exhibit plasmon resonance in the visible region, in which the plasmon resonance peak was gradually enhanced and red-shifted from 600 to 800 nm in wavelength in longitudinal mode, as the aspect ratio (length/diameter) of the Au nanorods became larger [F. Kim, 2002]. The aspect ratio (2.8 - 4.8) was controlled by the amount of Ag nitride solution added to the hydrogen tetracholoaurate solution, during the UV-reduction process of $AuCl_4^-$ ion to Au. The calculated extinction spectra of Ag nanocubes [F. Zhou, 2008] also showed that the peak position of the resonance peak in dipole (15 to 90 nm in the edge length) mode and quadrupole mode (100-200 nm in the edge length) was red-shifted with

increasing edge length. The systematic resonance frequency shifts for Au nanorods and nanospheres were reported by Ueno *et al* and Sönnichsen *et al* [K. Ueno, 2005] [C. Sönnichsen, 2002]. Ueno *et al* observed the local surface plasmon modes of rectangular, parallel piped Au nanoblocks (with aspect ratios of 1, 3, 5, 7, 9:1) made by electron-beam lithography and sputtering methods, where the size and the aspect ratio of the nanostructure were precisely controlled in a nanometer scale. A single plasmon resonance peak was observed at 700 nm for the nanostructures with an aspect ratio of 1:1, which split into two separated peaks of longitudinal and transverse modes with increasing aspect ratio. When the polarization of incident light was set to be either parallel or perpendicular to the rod, only longitudinal or transverse mode was excited, respectively. The longitudinal surface plasmon peak was linearly red-shifted from 930 to 1500 nm in wavelength as the aspect ratio became larger from 1:1 to 9:1, being consistent with the calculation based on the dipole approximation, while that of transverse mode was blue-shifted from 620 nm to 550 nm. Selective excitation of plasmon band was achieved from visible to near-infrared region by precisely controlling the three-dimensional structures and alignments. In the experiments of Sönnichsen, the resonance frequency in the scattering spectra was also shifted toward longer wavelength as the aspect ratio (1, 2, 3, 4:1) and the size (size: 20, 40, 60, 80, 100, 150 nm) became larger. They also evaluated the dephasing time scale from the line width of the light scattering spectra (scattering intensity versus light energy). The lifetime of the resonance

was in 6 to 18 fs in Au nanorods and 1.4 to 5 fs in Au spheres. Each value agreed well with the theoretical ones and the lifetime became longer at larger aspect ratio of the rods and smaller size in spheres.

In nanostructures with more complicated shapes, such as gold nanostars [F. Hao, 2007], the spectra should be treated with hybridized model. Observed scattering spectra changed depending on the polarization of the incident light and the each spectrum showed distinct peaks, due to the bonding and anti-bonding combination of core and tips (Figure I-4). Interestingly, there were several peaks, not two (from the core/tip), in the spectrum. This can be rationalized by assuming that some of five tips were coupled together to enhanced scattering, depending on the direction of the incident light polarization. The hybridized model is often used to treat nanovoid structures, in which the sphere and cavity are coupled in a bonding and anti-bonding manner. The validity of the hybridization model was confirmed by quantum mechanical and FDTD calculations [E. Prodan, 2003][C. Oubre, 2004]. It was reported that the shape and size of the metal nanoparticles strongly affect the optical properties.

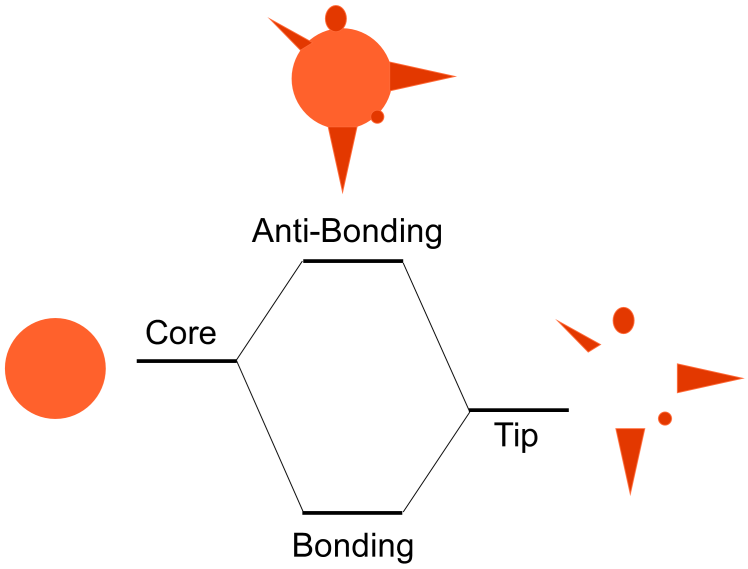

Figure I-4 Bonding and anti-bonding combination.

Now the effect of surrounding matrix is discussed. The absorption wavelength of surface plasmon resonance, can be written as [M. Kanehara, 2009],

$$\lambda^2 = \lambda_p^2(\varepsilon^\infty + 2\varepsilon_m) \quad (39),$$

where λ_p is the bulk plasma wavelength of the constituent material, ε^∞ is the dielectric constant at high-frequency region, and ε_m is the dielectric constant of the surrounding medium. As expected from equation (39), the resonance wavelength is red-shifted when surrounded by a medium with larger dielectric constant (or refractive index n, $= \sqrt{\varepsilon\mu}$). An example of this effect is seen in nanoparticles with core-shell structure [W. Shi, 2006]. Namely, Au nanoparticles with a diameter of 10 nm show a resonance peak at 560 nm in the extinction spectrum, whereas the resonant peak is red-shifted in Au-Fe_3O_4 core-shell particles, where the refractive index of Fe_3O_4 was ~2.4. It was also found that the

red-shifted becomes much more significant with increasing the thickness of Fe_3O_4 shell *t* (λ = 560 nm, 585, 600 nm for *t* = 1, 2, 3 nm, respectively). The red-shift and enhancement of peak intensity were also observed when the shell material was changed from Fe_3O_4 to PbS, the latter of which has a refractive index (real part) of ~4.3. As another example, the longitudinal and transverse plasmon resonance peaks in extinction spectrum of the Au-Ag nanorods, were shifted by 10 nm and 1 nm respectively, as the surrounding solution was changed from aqueous solution to glycerol (refractive index = 1.358), which was qualitatively confirmed by theoretical calculation [A. V. Alekseeva, 2006]. It was also revealed that the sensitivity of the plasmon resonance to the refractive index of surrounding solution was influenced by the axial ratio of nanorods.

Plasmon resonance is not limited to metal particles; Kanehara *et al.* [M. Kanehara 2009] reported that the near-IR absorbance spectra of Sn-doped indium tin oxide (ITO) nanoparticles clearly showed red-shift as the refractive index of the surrounding solvents increased from 1.37 (hexane) - 1.55 (nitrobenzene). They also examined the plasmon resonance properties as a function of carrier density, which was controlled by the amount of doping Sn, and found that the carrier density is another critical factor determining the resonance peak position. They concluded that ITO nanoparticle is a “well-defined SPR (surface plasmon resonance) -tunable conductive metal oxide system in the near infrared (NIR) region”. The resonance peak position was blue-shifted almost linearly (from 1940 nm to 1618 nm in wavelength) as the doping

concentration increased from 3% to 10%, where the percentage of Sn was defined as; $\%\mathrm{Sn} = 100\% \times \frac{[\mathrm{Sn}]}{[\mathrm{Sn}]+[\mathrm{In}]}$. However, further Sn doping (from 15% to 30%) induced the gradual red-shift (from 1626 nm to 1836 nm in wavelength) of the plasmon resonance peak as a consequence of the decrease in electron density due to the trapping of conduction electrons around Sn ions. Similar phenomena were seen in the vacancy doped semiconductor quantum dots of cupper sulfide [J. M. Luther, 2011]. Though stoichiometric Cu_2S nanorods showed no LSPR peak at NIR region, the LSPR peaks appeared and were blue-shifted (from ~1.5 to ~1.7 eV) as the Cu vacancies were introduced by exposing the nanorods to ambient air.

Besides, the dielectric constants of metal nanostructure materials, also affect the LSPR peak. Indeed, the LSPR peak position of Au nanoparticles was longer than that of Ag nanoparticles in absorbance spectra [S. Link, 1999]. Link *et al*. also investigated the LSPR peak position in Au-Ag alloys and found that the peak was red-shifted linearly with respect to the Au molar fraction. Mixtures of Au and Ag formed homogenous alloys and the calculation absorption spectrum agreed well with the experimental one only when the dielectric constant of Au-Ag alloy was taken into consideration. Meanwhile, the experimental spectrum could not be reproduced when dielectric constant was assumed to be $\varepsilon(\alpha) = (1-\alpha)\varepsilon_{Au} + \alpha\varepsilon_{Ag}$. Though Au and Ag have almost equivalent dielectric constant values, the dielectric constant of the Au-Ag alloy was very different from those of

Au or Ag because the band structure was significantly modified by the alloying. How important the selection of conducting material will be discussed in Section 1-4.

Finally I explain about the coupling between different plasmon resonance modes. Since the plasmon resonance is a near-field phenomenon, different plasmon modes couple with each other when they are close enough (approximately the size of the nanoparticles) for their spatial distribution to be overlapped. Theoretically, two individual plasmon resonances in metal nanoparticles hybridize into bonding and antibonding dimer plasmon [P. Nordlander, 2004]. The separation of these energy levels became larger as the two metal particles come closer in hybridization model, and this behavior was also confirmed by FDTD calculation. It was experimentally reported that the plasmonic peak of silver dimer, in which Ag nanoparticles were connected by oligonucleotide with fluorophores, was red-shifted relative to that of the monomer [J. Zhang, 2007]. The fluorescent intensity was also enhanced by a factor of more than 10 when the fluorophores were located at the center of the silver dimer compared with the case that the fluorophores were connected to the silver monomer, indicating that the near field coupling of the plasmon resonance enhanced the electric field. It is noteworthy that the plasmon coupling does not always shifts the LSPR toward longer wavelength [S. C. Yang, 2010]. In the scattering images two Au octahedrals, side length of 150 nm, the coupled plasmon resonance was strongly enhanced at the interval of 65 nm; the interval

of the two octahedrals was precisely controlled from 25 nm to 125 nm. Although the LSPR peak of the Au octahedral dimer is red-shifted when the incident light wave vector was parallel to the dimer axis, it was blue-shifted when the incident light wave vector was perpendicular to the dimer axis. The former was related to the bonding mode and the latter one was to the untibonding mode. Thus, the plasmon mode could be regulated by the incident light orientation.

1-3. The applications of plasmonic materials

In this section, I briefly introduce the applications of plasmonics, including photoelectric conversion which is the main topic of this thesis.

The market of the solar cells mainly relies on the expensive silicon crystals, thus semiconductor thin films, not limited to silicon, have been energetically studied in these days. However, a problem to be solved in these films is low absorption near the bandgap. Tremendous efforts have been made to increase the absorption efficiency in thin film based photovoltaic cells, and promising solution for this is utilizing plamonic nanostrctures, which can collect more photons by enhancing surrounding field (absorption) and folding the light in the films using scattering effect [H. A. Atwater, 2010]. Moreover the plasmonic systems can tune the resonant wavelength by size/shape of the nanostructures, which is especially useful to silicon-based cells because silicon cannot efficiently absorb the light from visible (longer than 600 nm in wavelength) to infrared region of the solar spectrum; the plasmonic particles for absorbing the corresponding wavelength regions were also investigated for the application of cells [J. R. Cole, 2006]. When 50% of the silicon surface was covered with the mixture of size-selected Au nanospheres (UV-vis) and Si-Au core-shell structures (vis-IR) with optimal ratios, the calculated absorption spectrum almost reproduced the solar irradiance spectrum. The improvement of the efficiency of silicon-based cells with plasmonic metal nanostructures been investigated both numerically and experimentally, where the scattering effect [F. J. Tsai, 2010][P.

Matheu, 2008], enhanced absorption [D. M. Schaadt, 2005] [C. Rockstuhl, 2008], and coupling with propagating plasmon polaritons [V. E. Ferry, 2008] were taken into account. The propagating mode of plasmon adjacent to the active layer elongates the optical path of the absorbing layer. Instead of the expensive silicon, organic cells with reasonable prices have been explored. In organic cells, the plasmonic structures were utilized in order to raise the relatively low conversion efficiency. In these studies, plasmonic structures were used in various ways: introduced into the scattering layer [M. A. Green, 2010], embedding in the active layer [C. H. Kim, 2011], sandwiched by the active layer and electrode [M. Westphalen, 2000][B. P. Rand, 2004] and so on, and, as a result, the cell properties/absorption were successfully improved by the plasmonic structures.

There is a different type of organic cells called dye synthesized solar cells (DSSC), which takes advantage of photocatalyst electrodes. Photocatalysts, first discovered in TiO_2 system by Honda and Fujishima [A. Fujishima, 1972], can be used in photovoltaic cells to separate UV-induced charges, as follows. In water splitting, semiconductors absorb photons, and then the careers (electron-hole pairs) diffuse separately to generate hydrogen and oxygen from electrons and holes, respectively. That is, the solar energy absorbed by the semiconductor is used for chemical reactions. The photoelectric conversion with photocatalysis seems clean and ideal, however there is a serious problem that most of the semiconductors with high photocatalytic activity like TiO_2 have wide bandgaps

and respond to only UV light, while the semiconductors with smaller bandgaps, such as hematite, have very low mobility of carriers. As reported by Tatsuma *et al*, in contrast, stable photoelectric conversion of visible light was achieve in composite TiO_2 films loaded with plasmonic Au nanoparticles, where the plasmon resonant peak was set at the visible region [Y. Tian, 2005]. The photoexcited electrons of Au were transferred to the conduction band of TiO_2, generating the photocurrent. It is also reported that composites of plasmonic metals and semiconductors showed better photocatalytic properties than the corresponding pure semiconductors at a selected wavelength range [K. Awazu, 2008][S. Link, 2011][T. Takahashi, 2013]. Nishijima *et al*. used Au nanorods loaded on TiO_2 photoelectrode to generate oxygen from water with near infrared light [Y. Nishijima, 2012]. Thus, the plasmon enhanced photoelectric conversion and photocatalytic phenomena enabled us to use full range of solar spectrum. On the contrary, the widening of light absorbing region can also be realized by dyes (dye-sensitized solar cell), where TiO_2 is used as electrodes in DSSCs [M. Gratzel, 2005]. Even in such a case, plasmonic structures can be introduced to to further enhance the efficiency [S. D. Standridge, 2009][M. Ihara, 2010].

Plasmon resonance can be utilized in sensing, as well. The first practical application of surface plasmon resonance was as a gas sensor in 1982, which could detect gases in the ppm range [C. Nylander, 1983]. Another successful example as an application of surface plasmon resonance is the surface-enhanced Raman scattering (SERS), being one of the most sensitive

detection methods, where the Raman signal is enhanced on the order of 10^{14}-10^{15} by localized electromagnetic field of metal nanostructures. Indeed, SERS has sensitivity of single molecular level [J. T. Krug, 1999] and is expected to be used in medical diagnoses [R. A. Alvarez-Puebla, 2012]. In addition, fabrication processes of plasmonic materials for SERS enhancement has been extensively studied; for instance, Fujimaki *et al* developed a easy and reliable fabrication process of Ag nanoparticles from AgO films by laser irradiation [M. Fujimaki, 2007][G. Sauer, 2005][L. Lu, 2006]. Metal nanoparticles enhance not only Raman scattering but also fluorescence, the latter of which can be used as a tool to investigate plasmon-mediated phenomena [S. Kühn, 2006][H. Lin, 2012].

Furthermore, plasmon resonance is useful for studying photochemical reactions [K. Ueno, 2008][S. Haruta, 2011], high-harmonic generation [S. Kim, 2008], dye laser oscillation with plasmon bandgap [T. Okamoto, 2004], optical trapping [H. Nabika, 2010], plasmon controlled electron beam lithography [D. Fromm, 2004][K. Ueno, 2006], sub-wavelength waveguide [S. I. Bozhevonyi, 2006], coloring nanoparticles [K. Okamoto, 2013], spectral thermometry [K. Setoura, 2012], and plasmon rulers [N. Liu, 2011]. The applications of plasmonics, will spread over various areas in the next decades. Especially, from the view point of effective use of solar energy source, enclosing light energy into small spaces with plasmonic antennas would become inevitable. Further investigations from both physical and chemical aspects are needed.

1-4. Ag nanoparticles

Nanoparticles of noble metals, especially Au, Ag, Cu and Al, are known to show plasmon resonance. Among them, Ag metal nanoparticles have been intensively studied because they efficiently enhance the surrounding electromagnetic field, compared with other materials [R. P. Van Duyne, 1993][S. Nie, 1997][K. Kneipp, 1997][N. G. Greeneltch, 2012]. Considering the Mie theory, the extinction coefficients of single metal nanoparticle of 60 nm sphere were calculated in a text book [D. Sarid, 2010]. The extinction corresponds to the sum of absorption and scattering, but the contribution of absorption is much larger than that of scattering as mentioned in the former Section 1-2-3; larger extinction coefficient implies that electric field is more enhanced due to plasmon resonance. The extinction coefficient of Ag was the largest among aforementioned metals, by several times in visible region. This is because the imaginary part of the dielectric constant, corresponding to the dissipation, of Ag is small. According to the DDA calculations for the extinction efficiency of Cu, Au and Ag nanoparticle arrays on glass substrates, the peak-top intensity was largest and the peak position was shortest (in wavelength) in Ag, where the diameter and height of each nanosphere were set to 390 nm and 50 nm, respectively [G. H. Chan, 2007]. This is why Ag is often used in applications utilizing plasmonic field enhancement, such as photovoltaic cells, sensors and so on, as cited in previous Section 1-3. In case of the near field optical sensors or biosensors, the original signals are small especially in Raman scattering, thus how much the

original signals are enhanced is critical. Ag nanoparticles are preferably chosen in sensing devices. There is a report comparing the sensitivity between Ag, Ag-Au alloy and Au based on DDA calculations. In the report, the extinction efficiency, response of plasmon resonance wavelength to the external dielectric constant variation, scattering quantum yield, and the full width half-maximum (FWHM) of the plasmon resonance peak were described [K. S. Lee, 2006]. It was revealed that the sensitivity of plasmon resonance peak position to the surrounding medium was similar in all the compositions examined but the absolute peak intensity became higher and the bandwidth became narrower as the Ag composition increased: pure Ag showed the largest intensity and narrowest plasmon peak in the scattering spectrum. Although the sensitivity in wavelength shift depended on the real part of the dielectric function of the metal nanorod, the intensity and sharpness of the signal were strongly affected by the imaginary part of the dielectric function. Lee *et al.* suggested that Ag is more advantageous than Au or the alloys as a nanoparticle material used in practical sensors because the actual sensitivity of the sensors depends on the absolute intensity and the bandwidth of plasmon resonance peaks. The sensitivity (of the plasmon resonance wavelength shift to the surrounding refractive index) of Au, Ag, and Cu nanoparticles in various structures were also evaluated from the figure of merit (FOM) values, where the figure of merit can be defined as the LSPR wavelength shift divided by FWHM [J. S. Sekhon, 2011]. As a consequence, it was found that Ag nano particles in prolate shapes showed the

best FOM in the visible to infrared region, as long as Ag was protected from oxidation. Better sensitivity of Ag than Au was reported by many researchers [A. J. Haes, 2004][I. Tanahashi, 2007]. However Ag has a problem in practical uses that it is chemically unstable, as well as Cu. In the Cu nanoparticle case, the plasmon resonance peak in the extinction spectra becomes broad and small even just after the fabrication of Cu nanoparticles because it is soon covered with oxide shell, [G. H. Chan, 2007]. The surface oxide layers can be removed by glacial acetic acid without harming the inner Cu metal parts [K. L. Chavez, 2001], and after the treatment the plasmon peak recovers its intensity and sharpness.

Though the applications of Ag nanoparticles are expected in various fields, the chemical instability in ambient atmosphere prevents their applications. It was reported that the nanometer-sized Ag nanoparticles in SiO_2 were deteriorated in several days or a week at ambient condition [M. Hillenkamp, 2007]. That is, as time went, the peak intensity decreased and the peak width was broadened due to the oxidation of Ag nanoparticles. Indeed, the intensity of plasmon resonance peak of the Ag particles became less than half after a day, compared with that one hour after the fabrication. Y. Han quantitatively discussed the correlation between Ag oxidation and surface-enhanced Raman scattering (SERS) activity, by intentionally oxidizing of the surface of Ag nanoparticles with ozone [Y. Han, 2011]. The SERS enhancement factor sharply dropped as the thickness of Ag_2O shell increased, where the thickness of Ag_2O layer was estimated from the

chemical composition determined by XPS. The SERS enhancement factor was suppressed by 3 orders of magnitude when the Ag_2O shell thickness was 0.4 nm, compared with that of non oxidized Ag nanoparticles. There are other reports on the Ag nanostructure variation by the deterioration; the plasmon resonance peak was blue-shifted accompanied with the deterioration [R. J. Peráez, 2013][T. W. H. Oates, 2013].

For the deterioration of Ag, not only oxidation but also sulfurization should be concerned, as the major causes of rapid rotting of Ag nanoparticles [L. Wang, 2011]. The surface of Ag absorbs water from humidity, acting as solution field to chemical reaction [T. E. Graedel, 1985][T. E. Graedel, 1992]. When carbonyl sulfide (COS) or hydrogen sulfide (H_2S) gas, was absorbed in the solution, HS^- ion are generated which react with the Ag metal surface or Ag^+ in the solution; low solubility Ag_2S segregates on the surfaces of Ag nanoparticles. Ag reacts with even ambient levels of COS and H_2S gas. Mcmahon reported the detail on the plasmonic resonance of Ag nanoparticles sulfidized by OCS in ambient laboratory air [M. D. Macmahon, 2005]. The surface plamsmon resonance peak of annealed 2D Ag nanodisk array was continuously red-shifted, broadened, and weakened until 36 hours after the fabrication. Scanning Auger spectroscopy clearly showed the contamination of sulfur, which was likely to be absorbed to the Ag surfaces. Spectra of Ag spheres with Ag_2S shells were calculated based on Mie theory, indicating the damping and red-shift of plasmon resonance peak with the thickness of Ag_2S shell, similar to the experimental results. The growth

rate of the Ag_2S shell, estimated from the shift of plasmon resonance peak position compared with calculated ones, was 3 nm in thickness per day, which is 7.5 times larger than that reported in Ag films [D. K. Burge, 1969]. These indicate that Ag with higher surface to volume ratio, such as nanoparticles, would be deteriorated faster.

The stability of Ag nanoparticles has been the subject of intensive studies for decades, and the coating of the Ag particles with various materials is now widely used to protect Ag [N. Hagura, 2010][M. M. Oliveira, 2005][V. G. Kravets, 2014].

1-5. Nanocomposite materials

Composite materials now belong to hot research topics from both fundamental and industrial interests. Pure materials no longer satisfy recent wide and complicated demands, so that creating totally new materials by combining different ones should be needed. The first semiconductor composite, in which single crystalline CdS particles were dispersed in a polyurethane film, was developed as a catalysis generating H_2 by direct dissociation of water in 1980's [D. Meissner, 1983]. Following the rapid growth of the science and technology of composite materials, great numbers of new materials were created, particularly, through splaying metal salt in plasma [M. Kagawa, 1984], sputtering [L. Maya, 1996], intercalation [P. B. Malla, 1991], sol gel method [M. L. Balmer, 1995], ballmilling [M. P. Horvath], etc.

Recently composites containing metal particles dispersed in a insulator matrix called cermets are well studied, which work as multifunctional devices indicating mechanical, magnetic, electric, or optical responses at the same time [J. S. Moya, 2007]. The mechanical strength of the brittle ceramics can be improved by adding metal, as seen in alumina/Ni composite, where the combination of metal and ceramic should be chosen so as to obtain firmly bonded ceramic/metal interface [W. G. Fahrenholtz, 2000][W. H. Tuan, 1995], otherwise cracks would propagate between metal and ceramic. In contrast, the strength of ZrO_2 was not increased by adding Ni [A. Morales-Rodriguez, 2003]. This is possible because oxygen vacancies changes the bonding character and the

atomic coordination, as revealed by Ab initio DFT calculation [J. I. Beltran, 2003] [J. I. Beltran, 2004].

Magnetic metal particles were also added to oxides to modify their magnetic properties. An example is a PLD-deposited yttria stabilized zirconia (YSZ) polycrystalline film added with Ni particles; the film was deposited on Si substrate by using multi target carousel system equipped with Ni and YSZ targets [J. T. Abiade, 2008]. The size of Ni nanoparticles in multiple layers of YSZ increased with deposition time of Ni. The magnetic properties showed clear dependence on the nanoparticle size: the coercivity at room temperature increased as the nanoparticle size became larger and, moreover, the composite underwent a superparamagnetic to ferromagnetic transition with increasing the particle size.

Recently, the number of theoretical calculations on the composite materials is increasing, helping us understand the physical properties of composites. A theoretical study on nanocomposite films of Mn-doped ZnO ($Zn_{30}Mn_2O_{32}$) also discussed about the magnetism as a function of Mn configuration (doped site) [Q. Wang, 2004]. The result of the first principal calculation explained that Mn configuration occupying nearest Zn sites was most stable and thus heavily doped Mn tended to form clusters, being consistent with the experimental result [Z. Jin, 2003]. Calculations on the magnetic moment of each possible configuration predicted that the ground state was antiferromagnetic, which is also consistent with experimental results [K. Ueda, 2001][T. Fukumura, 2001].

Optical properties are paid more attention because of their wide applicability including optical sensors, computers, filters, polarizers, cells and so on. For instance, the nanocomposite films containing CdS showed larger third order nonlinear susceptibility than bulk CdS [E. F. Hillinski, 1988][Y. Wang, 1990]; the small particles inside the matrix contributed to the optical properties and the surrounding matrix stabilized the particles growth. In semiconductor composites, nonlinear switching [A. S. B. Sombra, 1992], laser amplifying [L. L. Beecroft, 1997a], high refractive index materials (antireflection coating for solar cells)[L. L. Beecroft, 1997b] were also reported. When metal nanoparticles are embedded in the matrix, such as cermets, plasmonic properties are expected [T. Ung, 2001][B. Palpant, 1998][G. Carotenuto, 2000][H. Takele, 2006][D. Manikandan, 2003][N. Bahlawane, 2011]. As shown in the former Sections 1-2-3, 1-2-4, and 1-3, the matrix not merely stabilizes the unstable nanoparticles but also contributes to the enhancement of the plasmonic electromagnetic field and the tuning of the resonant wavelength. Thus controlling the shape/size of the metal nanostructures and choosing a suitable matrix material are important for the regulation of the optical properties. Thus, how to fabricate such composite materials is one of the urgent research topics. The aim of this thesis is to contribute to these researches through developing processes to fabricate Ag nanostructure in a TiO_2 medium, in a reproducible manner, and investigating their optical properties, pursuing their applications to photovoltaic cells and optical biosensors.

Here I have to mention about the density of the embedded metal nanoparticles. There is a limit to the amount of nanoparticles to be inserted in a matrix, which is called “percolation limit”. When the density of embedded metal spices is low, both the structural and physical properties continuously changes with metal concentration. At higher metal concentration, meanwhile, the nanoparticles combine with each other to form aggregates called “coalescent”. The limiting metal concentration is called percolation limit, above which the metal nanoparticles are combined with each other to become a unified metal film [M. Garcia del Muro, 2008] [E. Céspedes, 2010]. Interestingly, the composites near or above the percolation limit exhibit anomalous physical properties [J. S. Moya, 2007]: anomalous absorption [F. Brouers, 1993], giant Hall effects [A. B. Pakhomov, 1995], third order non-linearlity [Y. Hamanaka, 2004], etc.

Chapter 2: Experimental methods

2-1. Pulsed Laser Deposition [D. H. Lowndes, 2006]

Pulsed laser deposition (PLD) is a well-known thin film fabrication technique, where a focused laser pulse ablates a material called target. When the target was ablated, the energetic plasma beam called plume is generated; the initial velocity of atoms and ions in a plume is larger than 10^6 cm/s (i.e. 52 eV in kinetic energy), and the kinetic and internal excitation energy is used to the film formation and chemical reactions. The atoms/ions propagates in decelerating manner to the facing substrate, 5-10 cm apart from target, and they are deposited onto the surface of the substrate. The deposition rate would differ depending on how far from the plume; i.e. the deposition rate at the place directly opposite from the plume is larger than that at the rest places, thus it is not suitable for mass production with large area, however, PLD can make high quality films with artificial/complex structure.

Since neither electron beams nor hot filaments are needed, the film fabrication can be conducted under the ambient gas condition, which enables us to make oxide ceramic materials by reactive deposition. Hence the atmosphere and the gas pressure of PLD chamber can be regulated to control the amount of the oxygen vacancy in a film. Moreover, since the substrate can be heated by lamp/laser, the temperature of the substrate and the crystal structure of substrate determine the crystallinity of the fabricated film: amorphous, epitaxial single crystal etc. PLD is widely used in fabricating superconductor and doped

semiconductor materials due to several reasons, as follows. Firstly, the film composition can be transferred from the original target when particular energy of focused laser is chosen. Secondly, multi-layered films, in which layers with different composition share the same/continuous stoichiometry, and films with particles or uniform thickness can be obtained where the thickness of the film is easily controllable in atomic layer level by the deposition rate or the number of laser pulses (corresponding to the deposition time). Thirdly, physical properties of the PLD made film is generally changed by various parameters, such as, the atmosphere of the chamber (including gas pressure), laser power, laser frequency, the composition of targets, the order of the depositing (in multi layered film), deposition rate/the number of laser pulses, the substrates, substrate temperature, and the distance of target and substrate.

2-2. X-Ray Diffraction [C. Kittel, 1976]

X-ray diffraction (XRD) is the common technique to determine the crystal structure, based on the Bragg law. When the electron beam is introduced to a certain lattice plane of a crystal, the electrons are bounced back by each atom composing the lattice plane. Since electrons have the characteristic of wave, only when electrons reflected in a certain direction (angle) are in the same phase, the electrons waves strengthen each other, thus diffraction peak can be observed. Supposing the lattice planes with spacing d, and the incident X-ray hit the plane in an angle θ, the constructive interference can be occurred when;

$n\lambda = 2d\sin\theta$,

which is called Bragg condition, where n is an integer and $\lambda \leq 2d$. The constructive interference pattern as a function of θ becomes a finger print of the sample, from which the crystal structure is identified.

Recently two dimensional XRD is utilized in the detection of crystal structures of epitaxial films or organic single crystals; it provide us the diffraction information along two different axis perpendicular to each other, such as the quality of the crystal, the in-plane and out-plane crystal structures. When the sample is a single crystal, the XRD peak appears as a spot; while the peak becomes arc-like when the orientation of the crystal is not uniform.

2-3. Atomic Force Microscope [G. M. McClelland, 1987]

Atomic force microscope (AFM) is one of the scanning probe microscopy (SPM), which analyzes the morphology and the physical properties of the sample surface by detecting the physical quantity induced between the surface and the probe. Several physical interactions (interfacial forces) exist between the probe and the surface, such as tunneling effect, adsorption force, friction force, interatomic force (nN order), electromagnetic power, etc. AFM senses the atomic force, where optical interference is utilized to detect the motion of probe tip. A laser beam is focused on the cantilever supporting the tip and movement of cantilever in the direction perpendicular (z axis) to the surface is detected by the photodiode; the movement of tip in nm scale is converted to the movement of the laser beam in μm scale. The photodiode signal is converted to the voltage, and this voltage change corresponds to the surface corrugation, where the force between tip and surface is kept constant by a feedback loop. The map of surface morphology can be obtained by precisely moving the sample stage in the direction parallel (x, y plane) to the surface.

Not only surface morphology but also physical property can be imaged simultaneously by the same AFM setup, such as friction force, magnetic force and conductivity. In the conductive AFM measurement, bias voltage is applied to the sample from the sample stage, and current is measured by the probe which is connected to the current/voltage amplifier.

2-4. Electron Microscope [operation manual of JEM-2100F and HP of JEOL]

Scanning electron microscope (SEM) is the microscope using the electron beam with wavelength shorter than that of light, thus showing better resolution (nm scale) than optical microscopes. The electron beam generated by a hot tungsten filament is focused by magnetic lenses, called condenser lens (making the electron beam narrower) and objective lens (adjusting the focus). The lenses are made of coils covered by iron frame called yoke, where the strong magnetic force leaks from the small gap on the frame called pole piece and the focal distance of the lens is variable by the current applied to the coils. Once the focused electron beam hit the surface of a sample set in the vacuum chamber, secondary/Auger/back-scattered electrons, continuous/fluorescent/characteristic X-rays are emitted. Among them, the amount of secondary electrons, originating from valence electrons, are very sensitive to the surface morphology, since only the energy of secondary electrons is enough small to be emitted at the surface and absorbed in the inner part; the larger amount of secondary electrons are emitted with larger tilt angles. The secondary electrons are detected by the detector and converted to the electric signal; the electron beam is scanned along each pixel. In order to know the component of the sample, energy dispersive X-ray spectrometer (EDX) is utilized; the characteristic electrons are also emitted simultaneously during the SEM measurement. In the semiconductor detector, the electron-hole pairs whose number depends on the value of the X-ray energy are generated.

On the contrary, narrower images can be obtained in the transmission electron microscope (TEM); the literal resolution values of TEM and SEM are 0.1-0.3 nm and 0.5-4 nm, respectively. However, the practical resolution in this study was a little worse; less than 10 nm in SEM images and several nm in STEM-EDX mapping images because the sample edge was not so sharp in SEM observation and the resolution of TEM depends on sample thickness and the uniformity of sample structures. Besides, the EDX probe size and the density of each element correspond to the count number of the EDX signal affect the resolution of STEM-EDX mapping measurements. Although the configuration of the magnetic lens in TEM is similar but more complex compared to SEM (Figure 2-4), and the acceleration voltage of the electron beam is larger in TEM (hundreds of kV) than in SEM (several to tens of kV): in this study 15kV in SEM and 200kV in TEM. The electron beam hits the thin sample (less than 100nm in thickness), then the signals, such as secondary/Auger/back-scattered electrons, characteristic X-rays, and transmittance/diffracted electrons, are generated. The bright field TEM images, onto the fluorescent screen, are formed by transmitted electrons and electrons diffracted in low angle, while those of dark field are formed by only scattered and diffracted electrons. Although TEM is useful for the morphological observation, scanning transmission electron microscope (STEM) is powerful tool for the elementary analysis since the whole image of STEM is composed of small pixels each of which can be compared directly with element mapping images. The electron paths of TEM and STEM are reciprocal; the

relation between the electron irradiation system and the imaging system in TEM is same as that between detecting system and irradiation system of STEM. The objective lens position is before and after the sample in STEM and TEM, respectively. In order to analyze the components of samples, not only EDX but also electron energy-loss spectroscopy (EELS) is often used. Incident electrons interact with inner-shell or the outer shell to become inelastically scattered electrons of core-loss or plasmon-loss. The energy loss of the electrons is detected by the electron spectrometer; the position of the detector is determined by energy loss of the electron which is energetically dispersed by magnetic field. The energy filtered image of the core-loss peak corresponding to the specific binding energy gives the elemental mapping, while that of plasmon-loss peak corresponding to plasmon resonance peak becomes the mapping of electronic field enhancement.

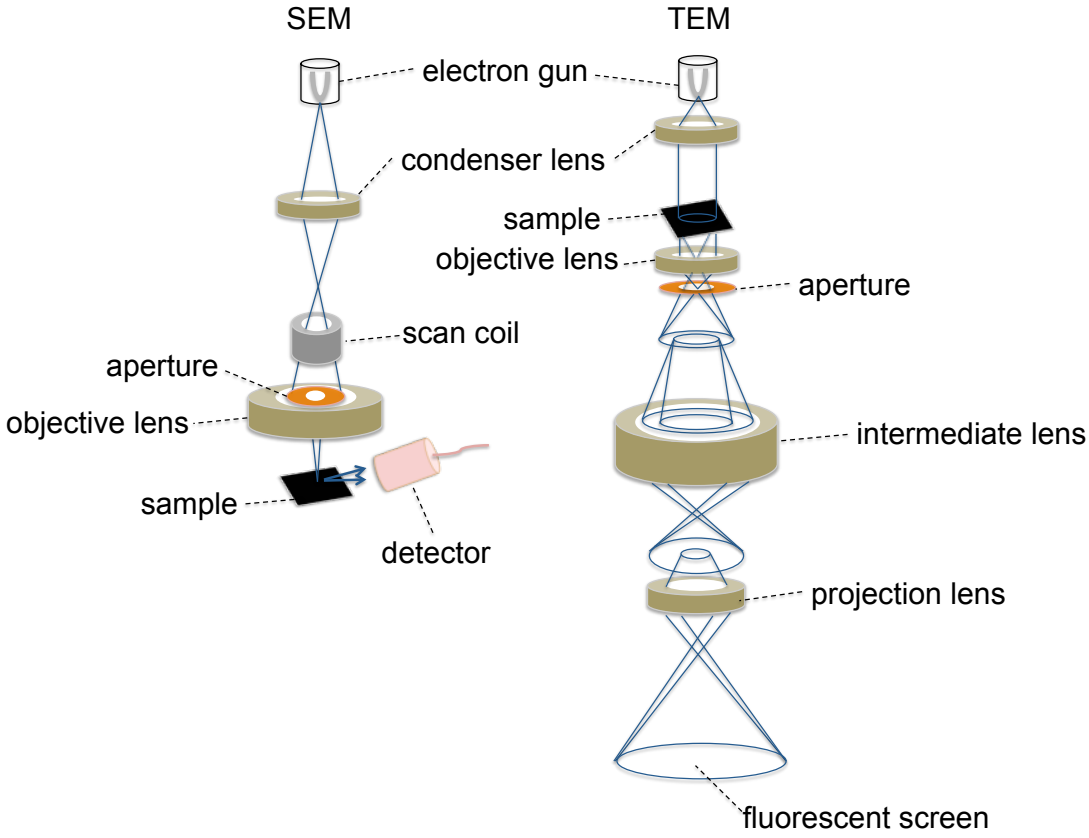

Figure 2-4 The schematic view of SEM and TEM.

2-5. Photo-electrochemical measurement [G. Hodes, 2012]

The three electrode system is the common setup of an electrochemical analysis such as voltammetry, composed of working electrode, reference electrode, and counter electrode in the electrolyte solution. Voltammetry is the technique to measure the relation between voltage and current by electrolyzing the sample as a working electrode, where the external voltage is applied between the working electrode and the counter electrode. Since solution resistance causes voltage drop, the working electrode potential is not accurate nor stable in the two electrode system. In the three electrode system, the voltage of the working electrode relative to reference electrode is controlled by potentiostat, so the electrochemical reaction voltage can be measured precisely. Cyclic voltammetry provides the redox potential of the chemical species on the working electrode, where the applied potential of the working electrode is swept in constant speed. When the potential of working electrode is swept to the positive potential, the current-voltage curve provides oxidation peak, while redox peak is available when swept to the negative potential.

In the case of photoelectrochemical measurements, the light is irradiated to the working electrode; historically the photocurrent is measured in dye-sensitized solar cells by photoelectrochemical measurement. Since the photoelectrode generates the anordic photocurrent, the current-voltage curve is enhanced when the light is irradiated compared with the dark condition, and the three electrode system is suitable to measure currents of the order of μA to nA stably.

2-6. Finite domain time difference analysis [K. Yee, 1966]

Finite-difference-time-domain method is a computational method to simulate the electromagnetic field by solving Maxwell equation;

$$\nabla \times E(r,t) = -\frac{\partial B(r,t)}{\partial t}$$

$$\nabla \times H(r,t) = \frac{\partial D(r,t)}{\partial t} + J(r,t)$$

$$\nabla \cdot D(r,t) = \rho(r,t)$$

$$\nabla \cdot B(r,t) = 0,$$

where $E(r, t)$, $B(r, t)$, $H(r, t)$, $D(r, t)$, $J(r, t)$, $\rho(r, t)$ are the electric field, the magnetic flux density, the magnetic field, the electric flux density, the electric current density, respectively, at coordinate r and time t. In order to solve the equation computationally, both time and space are divided into discrete segments. The space is subdivided into small computational cells, called Yee-cell, of the scale smaller than $\lambda/10$, where λ is the wavelength of electromagnetic wave (light). As shown in Figure 2-6, the magnetic field and electric field are stored at face centers and edges of each cell, respectively. The time step is set smaller than the timescale for the electromagnetic wave (light) to propagate from one cell to the next. The curl operation of the electric and magnetic field is calculated in turn at each time step, which is called leap-frog algorism. Since many small cells compose three dimensional shapes, FDTD enables us to calculate electromagnetic field of a complex structure.

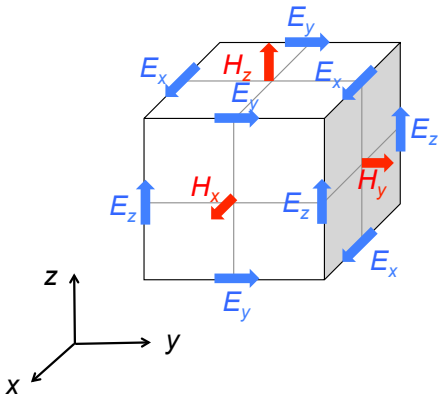

Figure 2-6 The configuration of Yee-cell.

Chapter 3: Fabrication and structural measurement of Ag-Co-TiO_2 nanocomposite films

3-1. Introduction

Metal nanocomposite films have received much attention, due to their interesting electromagnetic properties, as mentioned in Chapter 1. Thin film fabrication techniques, such as pulsed laser deposition (PLD) and molecular beam epitaxy (MBE), has been established as powerful tools for fabricating composite materials, where the shapes and sizes of nanostructures has been controlled by various experimental parameters, such as the amount of Cu in case of Cu-Al_2O_3 [R. Serna, 2001], and substrate orientations in $CoFe_2O_4$-$PbTiO_3$ ceramic composite films [I. Levin, 2006]. In addition, Seeking novel optical and catalytic properties, Resta *et al* embedded Au nanoparticles into a MgO single crystal with a high nucleation rate, in spite of the low lattice mismatch between rock-salt MgO and Au [V. Resta, 2009]. On the other hand, numerous studies have been made on wide-gap semiconductor thin films doped with magnetic ions to explore room temperature ferromagnetic semiconductors and it was often encountered that the magnetic properties differ from a researcher to another [B. Sanyal, 2009]. It has been argued that such inconsistency results from inhomogeneous distribution of the metal dopants. Thus, both theoretical and experimental studies have focused on metal nanostructures in semiconductor films, such as Co clusters in ZnO or TiO_2, and Ni nanocrystal in $BaTiO_3$ [D. Iuşan, 2009][F. F. Ge, 2010]. The anatase Co-TiO_2

films deposited by PLD using a sintered polycrystalline $Ti_{0.96}Co_{0.04}O_2$ target showed room temperature ferromagnetism originating from the Co metal nanoclusters, when the films were fabricated at low oxygen pressure (~ 10^{-6} Torr), [D. H. Kim, 2002][G. S. Chang, 2006]. Meanwhile Co metal nano clusters were not formed in the films prepared at relatively higher oxygen pressure. It was recently reported that the average size and density of Co metal nanoparticles in anatase TiO_2 films were controllable by carefully adjusting film growth conditions, such as substrate temperature and oxygen partial pressure [K. Ikemiya, 2011]. It was suggested that Co metal particles segregate during the film deposition without being oxidized because TiO_2 has stronger oxygen affinity than Co. TiO_2 is a good candidate for a matrix material that can disperse nanostructured metals; it was predicted that other metals, such as Fe, Ag, and Ni, could also be segregated by simple PLD deposition procedure. Ikemiya *et al*. tried to fabricate Co:TiO_2 film containing Ag nanostructure, expecting that Ag nanostructures would emerge and enhance/affect the magneto-optical properties [K. Ikemiya,2014]. As a result, they found unexpected characteristic metal nanostructures composed of Ag and Co. The STEM-EDX image revealed that self-assembled Ag nanorods grew on Co nanospheres were embedded in anatase TiO_2 films. Furthermore a LSPR-like peak was observed in the absorptance spectra, although its shape and location have not been rationalized by electromagnetic calculation in detail. As Ag nanostructures are known to induce strong surface plasmon resonance in the visible region, which is a

characteristic property of noble metal nanoparticles, I focused on the Ag-Co-TiO_2 composite films as a new plasmonic material. The Ag-Co nanostructure has an advantage that it is already combined with TiO_2 matrix, which is useful for stabilizing the Ag nanostructure. As is well known, Ag nanostructures are chemically unstable and preferable to be protected from ambient air [R. Seoudi, 2011][H. Im, 2011]. Particularly, the protective dielectric generally improves optical properties [Y. J. Jen, 2014]. Since the Ag-Co nanostructure with a “nanomatch”-like shape was discovered by chance, the reproducibility to prepare the nanostructures was not confirmed in a nanometer scale. Additionally, before their practical uses, it should be thoroughly investigated how the structures of the Ag-Co nanomatches and their plasmonic properties are affected by the film growth conditions. In this chapter, I established the methods to fabricate the Ag-Co nanomatch structures, especially focusing on the Ag nanostructures. I also present the tendency of plasmon resonance peak to the Ag nanostructures in the Ag-Co-TiO_2 system, and proved that the optical absorbance of the film resulted from the localized surface plasmon resonance based on numerical simulation.

3-2. Experiments

3-2-1. Thin film fabrication

PLD target was made by mixture from Ag_2O, CoO and TiO_2 with molar ratio of Ag:Co:TiO_2 = 20:5:95, heated at 900 °C for 12 hours under the atmospheric condition. The density of the greenish-white-color sintered target, $Ag_{20}Co_5(TiO_2)_{95}$, was 74.6 %. Since it was empirically known that anatase crystal can be formed at low temperature by the anatase seed layer, pure TiO_2 layer was firstly deposited on $LaSrAlO_4$ (LSAO) (001) substrate for 10 minutes, at substrate temperature T_S = 650 °C under an oxygen pressure P_{O2} = 5×10^{-3} Torr by pulsed laser deposition (PLD). Next, the temperature was once cooled down to be room temperature and raised again up to T_S = 650 °C under an oxygen pressure P_{O2} = 5×10^{-3} Torr. Then in consecutive manner, Ag-Co-TiO_2 film ($Ag_{20}Co_5(TiO_2)_{95}$ film in nominal composition) was deposited on the seed layer at T_S = 300 °C under P_{O2} = 1×10^{-7} Torr for 60 minutes with the $Ag_{20}Co_5(TiO_2)_{95}$ target. I hereafter describe the compositions of the Ag-Co-TiO_2 films using the nominal compositions of the targets, as $Ag_{20}Co_5(TiO_2)_{95}$. Both layers were deposited with KrF excimer laser (wavelength 248 nm), operating at 2 Hz and with energy 18 mJ/pulse. For comparison, a thinner and thicker films of $Ag_{20}Co_5(TiO_2)_{95}$ (in nominal composition), a bilayer film of $Ag_{20}(TiO_2)_{95}$ film (in nominal composition) on $Co_5(TiO_2)_{95}$ film (in nominal composition), using two sintered target sequentially for 60 minutes each, $Ag_{20}(TiO_2)_{95}$ target and $Co_5(TiO_2)_{95}$ target. The excessively Ag doped film of $Ag_xCo_5(TiO_2)_{50}$ (x = 100,

200) (in nominal composition) were also fabricated (using sintered target of Ag_x $Co_5(TiO_2)_{50}$), all on the same seed layer.

Their crystal structures were measured by X-ray diffraction (XRD), and the absorptance spectra were measured by UV-vis spectroscopy, where (absorptance) = 100 % − (transmittance) − (reflectance).

The surface morphology was measured with scanning electron microscopy (SEM) (JEOL, JSM-7001FA) with the aid of energy dispersive X-ray analysis (EDX) and atomic forced microscopy (AFM). The cross-sections of nanostructures were imaged by transmission electron microscopy at 200 kV of acceleration voltage (JEOL, 2010-HC, 2100F, JEM-2800).

3-2-2. Sample preparation of transmission electron microscope measurement

In order to observe the nanostructures by transmission electron microscope (TEM), the sample should be enough thin for the electrons to pass through: generally less than 100 nm in thickness. When the sample was too thick, the obtained image would be blurred, thus thinning process is the most crucial for obtaining sharp-contrast images. Various methods to prepare TEM samples have been developed so far; for instance, in case original samples are small enough, such as powders, they are dispersed on a microgrid with a supporting film (not to overlap each other). Meanwhile, the fragile biological organic samples are prefixed then embedded in amorphous ice, or the replication is made. Thermally weak samples or soft metals are directly cut by a diamond knife, which is called microtomy. However, my samples were thin films of several tens of nm in thickness on stiff oxide crystal substrate of mm-sized order. For their cross-sectional observations, ion milling is suitable because the samples could endure the process accompanying generation of heat.

There are two major thinning process for crystal samples. The first and easier one is focused ion-beam milling (FIB), which I tried first (SII, Xvision) in this study. A focused gallium ion beam accelerated at several to 40 kV, can quarry μm-order samples. With the help of scanning electron microscopy, the place and size to cut were controlled very well. To prepare a sample for cross-sectional TEM observation, the three sides were etched and inclined at a shallow angle by tilting the sample, and then the bottom part was cut; only one side remains. The

sample was attached to a metallic needle by the carbon deposition then the remaining one side was cut by gallium ion beam. Subsequently, the sample was picked up by the metallic needle (Figure 3-2-2-1).

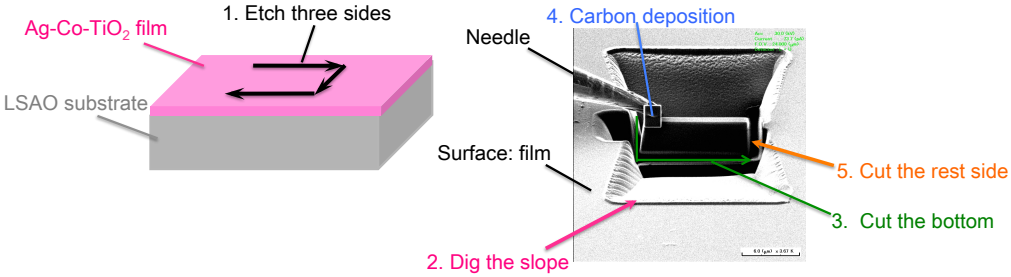

Figure 3-2-2-1 Schematic pictures of FIB process. (Thickness: several μm.)

At last the needle transfer the sample to the single hole mesh, then the mesh and the sample were adhered by the carbon deposition, followed by the separation of the sample from the needle. The problem in FIB thinning was that the strong gallium ion beam causes damage to the sample, creating an amorphous layer on the surface. During the crystal structure observation, the image of this amorphous layer is always overlapped, preventing detailed analysis of atomic images intrinsic to the original samples. Moreover μm-order thick sample was too thick to be observed in TEM, thus the etching with milder condition, i.e. smaller accelerating voltage of Ga ion beam and then milder Ar ion milling (2 kV), was needed. From both sides, through which electron goes in TEM, milder etchings were repeated until the thickness of the sample becomes

~ 100 nm. (If there is a Ar ion milling machine for the completing TEM sample, called nanomill whose argon ion beam size is as small as 1 μm, the gentle etching and Ar ion milling in FIB can be taken place by the Ar ion milling by nanomill.) The thinning by FIB was fast (~several hours) and easy to obtain the skills because all processes were automated. However, the TEM sample prepared for my films by FIB were too thick to obtain clear TEM images, though the samples had thickness less than 100 nm according to SEM observations. Without nanomill treatment, there is a limitation for the thickness of the sample and it takes long time to mill the sample until it becomes enough thin.

Thus I thinned my Ag-Co-TiO_2 film by hand/mechanical polishing and argon ion milling. The obtained TEM sample had distribution in thickness, which was suitable for my study, since the region with the best thickness would be chosen during the TEM observation. The TEM sample preparation recipe is dependent on the material the configurations of samples, however the detailed information given in this section would be generally used for the thin film samples on oxide crystal substrates.

My original sample size had a dimension of 5 mm x 5 mm x 0.5 mm, and it should be ~ 100 μm-thick before argon ion thinning. I first cut the sample into rectangular slices and then performed hand polishing. However, the oxide substrates of $LaAlSrO_4$ (LSAO) (001) was so fragile in the cross sectional direction, i.e. perpendicular to the layer-by-layer crystal structure, that the substrate easily cracked while polishing, especially detached at the place just

near from the film (Figure 3-2-2-2).

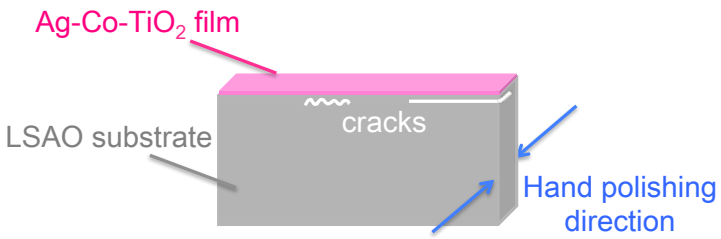

Figure 3-2-2-2 Crack positions generated during the hand polishing were indicated.

For the easier polishing, several ways are known to protect the surface film: coating the film with adhesive, embedding in resin, sticking the same two samples on each of their film surface to each other, and sticking the substrate (used in the original samples, glass, silicon, etc.). Though I tried the adhesive coating first, the protection was not enough; just some parts of the film were remained in island-shape. Then I succeeded in polishing into 100 μm depth by sticking the same two samples at film sides, but the success rate was not so good until my hand polishing skill improved. So I tried the way of sticking substrates of silicon wafer, since the similar etching rate (softness/fragility) should be chosen. It was experimentally clarified by my experiments that both thickness of the dummy silicon and the thickness of the adhesive (epoxy, G2) between sample and the dummy were important; I found out the desirable conditions by try and errors. The proper thickness of Si dummy and G2 were 20~30 μm and less than 5 μm, respectively; the thinner thickness caused the

adhesive peeled off, and the larger thickness took more than 20 hours in the latter argon ion thinning process.

The full processes for preparing a typical cross-sectional TEM sample making are as follows. The ultrasonically cleaned original sample was attached on 250 or 500 μm-thick- silicon substrate by epoxy resin, G2. Bubble in G2 was eliminated then G2 was thermoset (80°C 10 min, then 150°C 60 min), while the sample and the silicon substrate were pressed together. Then I cut the Si dummy attached sample into rectangular slices of 2.8 mm (width) x 300 μm (depth) x (original height) by the automated precision diamond cutter (JEOL, Isomet). The thickness (depth) of the rectangular slices was optimized as 300 μm through try and error (in a range of 100 μm to 1 mm). Smaller thickness leaded the delamination of the crystal layer of substrates just below the film surface, and larger ones required many times of grinding which caused more damages in the following hand milling process.

The thin sliced sample with silicon dummy was attached to glass plate with wax. Only silicon substrate was thinned in the plain view direction by hand polishing with diamond polishing film (JEOL, diamond wrapping film, 9 μm) and the surface grinder (JEOL, HLA-2), until the dummy Si layer became 20~30 μm (Figure 3-2-2-3).

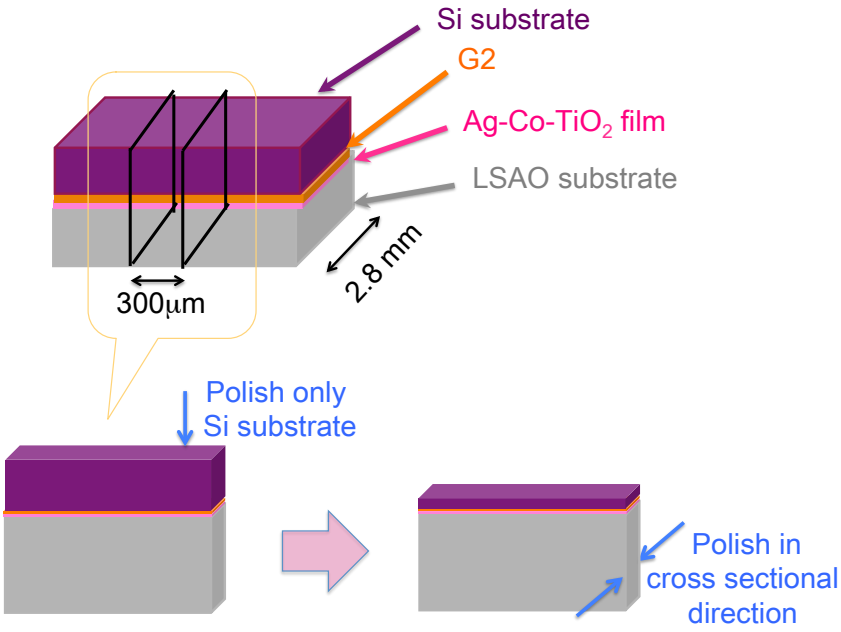

Figure 3-2-2-3 Procedure of the hand polishing, clarifying the polishing direction. (Thickness: initially 300 μm then polished until ~ 100 μm.)

Then the protected sample was once taken off on the hot plate (~130°C), and was laid on the glass plate again, attached by wax. Next the both sides of cross sectional direction of the protected sample were polished into 100~110 μm depth by hand polishing with diamond polishing film (JEOL, diamond wrapping film, 1 μm) and the surface grinder (JEOL, HLA-2). This thinning process by hand is very delicate task and it took one year for me to obtain the skill. (As getting used to polishing, I came to know whether the sample was gently polished, the timing of clogging of wrapping paper, and the approximate thickness of the sample, just by the touch sense and the sound during polishing.) The polishing film was often wiped with water and nonwoven fabric wiper

(BEMCOT), since the shaving damaged the sample.

After the hand polishing, the protected sample was removed gently from the grass plate and wiped carefully by the cotton buds and ethanol so that no wax remained. Cleaning the protected sample here reduces the re-deposition of impurities in the latter argon ion thinning process, however, too much wiping without handling skills would often destroy the sample. Next it was fixed on the sample holder of the Ion Slicer (JEOL, EM-09100IS) with wax. The Ion Slicer (IS) is the thinning machine, which had single argon ion gun. Both the gun and the sample holder were movable in back and forth, right and left drawing a circular arc, respectively, the sample was thinned from two directions. Thus the thinned sample had gentle gradient of thickness in the horizontal direction as shown in Figure 3-2-2-4. IS with characteristic belt, paved the way to prepare fragile samples without mechanical polishing. (The components of the shield belt were also checked by SEM-EDX measurements, Figure 3-2-2-5.)

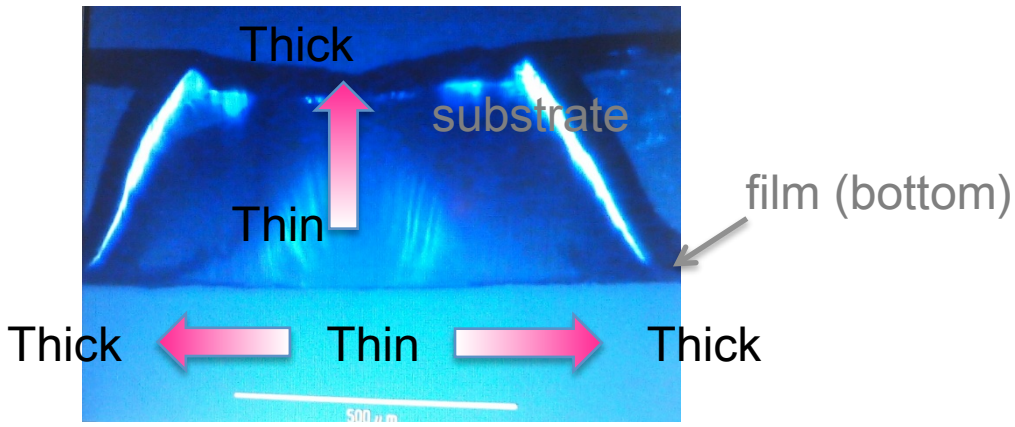

Figure 3-2-2-4 Typical thickness gradient of the sample treated by IS.

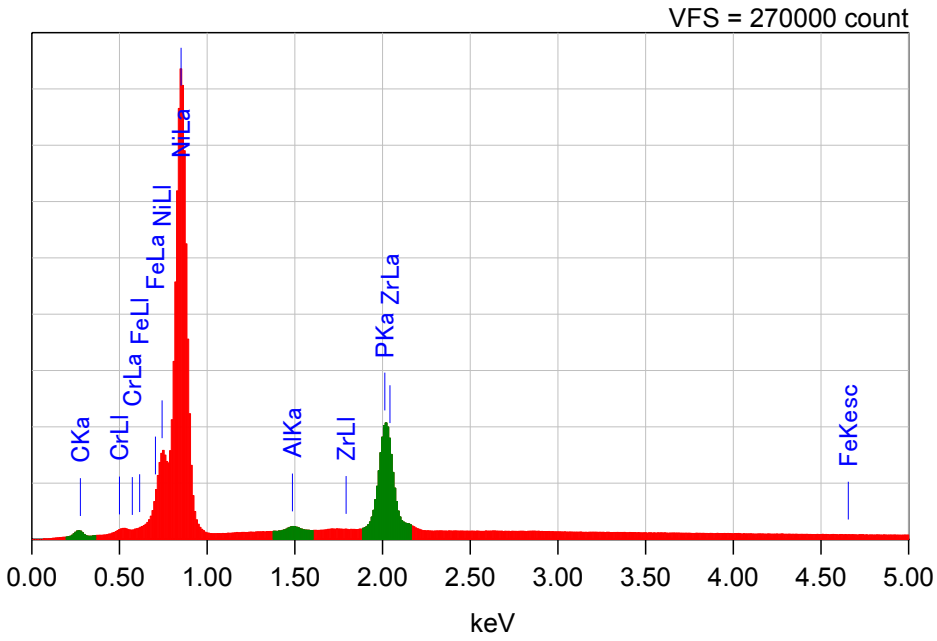

Figure 3-2-2-5 SEM-EDX spectrum of the shield belt, indicating that it was mainly made of Fe and Ni.

First, the shield belt masked the silicon dummy side (film side) and the argon ion beam polished the sample in waged-shape from the top; only the place directly under the belt (~ 10 μm) was left as it was, instead of mechanical polishing. The argon ion beam was accelerated at 6.5 kV at 0°. Then I removed the shield belt and turned the sample holder upside down. Here the second thinning was performed under the condition of acceleration voltage of argon ion beam (E_{ion}): 4.5 kV, the swing angle of argon ion beam (θ_{ion}): 4.5° from the front/back side alternately for 1 minute each (Figure 3-2-2-6).

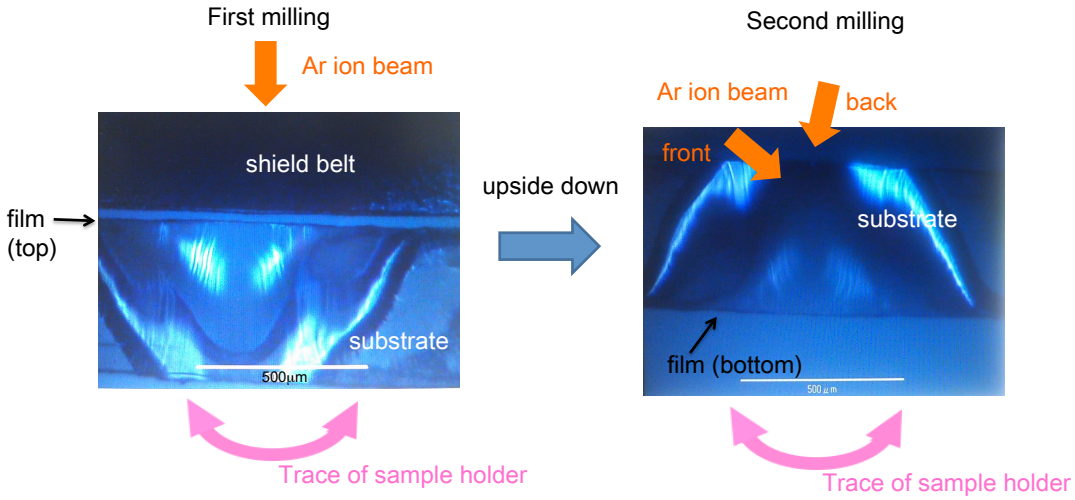

Figure 3-2-2-6 The general geometrical configurations of the first and second step of Ar ion milling in IS.

The substrate side remained thick even after the first polishing, thus the film side was gently milled by the argon ion beam at high angle. The center position of the film side became the thinnest part, so I finished the Ar ion milling on the point of the orifice appearing on the film surface, i.e. the sample thickness of the orifice

or just around the orifice was infinitively thin. To create good thin TEM sample, when to stop the argon ion thinning was very important. Normally the last step of the thinning was checked by optical or electron microscopes; in case the thinning was not enough, the sample was additionally thinned. Although the timing to stop the argon ion beam was difficult to judge, the interference pattern appeared and the thinnest part started blinking just before the orifice appeared. The orifice gradually got bigger with the longer etching time. Since the film surface was covered with silicon dummy, the orifice normally appeared at the silicon dummy place at first and then it was extended to G2, film, and reached to substrate place at last. It took less than 18 hours and about 12hours for samples with LSAO substrate and Nb:STO substrate, respectively. Then the protected sample was gently milled under the condition of E_{ion}: 1~2 kV, θ_{ion}: 5°, in order to eliminate the surface damage. It was noteworthy that the samples made of different components would have different etching rates. Generally the thinner the better for the TEM sample, however, the too thin place sometimes did not reflect the intrinsic nature of sample because only low-etching-rate component remained there and most of the high-etching-rate components were missing.

After the thinning by IS, the C-shape single hole mesh was fixed to the milled sample with araldite, that is, the sample was sandwiched by the IS holder and the mesh. Then the TEM sample with a mesh was removed from the IS sample holder by heating the wax between protected sample and the holder (Figure 3-2-2-7).

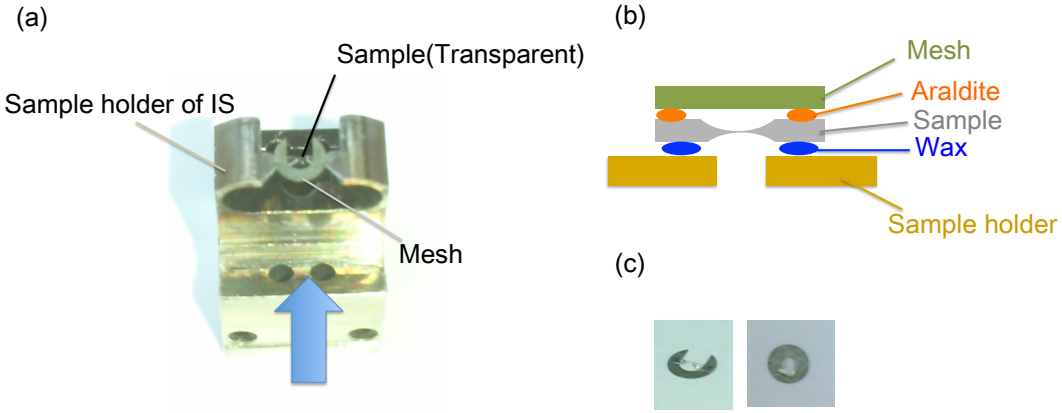

Figure 3-2-2-7 (a) The photo of mesh attaching process to IS polished sample. (b) The schematic configuration in detail was depicted from cross sectional direction (blue arrow in (a)). (c) The TEM sample of cross section (left) and plain view (right) for reference.

The sample surface just after the removal was coated by rough wax, which often caused the cracks during the sample fixing to the TEM sample holder. The wax was smoothed by sliding on the wrapping paper used for powdered medicine, on the hot plate for 30 seconds to 1 minute. This sample was used for the TEM observation after cleaned by the ion cleaner (JEOL, EC-52000IC).

Strictly speaking, the time for the argon ion thinning was different by an hour to two hours, from a sample to another, even though they were prepared from the same film sample. It is possibly due to the subtle but uncontrollable difference in the thickness of G2 and silicon dummy, tilting angle or thickness of the sample, surface roughness, and the small dust on the top or the invisible cracks made at hand polishing, tilting relative to the IS sample holder during the

fixation procedure. Longer time etching here not only cause re-deposition (Figure 3-2-2-8) but also lead to the high-pitched sample whose thickness drastically changes from the film part to substrate part.

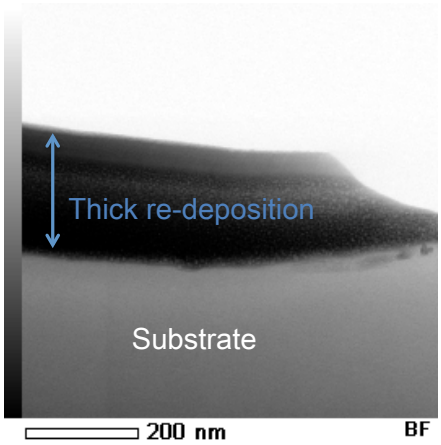

Figure 3-2-2-8 Example of the thick re-deposition on the surface of the sample. During the argon ion beam thinning, not only etching but also deposition of etched things took place.

Practically, the thinning speed of the film place to obtain orifice sometimes slower than the etching rate of the substrate side so that the cave of the substrate side tend to reach the other side first, which made the sample more fragile (Figure 3-2-2-9).

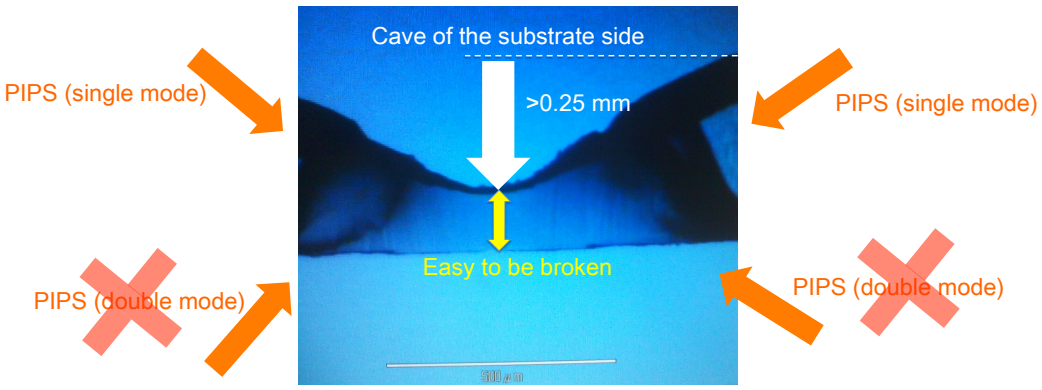

Figure 3-2-2-9 Substrate side (upper) is also etched during the etching of the film side (lower). This picture is the example of the large cave of the substrate side, which weakens the strength of samples. The Ar ion beam directions of following PIPS treatment are also explained; only upper two arrows of single mode, and all four allows of double mode.

Under such circumstances, I stopped the Ar ion milling by IS (when the height of cave of the substrate side was more than the half height of the sample, 0.25 mm) and took the sample out from IS, then put it to Precision ion polishing system (PIPS). PIPS (Gatan) is the ion milling with double Ar ion beams, whose irradiation angle can be set wider and irradiated position can be set more precise than IS. I adjusted θ_{ion} at 5~6° and E_{ion} was set to 3.5kV for the further polishing, the value of E_{ion} and θ_{ion} were again optimized by trial and errors. For the cross-sectional observations, the single mode should be used so that the ion beam direction was uniformed from substrate side to the film side, i.e. the beam was on during half rotation of the sample and off in the next half. In PIPS, the two

argon ion guns were settled, while the sample holder rotated. During the thinning process of PIPS, I fixed the protected sample to the holder by wax, without single C-shape single hole mesh made of Mo. Although the handling became more difficult, the polishing without mesh prevented the sample from re-deposition from the metal mesh.

I also succeeded in making the cross sectional samples on the Nb:STO substrate with PIPS after the mechanical polishing, although the handling was more difficult than with IS. Two slices from the exact same film were glued each other at the film side, then polished in the totally same procedures of the plain view samples, as described below. The cross sectional TEM samples thinned by PIPS only were cleaner and had more gentle slopes from film to substrate than IS made samples. I found that PIPS would be better than IS when the sample was stiff enough to be mechanically polished; PIPS after mechanical polishing was suitable for the samples with Nb:STO substrates but not for those with LSAO substrates.

Next the TEM sample making of plain-view observations were prepared as follows. As shown in the Figure 3-2-2-10, the ion polishing was performed only from the substrate side, until the substrate disappeared or the orifice appeared.

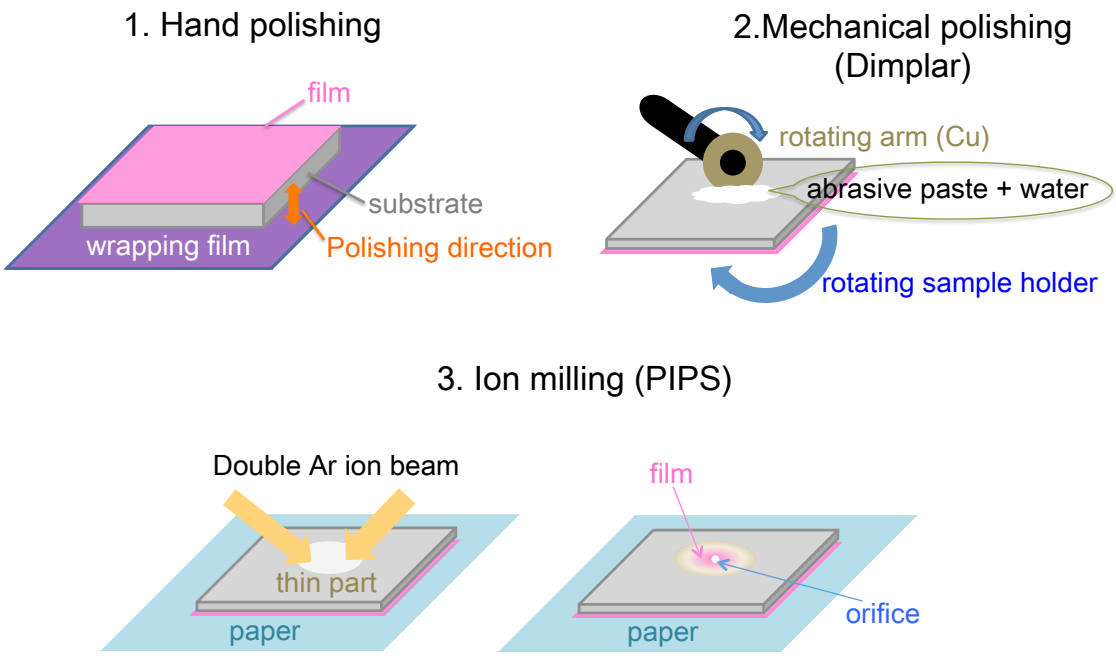

Figure 3-2-2-10 Explanatory diagrams of plain view TEM sample preparation.

The protection of the film surface was not needed because the argon ion beam never came from the film side. I used PIPS (Gatan) in the plain-view sample because even LSAO (001) substrate was tough in the plain-view direction enough to stand the mechanical polishing. Moreover PIPS was suitable to dig a large and shallow hole conically, because it uses double argon ion beam set at low angles.

First I cut the original film on the substrate into the size fitting to the O-shape single hole mesh by ISOMET: 2.0 mm (width) x 2.0 mm (depth) x (original height). Then it was fixed to the glass plate on the film side by wax, and hand polished until its thickness became ~ 50 μm with the surface grinder (JEOL, HLA-2) and diamond wrapping film (9 μm then 1 μm). Next the sample was

mechanically polished by the Dimple grinder (Gatan, 656 Dimple grinder) until the thickness became 20 μm; this process reduced the thinning time with PIPS. Both the sample holder and the Cu arm rotated to create the shallow hole as shown in Figure 3-2-2-10; alumina abrasive paste of 0.3 μm was used. The weight on the arm and the rotating speed should be controlled (I set the dials of weight and speed at 18 and 2, respectively). As the finishing of Dimpling, I buffed with alumina abrasive paste of 0.05 μm. After dimpling, the sample was removed from the grass plate and attached to the O-shape single hole mesh with araldite. The mesh was attached by araldite to reinforce before PIPS treatment. The sample and the wrapping paper of medicine was fixed together to the string type holder of PIPS; I put the wrapping paper on the film side to avoid the re-deposition on the film surface, during the Ar ion milling. The focus points of two argon ion beams was adjusted to the center position. Then the protected sample was gently milled under the following condition, E_{ion}: 4.5 kV, θ_{ion}: 4~5°, with double mode. Smaller angle would lead to the shallower samples, however, Ar ion beams would did not focused sharply onto the aiming spot, and thus I slightly adjusted the angle depending on the etched shape and speed of etching. Similar to the ion milling in IS, I finished the thinning by PIPS when orifice appeared. It usually took about 5 hours in milling, although the time tends to become longer as the samples after mechanical polishing became thicker. An interference pattern appeared and subsequently the thinnest part started blinking just before the orifice appeared. Then surface was gently milled for ~ 5

min (E_{ion}: 2 kV, θ_{ion}: 3°). PIPS treated samples were used for the TEM observation after cleaned by the ion cleaner (JEOL, EC-52000IC).

3-3. Results and discussion

3-3-1. Structural and optical evaluation

In order to utilize the Ag nanostructures, it should be prepared with good reproducibility. First I tried to reproduce the Ag-Co nanomatch-like structure using the same film growth condition as that in the previous study: an $Ag_{20}Co_5(TiO_2)_{95}$ film was deposited under the condition of T_S = 300 °C and P_{O2} = 1×10^{-7} Torr for 60 minutes with the $Ag_{20}Co_5(TiO_2)_{95}$ target. The surface morphology of the obtained film was shown in Figure 3-3-1-1.

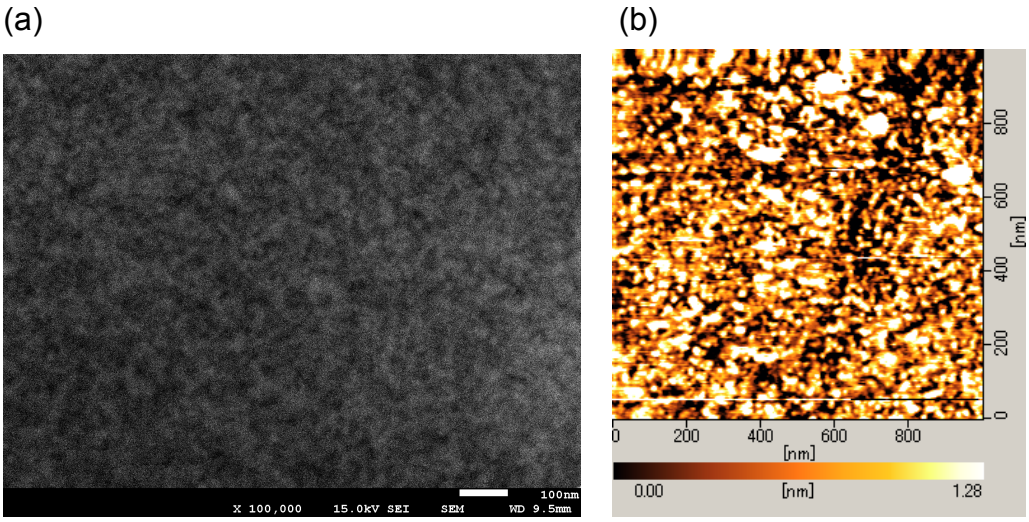

Figure 3-3-1-1 Surface morphology of the $Ag_{20}Co_5(TiO_2)_{95}$ film (60min deposition), (a) SEM, (b) AFM.

The film surface of the film had no clear nanostructures, but was relatively smooth with roughness of ~ 1nm. From the SEM image, some obscure structures sticking out of the surface (white regions) are recognizable, suggesting the segregation of something on the surface. A small amount of Ag

was detected while Co was not detectable from the SEM-EDX spectrum of $Ag_{20}Co_5(TiO_2)_{95}$ films (60min deposition) as shown in Figure 3-3-1-2. It can be assumed that Ag and Co were locally segregated to form small nanoparticles whose amount is below the detection limit of SEM-EDX.

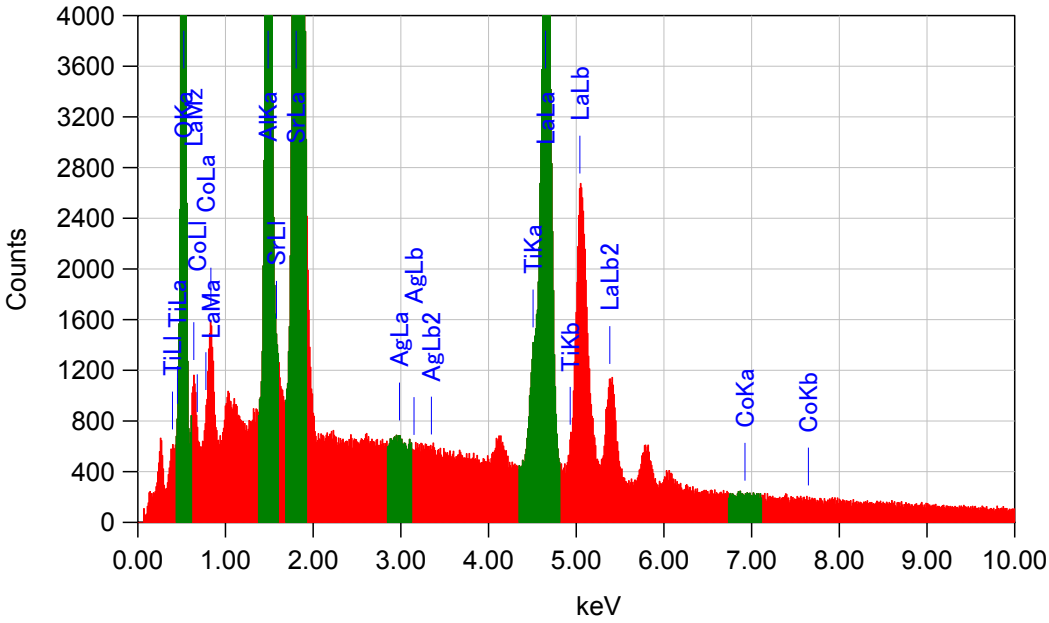

Figure 3-3-1-2 SEM-EDX spectrum of $Ag_{20}Co_5(TiO_2)_{95}$ film (60min deposition).

In order to know whether Ag/Co nanomatch structure was formed, the cross-sectional STEM-EDX image was obtained. In this study, I prepared all TEM samples by myself in order to investigate the structural variation of the nanostructures in detail as a function of thin film growth condition. However the oxide substrates with layer-by-layer structure was difficult to thin down in the direction perpendicular to the layer, I had to spend almost one year until I could make good TEM samples. Details about the sample preparation procedure were

described in the previous Section 3-2-2. The sample prepared by FIB was too thick to be observed by TEM, thus all TEM samples were made by ion beam milling method in this study. The cross-sectional HAADF-STEM-EDX images (Figure 3-3-1-3) of the $Ag_{20}Co_5(TiO_2)_{95}$ film (60min deposition) exhibited that the Co metal nanospheres were located just above the seed layer and that the Ag nanorods grew from the Co nanospheres in a self-assembled manner.

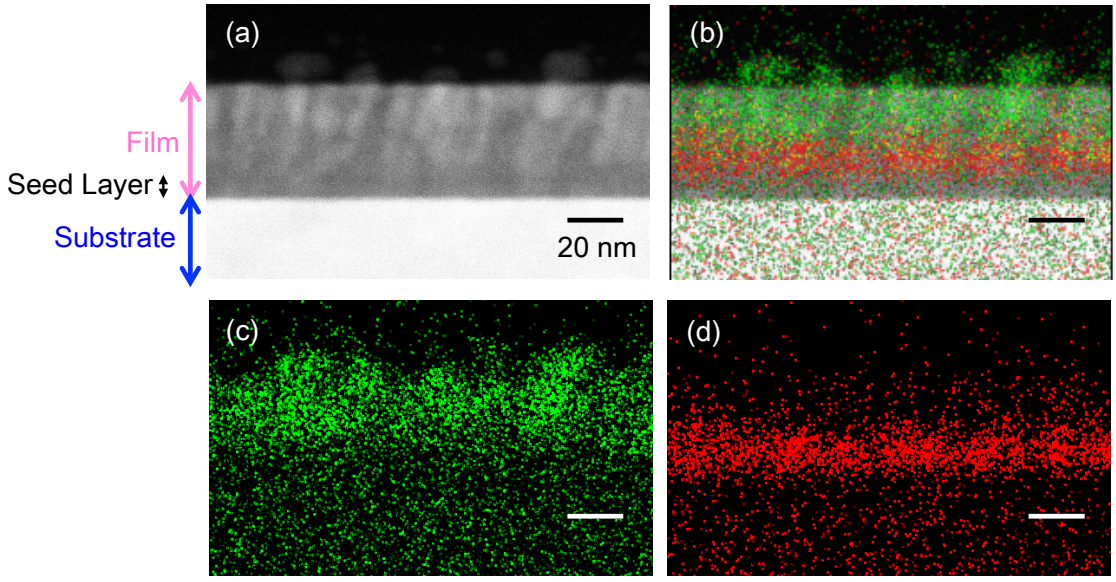

Figure 3-3-1-3 Cross-sectional (a) HAADF-STEM and (b) HAADF-STEM-EDX image overlapped on HAADF-STEM image, of the $Ag_{20}Co_5(TiO_2)_{95}$ film (60min deposition). Ag and Co were depicted with green and red color, respectively: (c) only Ag and (d) only Co mapping images. Scale bar indicated 20 nm. (The TEM used for the measurement was JEOL, JEM-2800.)

The typical film thickness was ~ 40 nm, including ~5 nm-thick seed layer. The typical radius of Co nanosphere was ~ 10 nm in diameter, and the Ag nanorods were ~ 20nm in height and ~ 5 nm in diameter, which agree well with those previously reported. Thus, the characteristic Ag/Co nanomatch structure was well reproduced in this study. Moreover, the nanomatches was distributed in the TiO_2 matrix in a uniform manner, i.e. nanomatches with almost the same size were distributed with a nearly constant interval of sub-micron scale, though the Ag nanorods slightly tilted from the film normal (Figure 3-3-1-4). Here, the word “reproducible” implies that the characteristic Ag/Co nanomatch structure with ~5 nm in diameter and 10-20 nm in height was obtained in TiO_2 matrix several times, regardless of the film thickness.

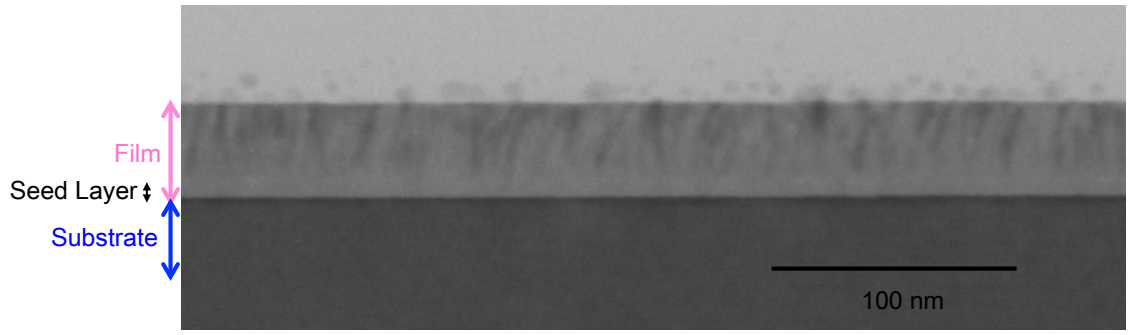

Figure 3-3-1-4 Wider area (several hundreds nm) image of cross-sectional bright field STEM image of $Ag_{20}Co_5(TiO_2)_{95}$ film (60min deposition). (The TEM used for the measurement was JEOL, JEM-2800.)

The relatively black color regions in the bright field STEM image, corresponding to the white regions in the dark field image (Figure 3-3-1-3 (a)), were assigned to the Ag/Co nanomatches by the EDX analysis. It is noteworthy that the top part of the Ag nanorods protruded onto the film surface, as clearly seen from the larger scale image. The density of Ag nanorods seemed high and the EDX images did not show clear edges because the TEM sample was still thick.

Since the reproducibility was confirmed, I examined the Ag-Co nanostructures in the films fabricated under different PLD conditions, as the next step. Composite films were fabricated at half (30 minutes) and twice longer (2 hours) deposition time were made, whose typical thicknesses were ~ 20 nm and ~70 nm, respectively. In the cross-sectional HAADF-STEM image of the $Ag_{20}Co_5(TiO_2)_{95}$ film (30 min deposition), oval or spherical nanostructures were observed instead of the Ag/Co nanomatch structure (Figure 3-3-1-5). The nanoparticles were too small to perform local EDX analysis so that an EDX spectrum was measured for the whole nanoparticle (Figure 3-3-1-6, point 2).

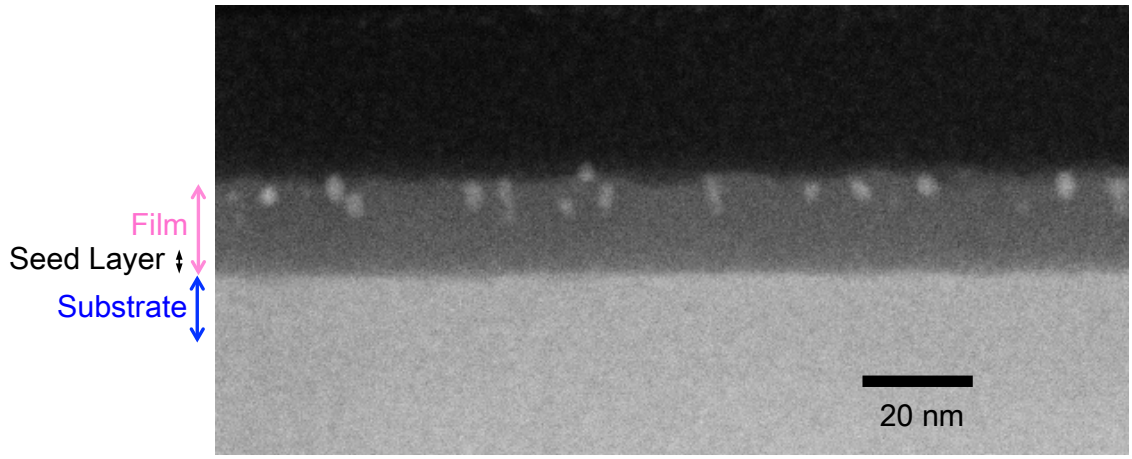

Figure 3-3-1-5 Cross-sectional HAADF-STEM image of the $Ag_{20}Co_5(TiO_2)_{95}$ film (30min deposition). (The TEM used for the measurement was JEOL, JEM-2800.)

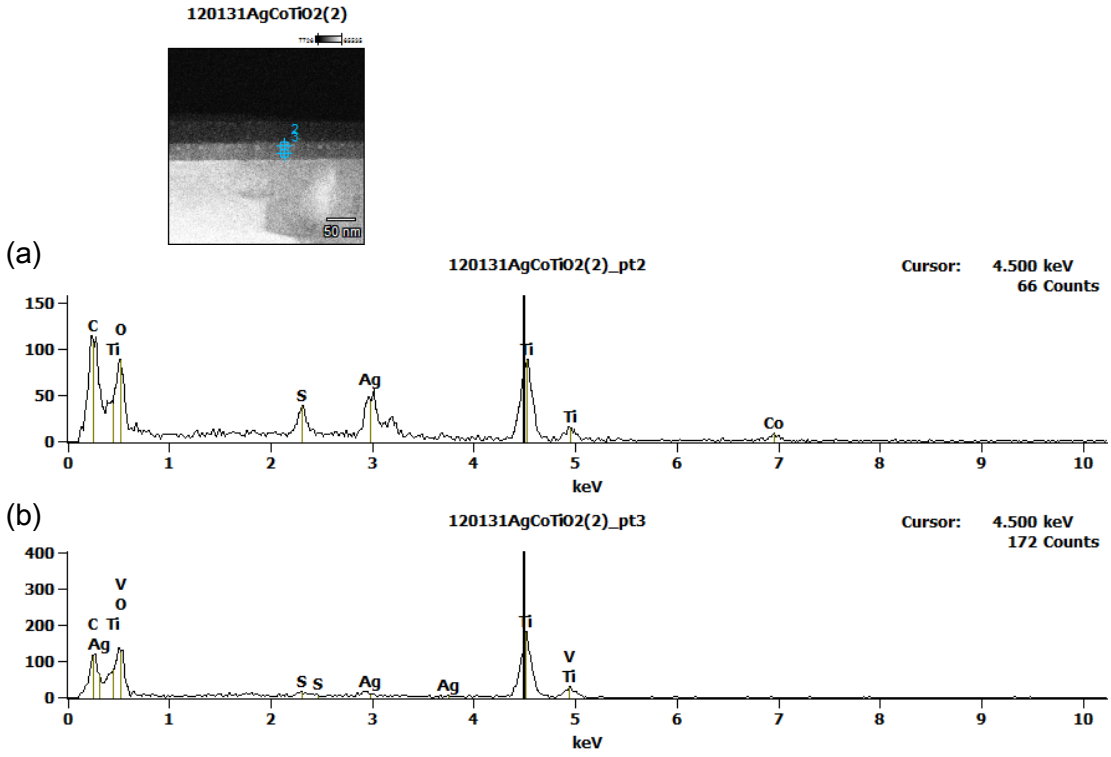

Figure 3-3-1-6 EDX spectrum of the $Ag_{20}Co_5(TiO_2)_{95}$ film (30min deposition), on the point of (a) the white nanoparticle, point 2 (pt2), and (b) no particle, point 3 (pt3), in the upper HAADF-STEM image. (The TEM used for the measurement was JEOL, JEM-2800.)

As a result, it was found that the particles were mainly composed of Ag with small amount of Co. The Ti and O peaks seen in the spectrum originated from TiO_2 matrix adjacent to the particle. The C and S signals were thought to be come from the epoxy adhesive used to protect the film surface during the TEM sample preparation, since the amount of S was too large even if all Ag were sulfurized. On the contrary, at point 3 where no nanoparticles can be seen, a small amount of Ag was detected but the Co level was below the detection limit, indicating that Ag segregates only when Co is located nearby. Since Ag was observed only at the location where the Ag/Co nanomatches reside in the $Ag_{20}Co_5(TiO_2)_{95}$ film (60 min deposition), it can be assumed that tiny Co metal nanoparticles was first formed and that Ag subsequently crystallized through the aggregation of Ag ions around the Co metal nanoparticles to form the Ag-Co nanomatch structure. It is thought that most of but not all Ag was segregated for 30 min after starting deposition.

A $Ag_{20}Co_5(TiO_2)_{95}$ film (120 min deposition) was also fabricated and the corresponding SEM image together with EDX results observed on the film surface was shown in Figure 3-3-1-7. Large particles containing Ag were observed on the surface. From the cross-sectional TEM image (Figure 3-3-1-8), it is evident that the particles with various sizes went out of the film and moved into the adhesive layer.

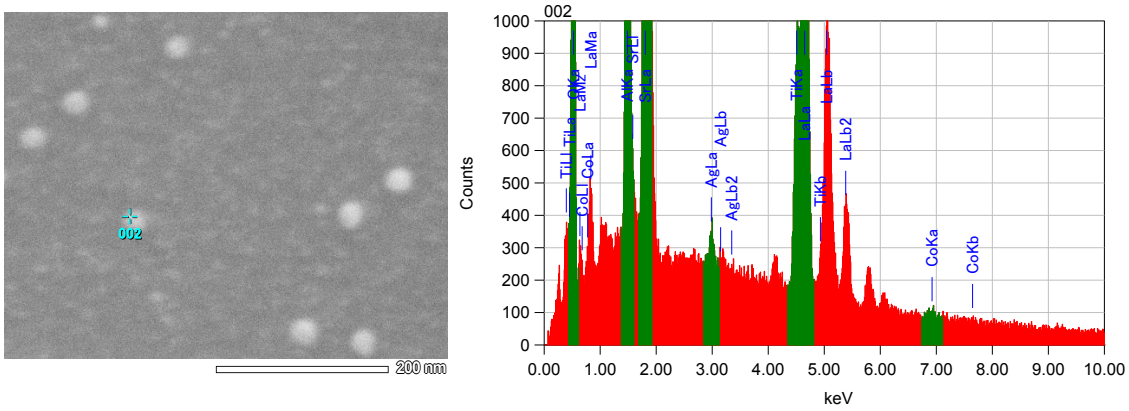

Figure 3-3-1-7 SEM image of $Ag_{20}Co_5(TiO_2)_{95}$ film (120min deposition) with EDX spectrum of point 1 in the left image.

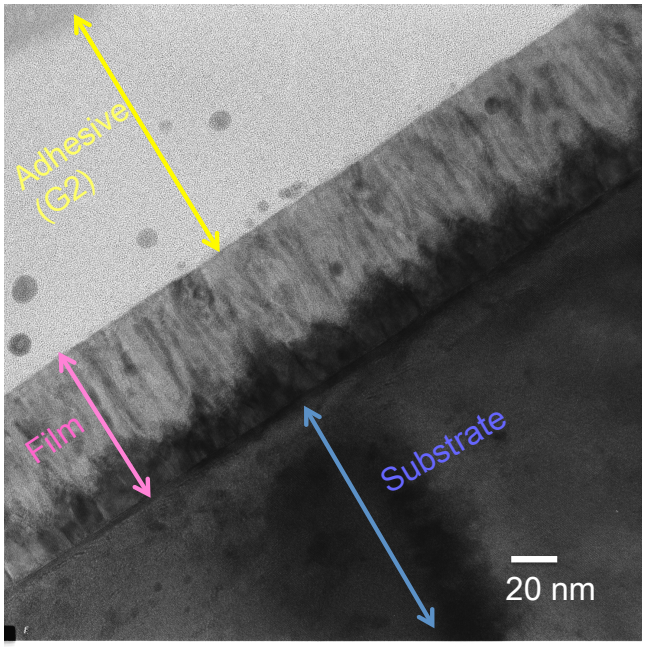

Figure 3-3-1-8 Bright field TEM image of $Ag_{20}Co_5(TiO_2)_{95}$ film (120min deposition). (The TEM used for the measurement was JEOL, JEM-2010HC.)

The TEM/EDX analysis (data not shown) also confirmed that most of Ag was segregated on the film, and that a trace amount of Ag was detected at the locations of black circular particles. This result indicates that too long time deposition does not lead to longer Ag nanorods. Instead, the Ag nanoparticle are combined with each other to form larger Ag particle and are finally ejected out of the TiO_2 crystal. It is very difficult to explain why the nanomatch structure is formed, because the structure is determined by the balance between thermal equilibrium and metal atom (ion) diffusion. Practically, for fabricating the characteristic Ag-Co nanomatch structure, the deposition time should be ~ 60 minutes. In other words, the appropriate thickness of the $Ag_{20}Co_5(TiO_2)_{95}$ film to reproduce the Ag/Co nanomatch structure on the LSAO substrate was ~ 40 nm. From these results, Co is thought to play an important role in the segregation of Ag. To confirm this, Ag-TiO_2 and Co-TiO_2 layers were separately deposited for 60 minutes on the same pure TiO_2 seed layer. Figures 3-3-1-9 (a) and (b) show cross-sectional TEM images observed at the different locations in the exactly same film.

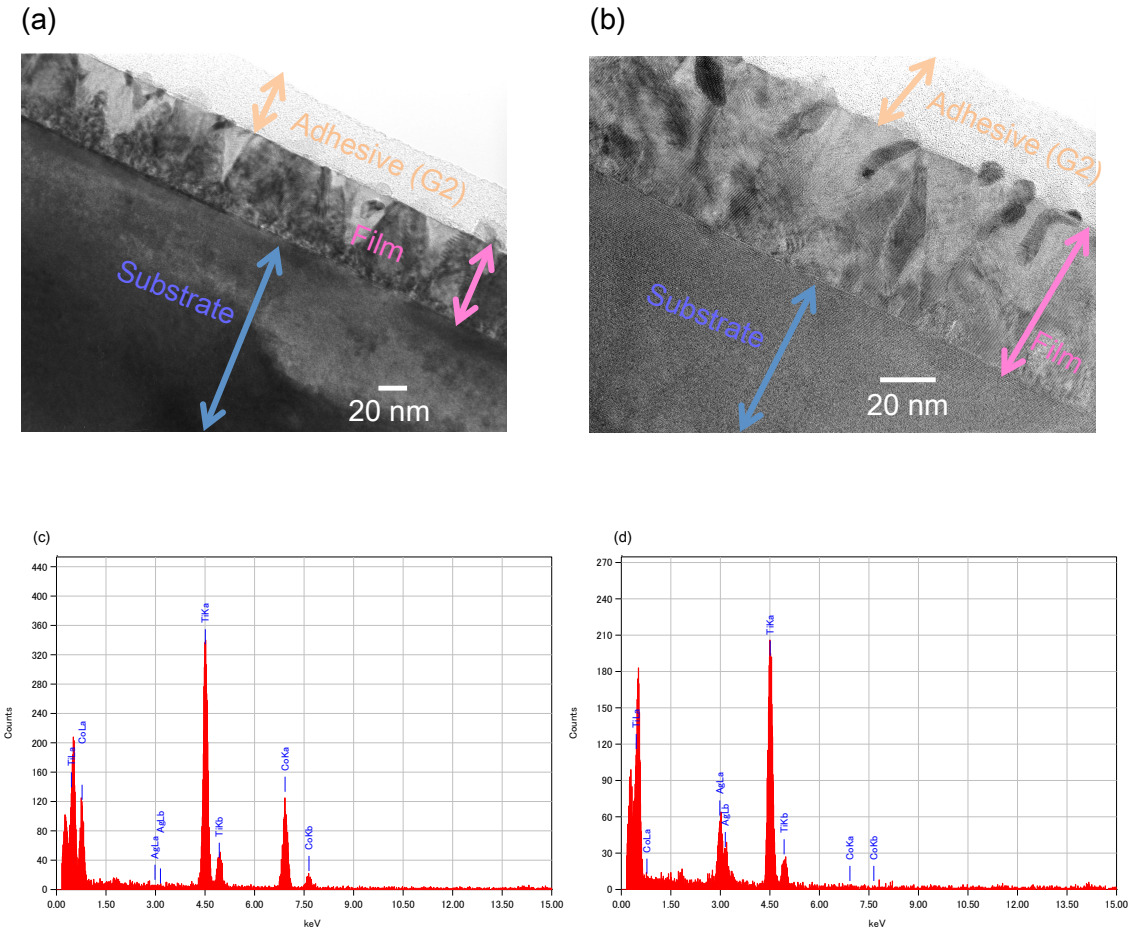

Figure 3-3-1-9 Bright field TEM image of $Ag_{20}(TiO_2)_{95}$ - $Co_{20}(TiO_2)_{95}$ bilayer film on pure TiO_2 seed layer and the EDX spectra of (c) $Co_{20}(TiO_2)_{95}$ layer (the substrate side of the film position in (a)) and (d) $Ag_{20}(TiO_2)_{95}$ layer (the adhesive side of the film position of (a)) (The TEM used for the measurement was JEOL, JEM-2100.)

The both figures exhibit irregular nanostructures: the nanostructures were not aligned at all. Moreover, no rod-like ones can be seen. These suggest that co-deposition of Co and Ag is crucial for the formation of Ag-Co bimetallic nanomatch structure. From EDX measurements, no intermixing of Ag and Co was observed: only Co was detected in the Co-TiO_2 layer, whereas only Ag in the Ag-TiO_2 layer, indicating that the Ag/Co nanostructure was formed simultaneously with the crystallization of TiO_2, and that Ag and Co no longer diffuse after the crystallization of host TiO_2. Furthermore, Ag rich nanostructure of various shapes and sizes, depicted with darker color, were located in the TiO_2 matrix with relatively bad crystallinity, i.e., in the matrix region containing an amorphous-like phase.

In order to investigate LSPR phenomena in the original $Ag_{20}Co_5(TiO_2)_{95}$ films with the Ag/Co nanomatch structure, I conducted UV-Vis spectroscopic measurements, where the incident light was set perpendicular to the rods. In this configuration, the localized surface plasmon mode, not surface plasmon propagation, should be mainly considered, because the Ag nanostructures are very small, ~5 nm in diameter and 10-20 nm in height and the rod interval is 10-20 nm. Since the color of the $Ag_{20}Co_5(TiO_2)_{95}$ films changed as a function of deposition time: transparent pale pink for 60 min deposition and transparent yellow for 120 min deposition, the plasmon resonance peak position was expected to vary depending on the PLD condition. Considering the fact that the color was more vivid in the 120 min-deposition film than the 60 min deposition

one, it was anticipated that the plasmonic signal is enhanced with increasing Ag amount. Thus I also fabricated a heavily Ag doped Ag-Co-TiO_2 films from a sintered target of $Ag_{100}Co_5(TiO_2)_{50}$. The obtained optical spectrum of the $Ag_{100}Co_5(TiO_2)_{50}$ thin film (60 minutes deposition) were shown in Figure 3-3-1-10 together with the spectrum of $Ag_{20}Co_5(TiO_2)_{95}$ (60 min deposition), where UV-Vis light is introduced perpendicular to the film normal.

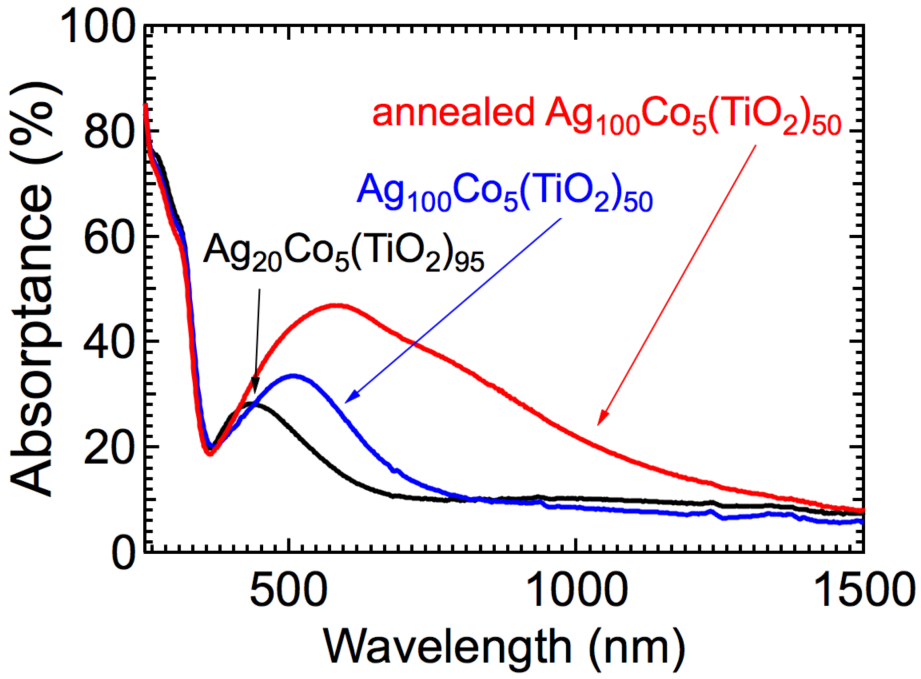

Figure 3-3-1-10 Absorptance spectra of as deposited $Ag_{20}Co_5(TiO_2)_{95}$ (60 minutes deposition), $Ag_{100}Co_5(TiO_2)_{50}$ thin films and the annealed $Ag_{100}Co_5(TiO_2)_{50}$ thin film.

As can be seen from the figure, a LSPR peak was clearly observed around 450 nm in $Ag_{20}Co_5(TiO_2)_{95}$ (60 min deposition) film. The larger absorption peak below 350 nm corresponds to the inter-band transition across the bandgap of TiO_2, 3.2 eV. Note that the oxygen pressure of the $Ag_{20}Co_5(TiO_2)_{95}$ film (60 min deposition) was set to P_{O2} = 1×10^{-7} Torr in this chapter, however, P_{O2} = 1×10^{-6} Torr was much easier to maintain stable than P_{O2} = 1×10^{-7} Torr in our PLD chamber whose background pressure was ~ 1×10^{-8} Torr. I confirmed that the films deposited at P_{O2} = 1×10^{-6} Torr and P_{O2} = 1×10^{-7} Torr showed essentially the same optical properties. Hereafter (in Chapter 4 and 5), I fabricated the films under P_{O2} = 1×10^{-6} Torr.

The $Ag_{100}Co_5(TiO_2)_{50}$ thin film had absorption peak at ~ 500 nm, which is red-shifted by ~50 nm and is slightly enhanced compared with that of $Ag_{20}Co_5(TiO_2)_{95}$ film, as I expected. Here I attempted to further change the Ag nanostructure of the $Ag_{100}Co_5(TiO_2)_{50}$ thin film by annealing under the background pressure ($P_{Chamber}$ = 1×10^{-8} Torr) without supplying O_2 gas at T_S = 450 °C for a hour. The annealed $Ag_{100}Co_5(TiO_2)_{50}$ film showed a much enhanced but broad LSPR peak. The surface morphology of the as-deposited and annealed $Ag_{100}Co_5(TiO_2)_{50}$ films was compared in Figure 3-3-1-11.

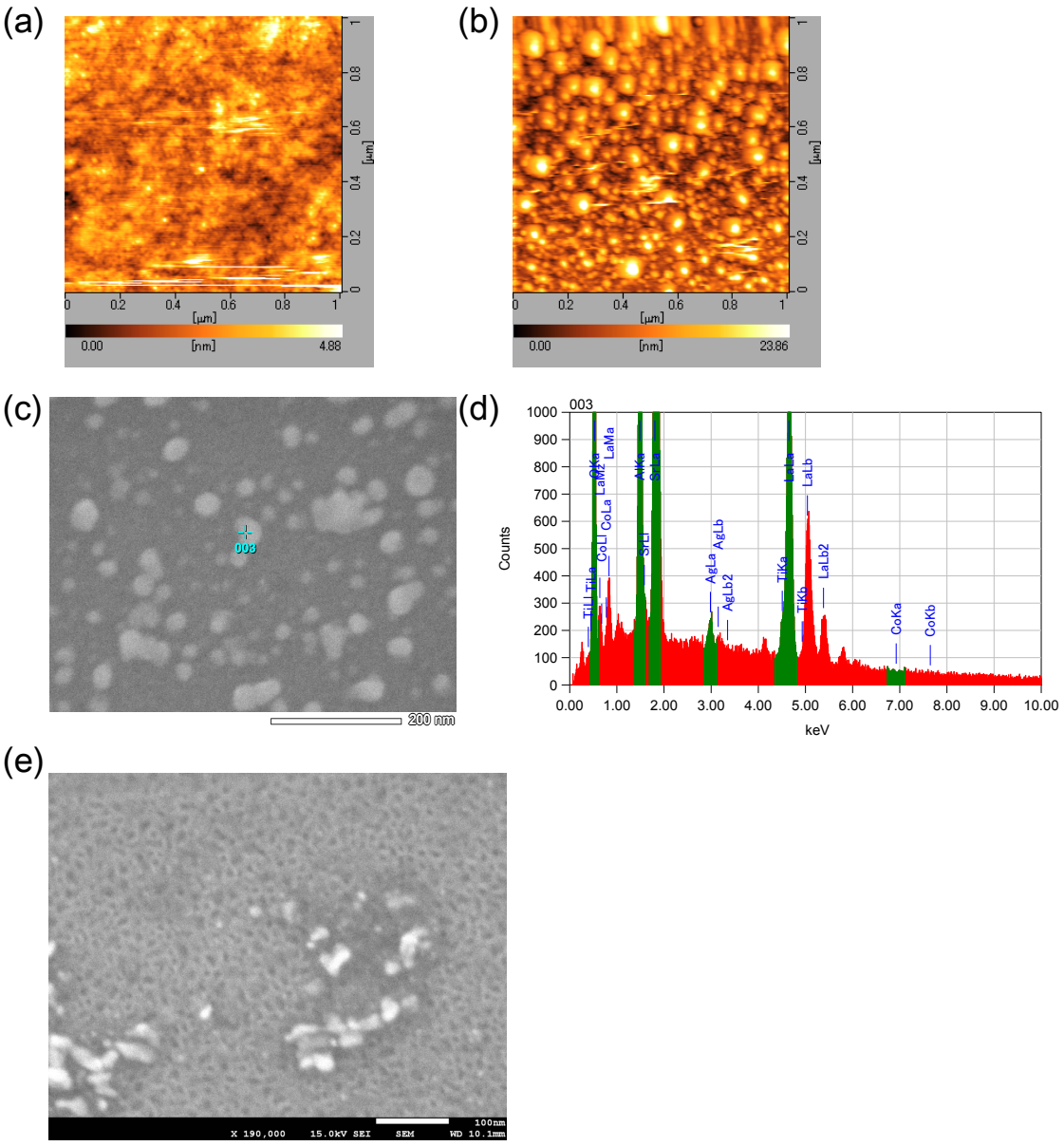

Figure 3-3-1-11 Surface morphologies of (a) the as deposited $Ag_{100}Co_5(TiO_2)_{50}$ thin films and (b) the annealed $Ag_{100}Co_5(TiO_2)_{50}$ thin film measure by AFM image. The (c) SEM image of annealed $Ag_{100}Co_5(TiO_2)_{50}$ thin film with (d) EDX spectrum at the point of nanoparticle (point 3 in (c)). (e) The finer SEM image of the annealed $Ag_{100}Co_5(TiO_2)_{50}$ thin film after cleaned by cotton buds.

The AFM images indicated that the surface became rougher and large particles appeared after the annealing. SEM-EDX analysis revealed that the large particles were composed of Ag, which is attributable to the enhanced and broadened LSPR peak. It should be noted that the blue color of the annealed $Ag_{100}Co_5(TiO_2)_{50}$ film and not annealed $Ag_{200}Co_5(TiO_2)_{50}$ film disappeared when the surface was cleaned by cotton buds with acetone, while the color was unchanged by the cleaning for the $Ag_{100}Co_5(TiO_2)_{50}$ and $Ag_{20}Co_5(TiO_2)_{95}$ films (60 min deposition). In addition, many holes appeared on the surface of annealed $Ag_{100}Co_5(TiO_2)_{50}$ films after the cleaning (Figure 3-3-1-11 (d)). No Ag was observed at the locations of holes, indicating that Ag nanoparticles inside the film were totally ejected out of the film by annealing. It is considered that the ejected Ag existing on the film surface was removed by the cleaning. Annealing is a new technique for collecting Ag easily. In the $Ag_{200}Co_5(TiO_2)_{50}$ film, most Ag was segregated without annealing. However, these fragile Ag nanostructures are not suitable for my goal, which aims at utilizing the stable Ag nanostructures. The properties of embedded Ag-Co nanostructures will be discussed in the next chapter.

Appendix: Ag-Co-TiO_2 Target color

3-3-2. Electromagnetic analyses

Numerical simulation for electromagnetic field is a powerful tool to know how efficiently the electric filed is enhanced and at which locations of the nanostructures the electric field is enhanced. In order to elucidate the origin of the absorption peak of the Ag-Co-TiO_2 films, I performed electromagnetic analysis, using finite difference time domain (FDTD) method, where commercially available software, Lumerical. Co. Ltd was employed. Before taking realistic Ag/Co nanostructures into account, I first calculated the electromagnetic field profiles and the optical spectra using simpler models for the Ag nanostructures in the Ag-Co-TiO2 films. Since the Ag nanorods aligned vertically to the film surface, as described in the previous section (Section 3-3-1, Figure 3-3-1-3), the light was injected parallel to the rod direction in the FDTD simulation. The electromagnetic field enhancement was calculated, assuming that a Co sphere of 10 nm in diameter was placed in a TiO_2 matrix just on a seed layer and a Ag nanorod of 6 nm in diameter and 20 nm in height was located above the Co particle along the film normal. The Ag-Co-TiO_2 composite film and anatase TiO_2 seed layer were assumed to be 35 nm and 5 nm in thickness, respectively. I also assumed periodic alignment of the Ag-Co nanostructure (periodic boundary condition) in the plain-view directions and the presence of a perfectly matched layer (PML), being an absorbing boundary layer, in the cross-sectional direction, i. e., in the direction of incident light propagation. The optical constants of anatase epitaxial film were based on the previous research

[S. Tanemura, 2003].

The electric field profiles with the incident light of 450 nm in wavelength, at which an absorption peak was experimentally observed (Figure 3-3-1-10), was shown in Figure 3-3-2-1.

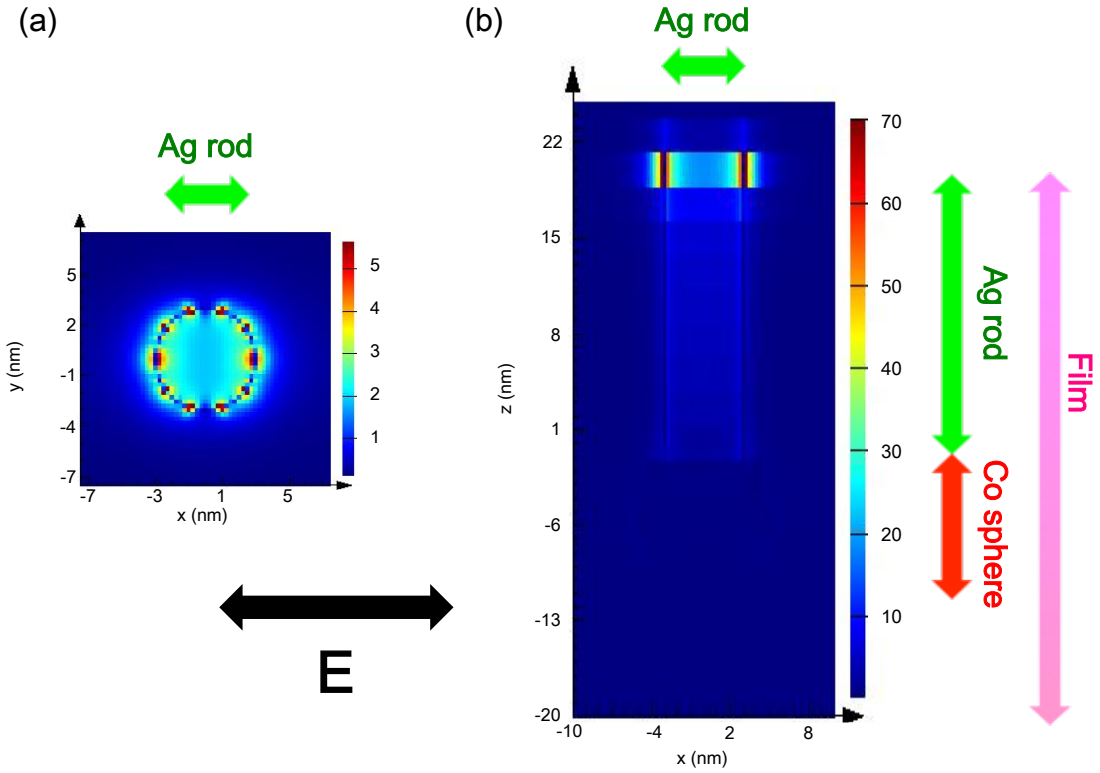

Figure 3-3-2-1 Electromagnetic field enhancement of (a) plain view and (b) cross sectional direction to the film normal. The black arrow indicates the linear polarization of incident light. Pink, green, red arrows depict the position of film, Ag nanorod, Co nanosphere, respectively.

The electromagnetic field distribution in the plain-view direction was enhanced parallel to the incident electromagnetic field, similar to the dipole mode (but

perhaps combined with a higher-order plasmonic mode). While the electric field in the cross-sectional direction was enhanced only along the Ag rod, and no enhancement was seen around the Co sphere; i.e., only Ag nanorods in TiO_2 matrix would induce LSPR without the help of the Co nanospheres. Additionally, the field is enhanced at the interface between Ag nanorod and TiO_2 matrix. Consequently, larger surface area of TiO_2 could gather the light energy. Notably, the electric field enhancement was particularly large at the film surface, indicating that this film would be suitable for the application utilizing the reactions or sensing at the film surface, such as liquid type cells, photocatalytic reactions, and SERS. Since Co was not important for LSPR in this system, the factors that govern the LSPR peak intensity can be extracted through the calculations using a simple Ag spheres without Co. As mentioned in the previous section, the Ag nanoparticles in the Ag-Co-TiO_2 nanocomposite exhibit a clear absorption peak, though they are very small. In case of Au nanoparticles, in contrast, it is assessed that the plasmon resonance peak sharply decreases with the size and almost disappears when the diameter is less than 3 nm [M. C. Daniel, 2004]. Thus it is important to understand which factor enhances LSPR in this Ag-Co-TiO_2 system. Here, the interval, size and depth of Ag spheres in the TiO_2 matrix were investigated as such factors. Simple model assuming Ag nanospheres in an anatase TiO_2 matrix were used as shown in the insets of Figure 3-3-2-2 to 3-3-2-4, where the thickness of the TiO_2 matrix, the angle of incident light, and the boundary condition were same as those in Fig. 3-3-2-1.

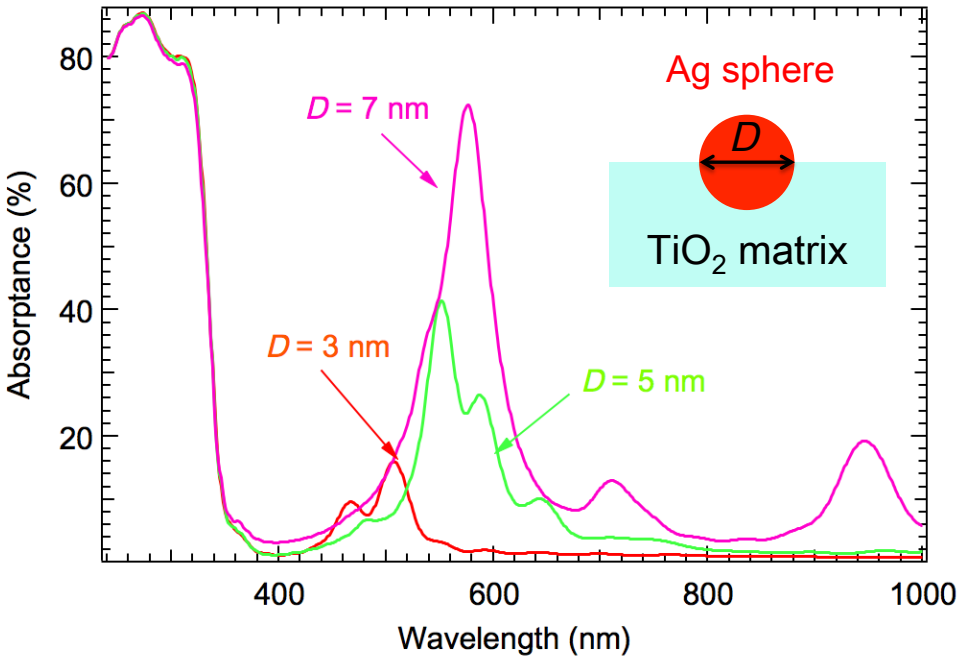

Figure 3-3-2-2 Size dependence of the absorptance spectra of half-embedded Ag spheres, where *D* was the diameter of the Ag spheres.

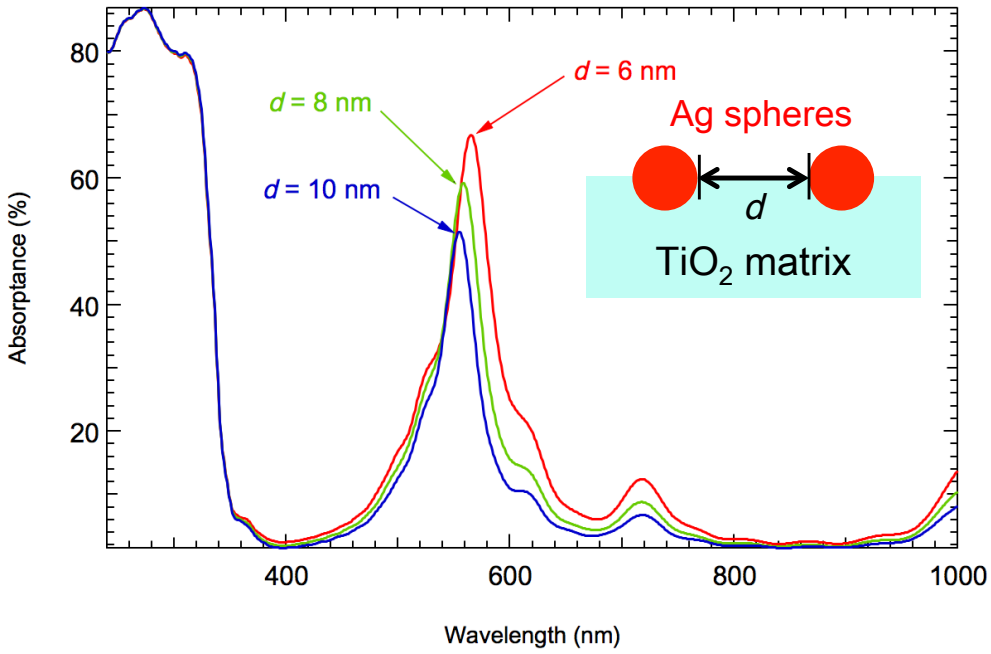

Figure 3-3-2-3 Interval distance dependence of absorptance spectra, of half-embedded Ag spheres, where *d* is the interval between neighboring Ag spheres.

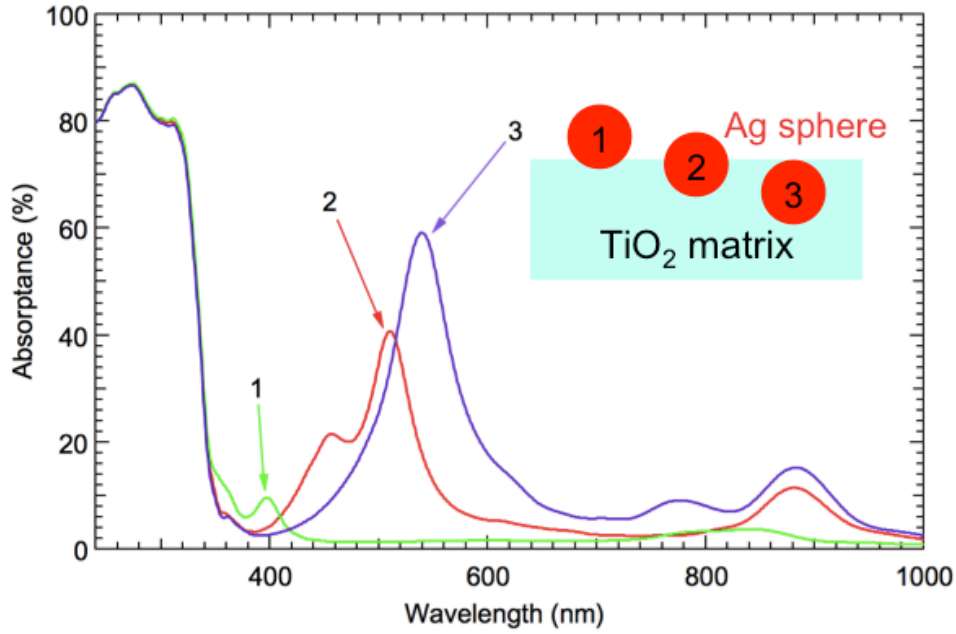

Figure 3-3-2-4 Absorptance spectra of 1: totally segregated, 2: half-embedded, 3: fully embedded Ag spheres.

Figure 3-3-2-2 shows absorptance spectra calculated for half-embedded Ag nanosphere, where the diameter of the nanosphere varied in a range of 3-7 nm. The interval distance between Ag particles were all set to 6 nm. As the diameter increases, the LSPR peak was enhanced and red-shifted and, at the same time, the several components evolved. The spectra became complicated at the larger Ag spheres, which is possibly because the interval between particles is comparable to the diameter of the Ag spheres and plasmon coupling occurs. Figure 3-3-2-3 was the absorptance spectra, where the interval between half-embedded Ag spheres was varied from 6 to 10 nm and the diameters of the

Ag spheres were fixed to 6 nm. Although the interval was as small as the sphere size, the intensity did not change drastically; the LSPR peak was slightly enhanced and red-shifted, as the interval becomes smaller. On the contrary, the effects of surrounding media were clearly seen in Figure 3-3-2-4, where the diameter of Ag spheres and the interval were set to 10 nm and 15 nm, respectively. The peak was very small when the Ag sphere was partially buried in the TiO_2 matrix, even though the size of the Ag sphere was much larger than those of the experimentally observed Ag nanorods. As the Ag spheres are buried deeper into the TiO_2 matrix, the LSPR peak was more enhanced and red-shifted. When focusing on the absorption at ~450 nm, it was enhanced more than several times in case that the sphere was completely buried in the anatase matrix. In conclusion, the surrounding environment is an important factor giving a significant influence on the optical properties of the Ag-Co-TiO_2 composite system.

Finally, in order to confirm the origin of absorption peak in the experimental configuration (Figure 3-3-1-10), the absorptance spectra were calculated using a more complex model. The positions of the diameters of Co nanospheres were obtained as digital data directly from the experimental plain-view TEM image. These data were used in the simulation: nanomatches were simulated as cylinders composed of Ag and Co of which two-dimensional positions and diameters are assumed to be equal to the above-mentioned values. I did not use the EDX map of Ag for the simulation, because the tilting of Ag nanorods was

not negligible and each nanorods was imaged as a large oval. The heights of Ag and Co nanorod parts were set to 20 nm and 5 nm, respectively, as illustrated in Figure 3-3-2-5.

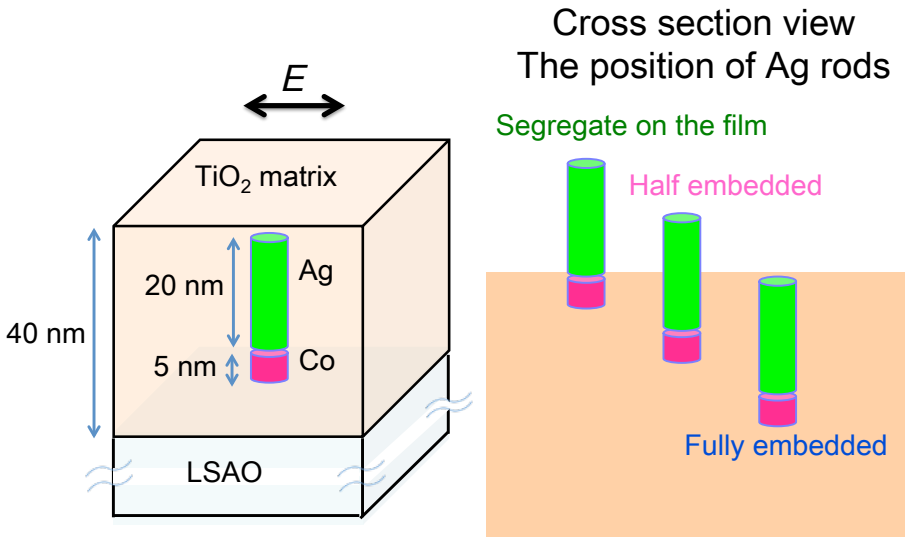

Figure 3-3-2-5 Schematic image of the Ag/Co structure, where Ag column was on the Co column.

The thicknesses of the TiO_2 film and $LaSrAlO_4$ (LSAO) substrate was set to 40 nm and 1 μm, respectively. The optical constants of the LSAO substrate were calculated from experimental transmittance and refractive index spectra, based on the mathematical methods reported previously [M. Kobiyama, 2003]. The surrounding environment is an important factor that determines the optical properties of this system, as described above. Hence, in the simulation, I assumed three cases for the depth of Ag rods in the TiO_2 matrix: fully embedded

in the matrix, half embedded in the matrix, and totally segregated on the TiO_2 surface, as illustrated in Figure 3-3-2-5. The absorptance spectra assuming fully embedded and half embedded Ag-Co nanorods well reproduced the experimental one: the simulated wavelength range, over-all spectral shape and peak intensity were in good agreement with experimental ones (Figure 3-3-2-6).

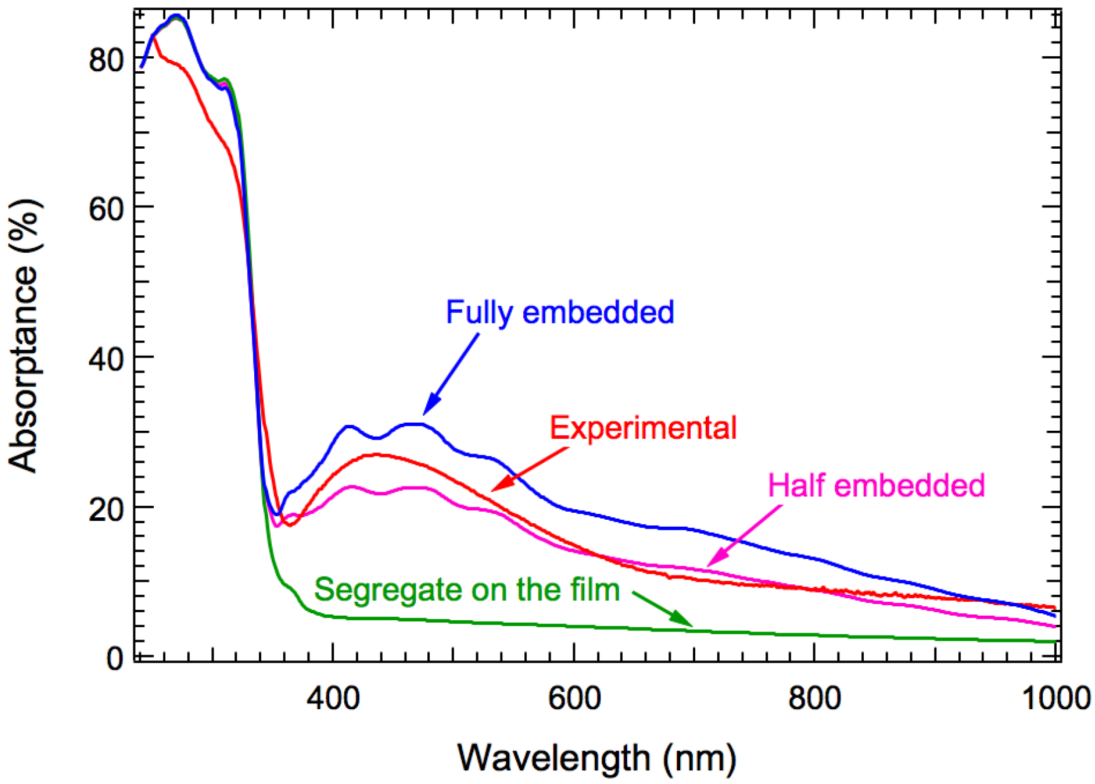

Figure 3-3-2-6 Absorptance spectra of Ag-Co rods, fully embedded, half embedded in, and totally segregated on TiO_2 matrix.

The calculation confirmed that the peak observed in the experimental spectra was due to LSPR absorption associated with the Ag/Co rods structure. The calculated spectra showed several fine structures near the absorption maxima, while the experimental one did not; the fine peaks in the calculated spectrum correspond to each different plasmon modes. Notably, the experimental spectrum was substantially smeared out compared with the calculated one. This is possibly due to the merging of several plasmon resonance modes or to the averaging of the absorptance spectra over a larger area (This simulation used a TEM image of only less than 1 μm^2 in area indicated with a white square in Figure 3-3-2-7 (a), while experimental measurements were done over a larger area of several mm^2.) The tilting of Ag-Co nanorods may contribute to the smearing, as well. Amazingly, when all Ag/Co nanorods were segregated on the film surface, no absorption peak was seen around 450 nm. This is because the Ag nanorods with several nm in diameter are too small. It was noteworthy that the peak intensity of experimental spectrum around 400-600 nm was larger than the simulated one assuming half embedded nanorods, while it is smaller than that assuming fully embedded nanorods. Experimentally, it was observed that most of the Ag nanorods were embedded in the matrix, but some are sticking out of the surface and their embedded parts were shorter than 20 nm in length. These facts well explain well why the experimental spectrum shows an intermediate feature between half embedded and full embedded case. Electric field enhancement in the plain view directions is shown in Figure 3-3-2-7.

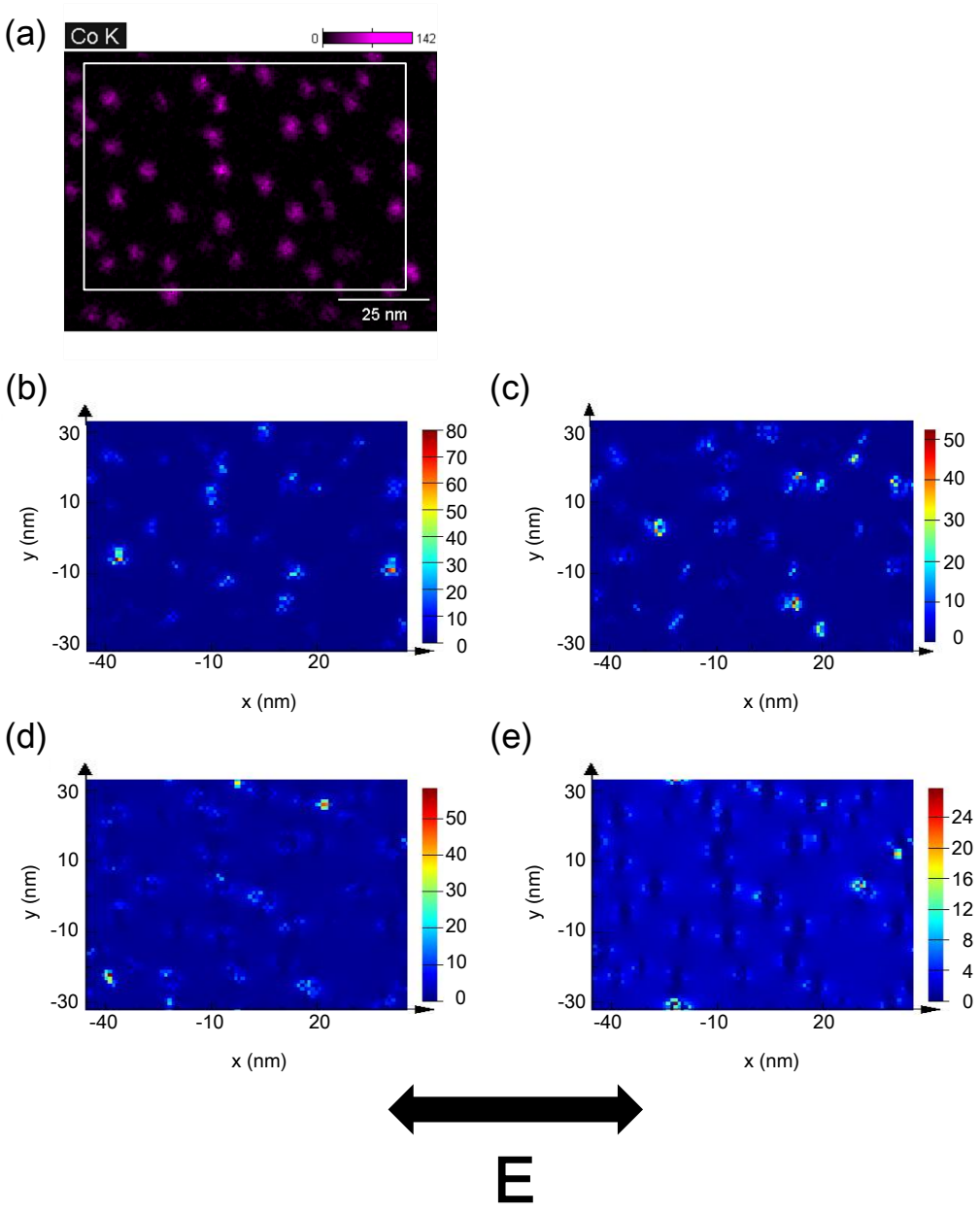

Figure 3-3-2-7 (a) Imported Co plain view STEM-EDX image of $Ag_{20}Co_5(TiO_2)_{95}$ film (K. Ikemiya, Dr. thesis 2011, p.38), as two dimensional position and the size of both Ag and Co nanorods. The white part was used in the simulation. The black arrow indicates the linear polarization of incident light. (b-e) Electric field enhancement of Ag-Co rods in plain view direction, when the incident light was (b) 450 nm, (c) 500 nm, (d) 800 nm, (e) 1000 nm, in wavelength.

Each Ag nanorod enhanced the electric field, especially around the peak wavelength, 450 nm. As the wavelength of the incident light becomes larger than 450 nm, the electric field enhancement at each Ag nanorod had a tendency to become smaller. However even in Figure 3-3-2-7 (d) and (e), small electric field enhancement was obtained. The experimental absorptance spectrum in Figure 3-3-1-10 seemed to have ~7% background noise at λ ~1000 nm, while the calculated spectra in Figure 3-3-2-6 indicated that small absorption should exist at λ ~1000 nm; the result indicates that small absorption in experimental spectrum at long wavelength region was originated from LSPR.

3-4. Summary

In summary, I fabricated Ag and Co co-doped TiO_2 films in various PLD conditions (deposition time, annealing, composition etc.) and established the way of fabricating Ag/Co nanostructures. As a consequence, I could reproducibly fabricate the characteristic nanomatch structures consisting of Ag nanorods on Co nanospeheres embedded in anatase TiO_2 matrix. The importance of Co in the formation of the Ag-Co nanomatch structure and the possibility of the LSPR peak tuning by the fabrication condition were also presented.

The numerical electromagetic simulation (FDTD calculations) based on Ag/Co nanomatch models well reproduced the experimental absorption spectrum. The clear absorption peak at ~450 nm was confirmed to be caused by LSPR induced by the Ag nanorods and it was also clarified that the depth of the Ag nanorods embedded in the TiO_2 matrix was a critical parameter that governed the plasmonic properties of the Ag-Co-TiO_2 nanocomposite.

Chapter 4: The structural variation of Ag-Co-TiO_2 film

The contents of Chapter 4 were already published in

("Structural Variation in Ag-Co Nanostructures Embedded in TiO_2 Thin Films Fabricated by Pulsed Laser Deposition", Anri Watanabe, Katsura Ikemiya, Akira Chikamatsu, Yasushi Hirose, and Tetsuya Hasegawa, *Chem. Lett.*, vol.43, pp. 225-227, 2014. 2.).

4-1. Introduction

Nano composite materials made of dielectric matrix and the metal nanoparticles are paid much attention these days. These functional structures exhibit optical, electronic, catalytic and magnetic properties, which are expected to be used in various applications, as mentioned in Section 1-5. For instance, Ag/alumina nanocomposites has been studied for use of catalysis [X. She, 2004], floating-gate memory devices [Q. Wang, 2004], and polarizer [R. L. Zong, 2004]. Artificial nanocomposite structures have been obtained by various methods, such as ion irradiation [P. Kluth, 2006][K. Awazu, 2009], sol–gel processing [D. Buso, 2009], sputtering [H. Inouye, 1998], and so on. Among them pulsed laser deposition (PLD) well known for thin film deposition technique, has been recognized a potential for fabricating metal nano composite films. For example, metal-alumina nanocomposite films containing Ag nanolentils, nanocolumns, and nanospheres [J. Margueritat, 2006][J. Margueritat, 2007][A. Castelo, 2012] or Cu nanocrystals [R. Serna, 1999] embedded in an amorphous Al_2O_3 have been synthesized by PLD.

Nanocomposite thin films of Co nanostructures and a TiO_2 matrix have also been the subject of intensive studies; the fabrication of Co nanorods in a single-crystal anatase TiO_2 matrix [K. Ikemiya, 2011] and crystallographically oriented Co nanocrystals in a polycrystalline rutile TiO_2 matrix [T. Li, 2013], where the Co nanostructures were self-assembled using phase separation during the PLD growth at high temperature. Recently, it was reported that characteristic Ag/Co “nanomatch” structures, in which Ag nano-rods grow on Co nano-spheres, can be embedded in anatase TiO_2 films by laser ablation of $Ag_2O/CoO/TiO_2$ mixuture sintered target. The obtained Ag/Co-TiO_2 composite films exhibited an absorption peak around 450 nm in wavelength [K. Ikemiya, 2014], which was confirmed to be due to localized surface plasmon resonance (LSPR) as described in Section 3-3-2. One possible application of the Ag-Co-TiO_2 thin films is a plasmonic device, such as bio-sensing, plasmonic waveguide, and photo voltaic devices, where the device properties were sensitive to size, shape, and distribution of nanostructures. Thus it is practically important to control the size and density of the Ag/Co nanostructures during the film growth.

In Section 3-3-1, the surface morphology including Ag nanoparticles segregated on the surface was roughly controlled by the PLD conditions (nominal target composition and annealing). It was assumed that the shape or size of the Ag/Co nanostructures would be significantly affected by the film growth conditions. In Section 3-3-1 most Ag segregated on the films in

$Ag_{200}Co_5(TiO_2)_{50}$ films and annealed $Ag_{100}Co_5(TiO_2)_{50}$ films because of too much Ag content, thus in this chapter I decided to vary the Ag composition of targets in relatively smaller range. It was also indicated by the FDTD calculation (Section 3-3-2) that the LSPR optical properties in this Ag-Co-TiO_2 film strongly affected by the size of the Ag nanostructure and how deep the nanostructure was embedded in the TiO_2 matrix.

In this chapter, I investigated structural variation of Ag/Co nanostructures as a function of the Ag contents in targets ($Ag_xCo_5(TiO_2)_{95}$), and the substrate temperature (T_S) during the film fabrication. I observed that the shape and distribution of the Ag/Co nanostructures change significantly with T_S and the target composition. Especially, with increasing Ag content, the shape of the Ag nanostructures changed from rod-like to spherical, leading to the red shift of the Ag LSPR peak. Furthermore, we discussed the mechanism of formation of the Ag/Co nanomatch structures.

4-2. Experiments

Ag/Co co-doped TiO_2 films, $Ag_xCo_5(TiO_2)_{95}$ (x = 20, 40, 60, and 80) in the nominal composition, were fabricated on $LaSrAlO_4$ (LSAO) (001) substrates by PLD method. A KrF excimer laser (wavelength of 248 nm) with frequency of 2 Hz and energy of 18 mJ/pulse was used for ablation. Sintered pellets of pure TiO_2 and $Ag_xCo_5(TiO_2)_{95}$ (molar ratio of Ag:Co:TiO_2 = *x*:5:95) were used as PLD targets for seed layers and $Ag_xCo_5(TiO_2)_{95}$ films (in nominal composition), respectively. The $Ag_xCo_5(TiO_2)_{95}$ pellet was a single mixture target, composed of Ag_2O, CoO, and TiO_2. A pure anatase TiO_2 seed layer was first deposited on LSAO substrates at a substrate temperature (T_S) of 650°C and oxygen pressure (P_{O2}) of 5×10^{-3} Torr. Then a $Ag_xCo_5(TiO_2)_{95}$ thin film was deposited on the seed layers at T_S = 250-350°C and $P_{O2} = 1 \times 10^{-6}$ Torr. The depositions of thin film and the substrate annealing were performed simultaneously. As comparison experiments, $Ag_{20}(TiO_2)_{95}$ films without Co, and $Co_5(TiO_2)_{95}$ films without Ag, were also fabricated on the same seed layer, at T_S = 300°C and $P_{O2} = 1 \times 10^{-6}$ Torr. Including the ~5 nm-thick seed layer, the typical thickness of the obtained films was ~40 nm.

The crystal structures of the films were characterized by X-ray diffraction (XRD). Their absorption spectra were measured by an ultraviolet-visible spectrometer, where the incident light was irradiated in the direction perpendicular to the film normal. The size and distribution of Ag/Co nano-structures were observed with bright field transmission electron

microscopy (JEOL, JEM-2010HC, JEM-2010F), bright field scanning transmission electron microscopy (JEOL, JEM-2100F) and high-angle annular dark field scanning transmission electron microcopy (TOPCON, EM002BF (ASD-2B2)) and (JEOL, JEM-ARM, JEM-2100FHC) with the aid of energy dispersive X-ray analysis (EDX). High resolution TEM image was also obtained for $Co_5(TiO_2)_{95}$ films (Hitachi, H9000NAR).

4-3. Results and discussion

The crystal structures of the Ag films were evaluated by the two dimensional X-ray diffraction measurements. The θ-2θ XRD patterns of $Ag_xCo_5(TiO_2)_{95}$ (x = 20, 40, 60, and 80) thin films (in nominal composition) grown at T_S = 300°C are shown in Figure 4-1.

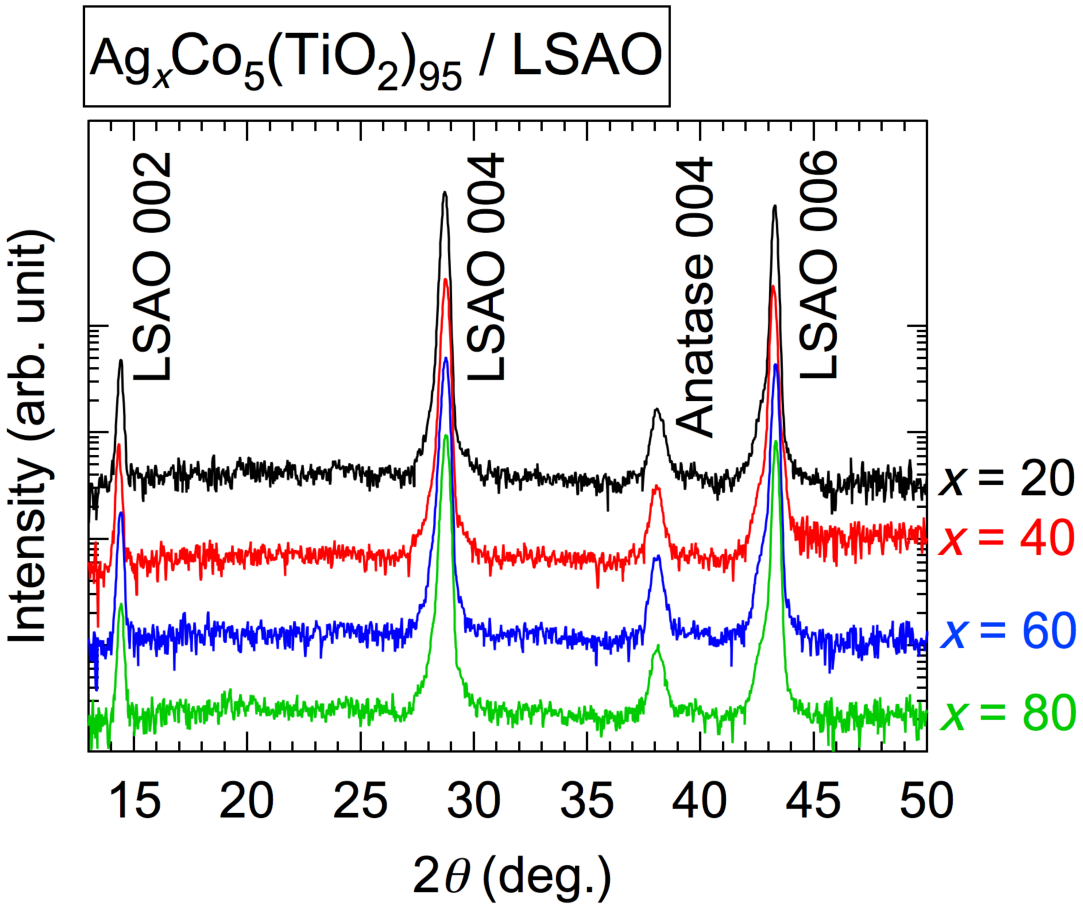

Figure 4-1. XRD patterns of $Ag_xCo_5(TiO_2)_{95}$ (x = 20, 40, 60, and 80) films. (Reprinted with permission from Copyright (2014) The Chemical Society of Japan, A. Watanabe *et al*, *Chem. Lett.*, vol.43, pp. 225-227, 2014. 2.)

In all XRD patterns, the clear peak was observed at 2θ = 38°, corresponding

to the 004 plane of anatase. Each anatase peak of *x* = 20, 40, 60, and 80 film appeared as a single spot in the 2θ - χ image measured by a two-dimensional detector, indicating that the anatase TiO_2 crystal was the epitaxial single crystal (Data not shown). The other peaks were identified to the LSAO 0 0 2n diffractions and no peaks of secondary phases, such as Ag or Co were detected. Ag and Co were assumed to be in nanoparticle form. The cross sectional bright field TEM images of *x* = 20 - 80 film were shown in Figure 4-2.

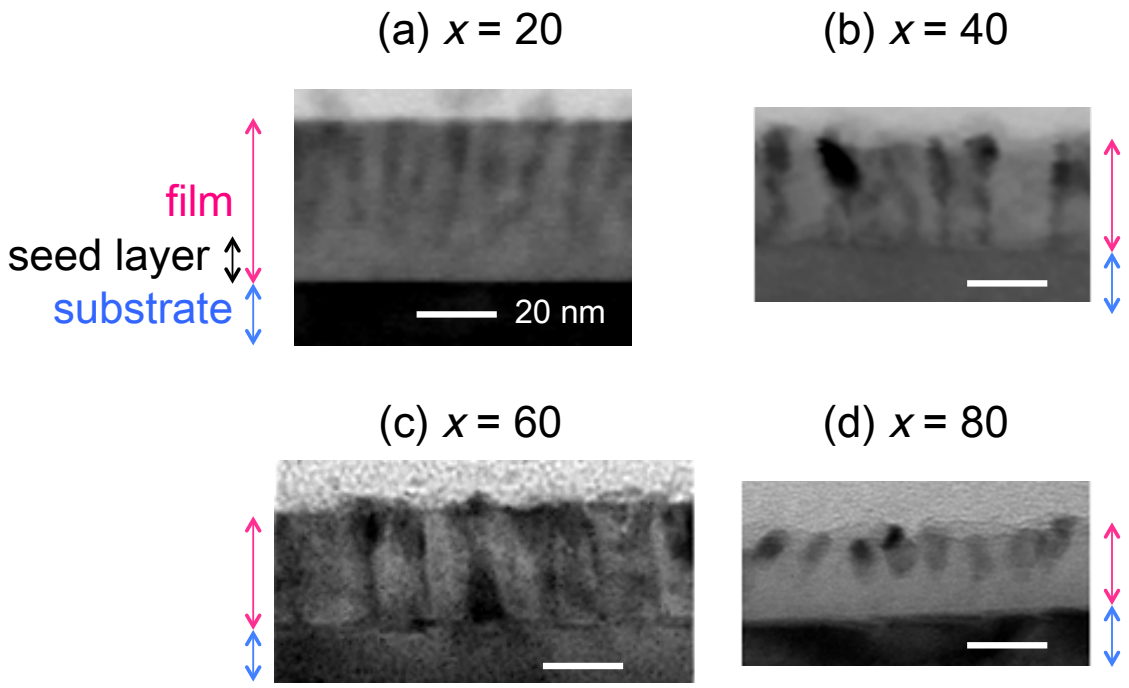

Figure 4-2 Cross sectional TEM images (bright field) of $Ag_xCo_5(TiO_2)_{95}$ films grown at 300 °C. Ag content, *x,* is (a) 20, (b) 40, (c) 60, and (d) 80. Red, blue, and black arrows beside the images indicate the regions of the film, the substrate, and seed layer, respectively. The scale bar is 20 nm.

As the Ag is larger in atomic number than Ti and O, Ag should be depicted in

darker contrast in bright field images. All of Figure 4-2 (a)–(d) seemed to have dark contrast, which correspond to nanostructures. The rod-like shape and spherical shape were obtained in x = 20 film, and x = 80 film, respectively. However, in the x = 40 film and x = 60 film, the shape of nanostructure was not clear only from the contrast of TEM images, and it was difficult to distinguish between rod shape and spherical shape. The high resolution TEM image of x = 40 film (Figure 4-3 (a)) implied the orientation of TiO_2 crystal were not completely uniform, and it was difficult to recognize the Ag nanostructure.

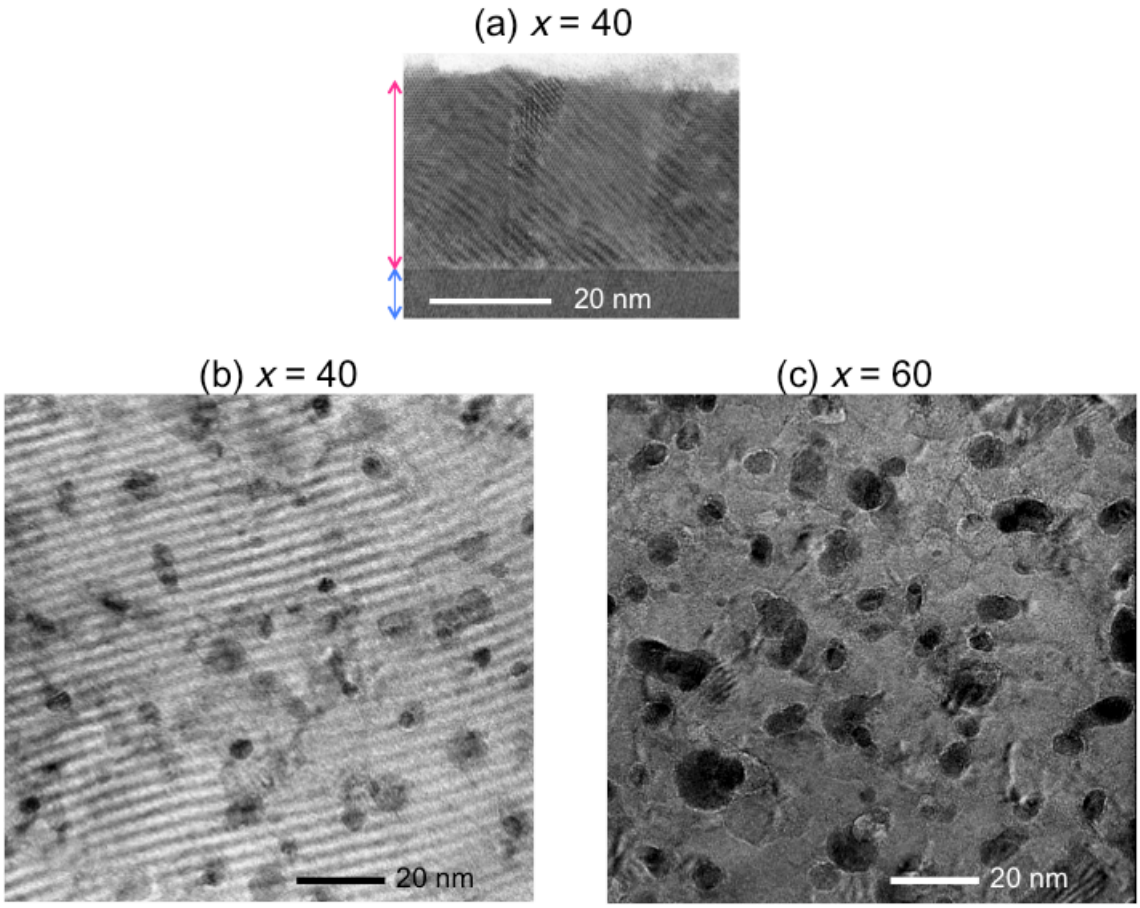

Figure 4-3 Bright field TEM images of $Ag_xCo_5(TiO_2)_{95}$ films grown at 300 °C. (a) High resolution cross sectional TEM image of x = 40. Red and blue arrows beside the images indicate the regions of the film and the substrate, respectively. The plain view TEM images of (b) x = 40, (c) x = 60. The scale bar is 20 nm.

The TEM sample was thick and the Ag parts and TiO_2 parts were overlapped in the TEM image. Thus clear Ag lattice image was not obtained. In the plain view bright field TEM images of x = 40 and 60 films (Figure 4-3 (b), (c)), nanostructures with circular to oval shapes were observed; the shapes were not uniform in both images, but the size of the nanostructure was larger in the x = 60 film than in x = 40.

Since it was difficult to determine the Ag/Co nanostructures by TEM images, the cross sectional STEM-EDX mapping images were obtained on the $Ag_xCo_5(TiO_2)_{95}$ (x = 20, 40, 60, and 80) thin films grown at T_S = 300°C. As shown in Figure 4-4, the x = 20 film exhibited the characteristic Ag/Co nanostructure, in which Ag nanorods are on the Co nanospheres [K. Ikemiya, 2014].

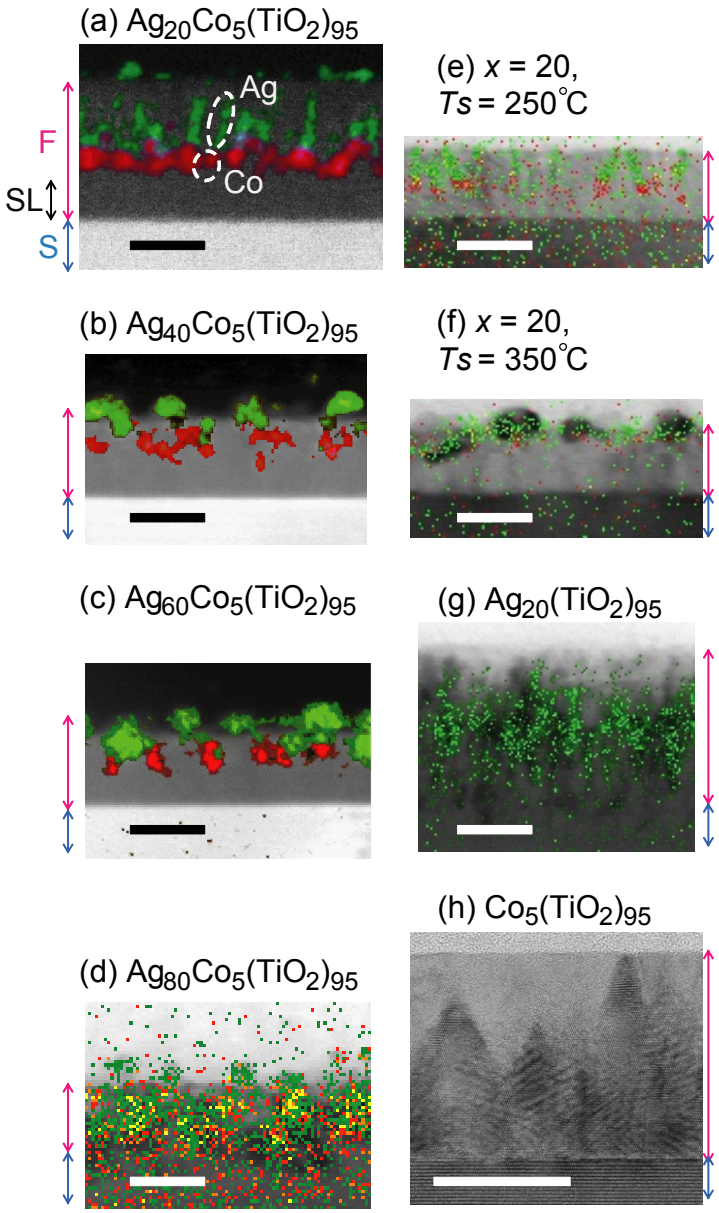

Figure 4-4 (a)-(d): Cross-sectional STEM-EDX mapping images of $Ag_xCo_5(TiO_2)_{95}$ films grown at 300 °C. Ag content, *x,* is (a) 20, (b) 40, (c) 60, and (d) 80. (e), (f): Cross-sectional STEM-EDX mapping images of $Ag_{20}Co_5(TiO_2)_{95}$ films fabricated at substrate temperatures of (e) 250 °C and (f) 350 °C. (g): Cross-sectional STEM-EDX mapping image of $Ag_{20}(TiO_2)_{95}$ grown at 300 °C. Distribution of Ag and Co inside the sample are depicted as red and green, respectively overlapped on high-angle annular dark-field image ((a)-(c)) or bright-field image ((d)-(g)). (h): High resolution cross-sectional TEM image of $Co_5(TiO_2)_{95}$ grown at 300 °C. Red, blue, and black arrows beside the images indicate the regions of the film (F), the substrate (S), and seed layer (SL),

respectively. The scale bar is 25 nm. (Reprinted with permission from Copyright (2014) The Chemical Society of Japan, A. Watanabe *et al*, *Chem. Lett.*, vol.43, pp. 225-227, 2014. 2.)

The Ag nanostructures were fully embedded in the TiO_2 matrix, although there were some Ag segregation on the surface. As the Ag content *x* increased, the shape of Ag nanostructure changed from rods to spheres (Figure 4-4 (a), (b)). In addition, the Ag nanoparticles were half embedded in *x* = 40 film, adjacent to the Co nanoparticles. Comparing the films of *x* = 40 and 60, the size of the Ag nanospheres of the *x* = 60 films were larger than those of *x* = 40 films (Figure 4-4 (b), (c)). Since the special resolution of STEM-EDX images were limited, it was difficult to conclude whether the Ag particle of *x* = 60 films was single large particle or the aggregation of small Ag particles. However, I infer the formation of large Ag particle due to the red shift of the LSPR peak. Even in *x* = 60 films, the Ag particles tended to be located on the Co nanoparticles. In the films with *x* = 80 (Figure 4-4 (d)), the Ag nanoparticles became larger and the Ag particles were spread all over the film irregularly and the number of the Ag nanoparticles increased. Some were totally and others were partially embedded in the anatase matrix. Even in the films with larger *x* value films, such as *x* = 100, the appearance of the Ag nanoparticles were almost same but the number and the density of Ag particles increased (data not shown). Interestingly, in the films with large Ag content near to the percolation limit (*x* = 80, 100), extra Ag was ejected from the film surface. From these results, it can be concluded that the

characteristic Ag/Co nanostructure was formed in very narrow Ag content range at around x = 20.

Next I focused on the substrate temperature, T_S, dependence during the film fabrication. It was thought that the annealing temperature would affect the crystallization of films and thus gives a large influence on the diffusion or movement of the metal atoms during the crystallization. I fabricated x = 20 films with different T_S at the range of 250-350 °C. XRD measurements confirmed that epitaxial anatase crystals were also formed in both T_S = 250 °C and 350 °C films (data not shown). The cross-sectional STEM-EDX images were shown in Figure 4-4 (e), (f). In the film grown at T_S = 250 °C, the Ag nanorods were entirely embedded in the anatase matrix and the Co nanospheres resided beneath Ag nanorods. On the other hand, in the film grown at T_S = 350 °C, the characteristic Ag/Co nano structure no longer evolved. Ag nano particles with irregular size and shape distributed at the film surface. This result suggested that the Ag segregation was due to the enhanced thermal diffusion. Thus the Ag-Co nanomatch structure were formed at the narrow T_S range of 250-300°C.

Here I discuss about the formation mechanism of this characteristic Ag-Co nanomatch structure of the x = 20, T_S = 250-300 °C films. As the Co nanospheres were always beneath the Ag nanorods, it seemed that the Co nanospheres played an important role of Ag nanorod growth. In order to elucidate the concrete function of Co nanospheres, I fabricated Ag doped TiO_2 films without Co, i.e. $Ag_{20}(TiO_2)_{95}$ films at T_S = 300 °C. The cross section

STEM-EDX mapping of the film was shown in Figure 4-4 (g). No Ag nanorods were formed in the $Ag_{20}(TiO_2)_{95}$ films, instead, the various sizes and shapes of Ag nanoparticles were randomly spread in the film matrix. High resolution TEM measurements of a Co doped TiO_2 film without Ag were conducted and I found that the epitaxially grown TiO_2 crystals have triangular shapes, as shown in Figure 4-4 (h). Moreover, from HAADF-STEM observations (Figure 4-5 (a)) it was found that each Co nanoparticle (depicted with brighter color due to z contrast, which was confirmed in the EDX measurements) resides at the bottom of each valley, as schematically illustrated in Figure 4-5 (b).

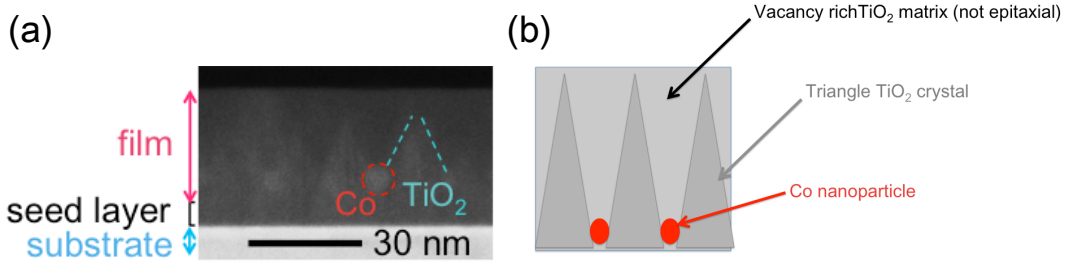

Figure 4-5 (a) Cross-sectional HAADF-STEM image and (b) its schematic images of $Co_5(TiO_2)_{95}$ films grown at 300 °C.

Based on these observations, I proposed the following formation mechanism. Once tiny Co nanoparticles are formed in the $Ag_{20}Co_5(TiO_2)_{95}$ film/TiO_2 seed film interface in the initial stage of PLD film fabrication. The Co nanoparticles were thought to behave as obstacles to the crystal growth of epitaxial anatase TiO_2

crystal. As a result, the TiO_2 matrix above the Co nanoparticles contains defects, such as oxygen vacancies. In the defect-rich TiO_2 matrix, it was reasonable to assume that the diffusion of Ag or Co atoms was accelerated and that Ag and Co are segregated on the Co nanoparticles located at the bottom of valleys. Further motion of Ag and Co towards the film surface side and substrate side, respectively, resulted in the formation of the characteristic nanomatch structure. Since the Co is immiscible with Ag [A. E. Tselev, 1999][H. Sang, 1995][S. Pisov, 2008], the Ag and Co diffused long distance towards the Ag and Co, respectively. This was why the Co nanoparticles behaved as the nucleation center of the Ag nanorods. The role of Co in a Ag-Co-TiO_2 film is to determine the two dimensional position, that is plain view direction, of Ag/Co nanomatch structure, and to make the space for a Ag nanorod to grow between the TiO_2 crystal. However, the Ag segregation, at the various positions in the film matrix, took place when the Ag content increased.

Finally I discuss the optical properties of the films grown at T_S = 300 °C with different Ag content. Figure 4-6 are the absorptance spectra of the $Ag_xCo_5(TiO_2)_{95}$ films (x = 20, 40, 60, and 80).

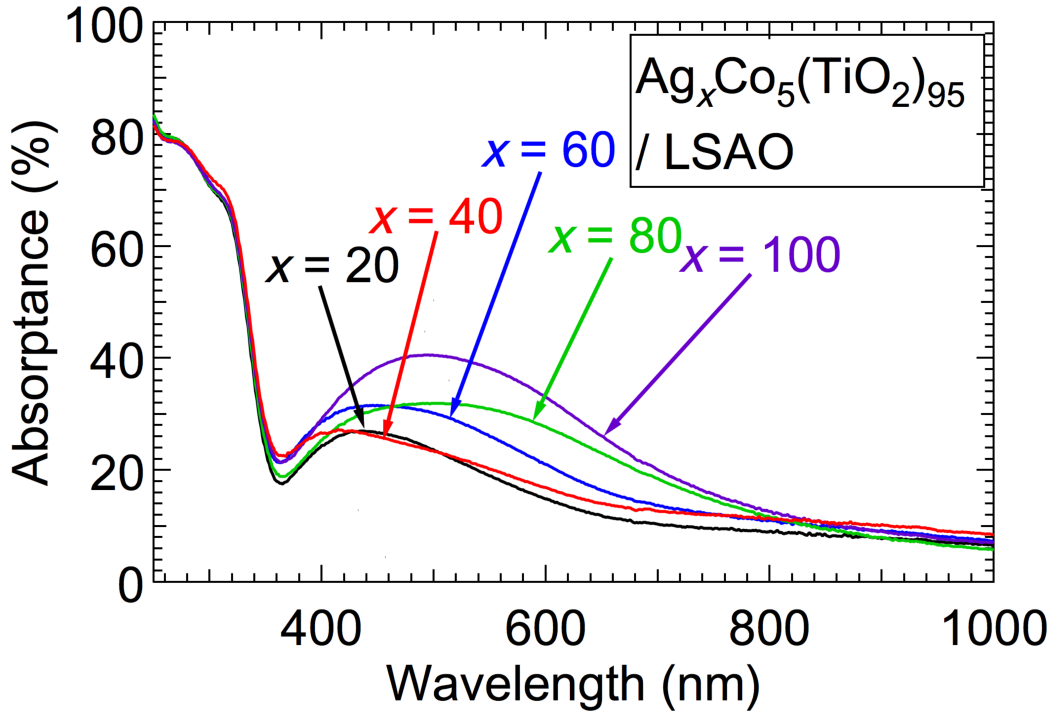

Figure 4-6. Absorptance spectra of $Ag_xCo_5(TiO_2)_{95}$ films fabricated at 300°C. (Reprinted with permission from Copyright (2014) The Chemical Society of Japan, A. Watanabe *et al*, *Chem. Lett.*, vol.43, pp. 225-227, 2014. 2.)

The intense absorption peak below 390 nm was due to the TiO_2 interband transition of TiO_2 bandgap (3.2 eV). Each spectrum shows a broad absorption peak at the visible region, resembling to the previous report [K. Ikemiya, 2014]. I confirmed that the absorption peak was due to LSPR by the FDTD calculation, as described in the previous section (Section 3-3-2). As the Ag content increased, the intensity of LSPR peak were enhanced, reflecting the increased density of Ag particles absorbing the light. It was noteworthy that the position of the LSPR peak, hereafter called λ_{peak}, was clearly shifted toward longer wavelength, as *x* increased. It was because the Ag particle size increased [C. L.

Haynes, 2001].

Although the intensity and λ_{peak} were almost systematically varied with the increase of *x*, the LSPR peak of *x* = 20 and *x* = 40 films were similar in both intensity and the λ_{peak}. This similarity can be explained by the FDTD calculation, as already discussed in Section 3-3-2; both the size and the refractive index of the surrounding material were critical in the enhancement and λ_{peak}. As the size of Ag particles increased, or the Ag particles was more embedded in the TiO_2 matrix, the λ_{peak} shifted toward longer wavelength and the peak intensity was enhanced. According to Figure 4-4 (a), (b), the Ag nanorods were entirely embedded in the *x* = 20 films, while the larger Ag particles (compared with Ag nanorods in *x* = 20 films) partially embedded in the *x* = 40 films. The increase of size and the less surrounding dielectric matrix had the opposite effect, leading to the similarity in the LSPR peaks of *x* = 20 and 40 films.

4-4. Summary

I investigated the structural variation of the Ag/Co nanostructures in Ag and Co co-doped TiO_2 films by changing the PLD conditions. It was found that the size, shape, and distribution of Ag-Co nanostructures significantly varied with Ag content, x, and the substrate temperature, T_S, during the thin film fabrication. The characteristic Ag/Co nanomatch structure was formed only at a specific condition at around $x \sim 20$ and $T_S \leq 300°C$. During the formation of the Ag nanorod, the Co played an important role as a nucleation center. As x increased, the shape of Ag particles changed from rod to spherical ($20 \leq x \leq 40$) and the size of Ag particles increased ($x \geq 40$), leading to the red shift of the LSPR peaks.

Chapter 5: Photoelectrochemical behavior of Ag-Co-TiO_2 film

The contents of Chapter 5 were already published in (Photoelectrochemical Behavior of Self-Assembled Ag/Co Plasmonic Nanostructures Capped with TiO_2", Anri Watanabe, Yuki Kotake, Yoshiomi Kamata, Akira Chikamatsu, Kosei Ueno, Hiroaki Misawa, Tetsuya Hasegawa, *J. Phys. Chem. Lett.*, vol.5, pp. 25-29, 2014.1., and its supporting information: http://pubs.acs.org/doi/suppl/10.1021/jz402320p).

5-1. Introduction

Localized surface plasmon resonance (LSPR) induced by Ag nanostructures exhibits large optical electric-field enhancement due to small imaginary part of its dielectric constant in the visible wavelength region [U. Kreibig, 1995][K. L. Kelly, 2003]. The LSPR properties of Ag are expected to have promising applications such as surface enhanced Raman spectroscopy (SERS) [C. L. Haynes, 2003][Y. Fang, 2008][M. Fleischmann, 1974][D. L. Jeanmaire, 1977][M. G. Albrecht, 1977], photoelectric conversion [M. Westphalen, 2000][A. P. Kulkarni, 2010][W. J. Yoon, 2010], surface-plasmon-assisted nanolithography [W. Srituravanich, 2005][X. Luo, 2004], sensing [J. J. Mock, 2003]. Ag has achieved photocatalytic activity in the longer wavelength of light [J. Yu, 2009][X. Zhou, 2010][M. K. Kumar, 2011][D. B. Ingram, 2011], as the resonant wavelength of LSPR can be tuned by the Ag structure. Moreover, the photocatalytic activity itself can be boosted by the electric field enhancement of Ag nanostructures, whose plasmon resonance was intentionally set to vicinity of UV region so that the bandgap of

TiO_2 and the Ag LSPR band spectrally overlap [K. Awazu, 2008].

The photoelectric conversion using Ag nanostructures, catalytically loaded on the surfaces of nanoporous TiO_2 films, has been investigated by Tatsuma *et al* [Y. Tian, 2004]. They found that the TiO_2 film with Ag nanoparticles shows four times higher conversion efficiency than that with Au nanoparticles. Under irradiation of visible light whose wavelength is corresponding to the LSPR band of Ag nanoparticles, the Ag nanoparticles dissolved into water. This is probably because LSPR induces the photooxidation, photoexcited electrons are transferred from Ag to the conduction band of TiO_2 and, subsequently, produced Ag^+ ions dissolve into water or solution [K. Naoi, 2004].

However, the TiO_2-Ag nanoparticle composite has a serious drawback as a photoconversion system that the Ag nanoparticles easily sulfidate and oxidate in ambient air even if they are preserved under dark condition, resulting in disappearance of Ag plasmon resonance [L. Wang, 2011]. In order to avoid the chemical deterioration of Ag, Ag should be buried in a matrix with low O_2 permeability such as oxides [S. Szunerits, 2008] or polymers [G. Manickam, 2012]. The coatings are also used as functional thin films. The high reactivity of silver in ambient condition limits the usage of silver and it was difficult to use bare silver for SERS signal in the solution [G. Manickam, 2012]. However, from a point of sensitivity as a sensor, it is better for biomolecules to interact with fresh Ag directly. The protection of Ag and the sensitivity are in the relationship of trade off. If it becomes possible for the fresh Ag surface to be exposed just

before the measurement, both Ag protection and good sensitivity are satisfied. Thus the device would have outstanding(distinguishing) features compared with conventional ones.

Recently, Ag/Co nanostructure was successfully embedded in anatase TiO_2 film in a self assembled manner by depositing a mixture of Ag_2O, CoO and TiO_2 with pulsed laser deposition (PLD) method. Each Ag-Co nanostructure has a characteristic nanomatch shape composed of a Co sphere at the bottom (substrate side) and a Ag rod at the top (film surface side). This composite film showed clear LSPR originating from Ag nanorods in the visible wavelength region [A. Watanabe, 2014a][K. Ikemiya, 2014] and, surprisingly, it was clarified that this structure showed same plasmon resonance spectrum even six months after the film deposition. The Ag/Co nanostructure encapsulated in TiO_2 matrix was even stable in various solvents, water, ethanol, acetone; it was confirmed that ultrasonic washing for more than 10 minutes did not affect the lifetime of Ag/Co nanostructures. In addition, the handling of the Ag-Co-TiO_2 films is much easier than the Ag nanostructures made by catalytic loading or the lithography technique.

In this study, I propose photoelectric conversion using the Ag nanorods with long-term stability. According to the cross-sectional TEM-EDX measurements, the Ag nanorods are densely distributed near the TiO_2 film surface. Though most of Co is segregated between Ag nanorods and substrate to form Co nanoparticles, Co oxide (or surface oxidized Co metal) nanoclusters of several

nm scale also reside near the film surface, which prevent Ag nanorods from direct exposed to the air. The oxidation of Co to CoO is electrochemically and thermodynamically favorable than the oxidation of Ag to Ag_2O, the formation of Co oxide layer would suppress the oxidation of Ag [R. Sachan, 2012].

On the other hand, prior to starting the photoelectric conversion, the surface Co protection layer should be removed to make the Ag nanorods contact with electrolyte solution. I refer to this process as ‘unseal’ of Ag. Here I propose an Ag unseal process by using electrochemical oxidation of Co, which enables us to ‘unseal’ Ag at desired time. Furthermore, I demonstrate the potential of the Ag-Co-TiO_2 nanocomposite film as an innovative electrode in plasmonic photoelectrochemical cells; the concept of the sealing/unsealing procedure for the Ag nanostructure is illustrated in Figure 5-1.

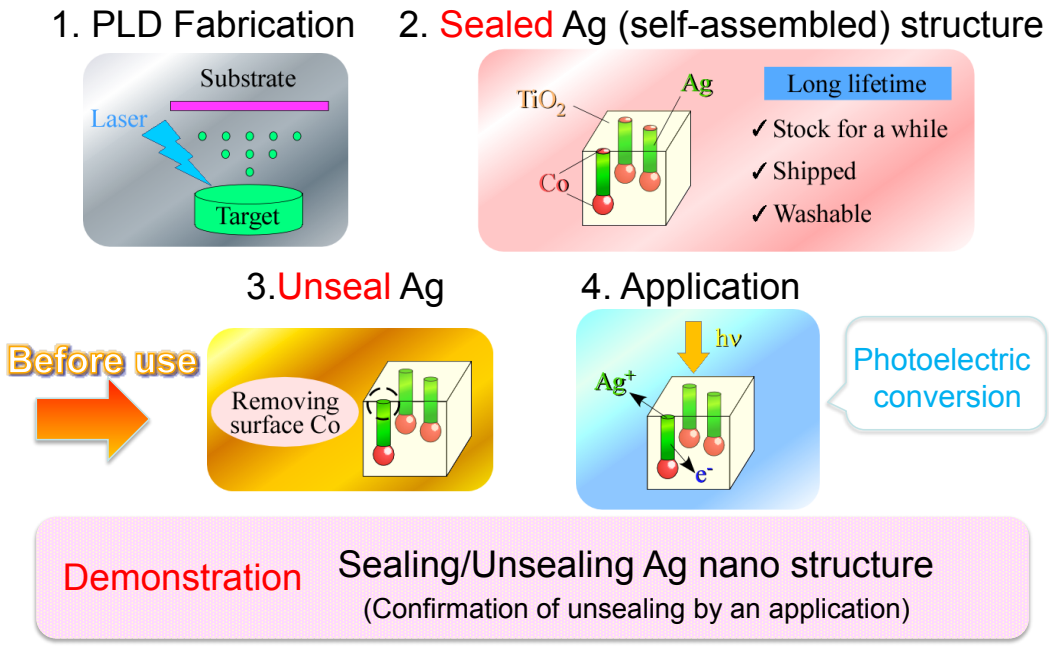

Figure 5-1 Concept of sealing/unsealing procedure for the Ag nanostructure was illustrated. Reprinted with permission from A. Watanabe *et al*, *J. Phys. Chem. Lett.*, vol.5, pp. 25-29, 2014.1., Supporting information. Copyright (2014) American Chemical Society.

5-2. Experiments

Ag-Co-TiO_2 nanocomposite films were fabricated on Nb 0.5wt% or Nb 0.05wt% doped $SrTiO_3$ (Nb:STO) (100) substrate by PLD method. A KrF excimer laser (wavelength λ = 248 nm) operating at a frequency of 2 Hz and energy of 18 mJ/pulse was used for ablation. Sintered pellets of $Ti_{0.97}Nb_{0.03}O_2$ and mixture of Ag_2O:CoO:TiO_2 = 10:5:95 ($Ag_{20}Co_5(TiO_2)_{95}$) were used as PLD targets for seed layers and Ag-Co-TiO_2 nanocomposite film, respectively. A Nb 3% doped anatase TiO_2 seed layer was first deposited on Nb:STO (100) substrate at a substrate temperature (T_s) of 650 °C and oxygen partial pressure (P_{O2}) of 1 × 10^{-5} Torr [H. Nogawa, 2010]. Then, a Ag-Co-TiO_2 nanocomposite thin film was deposited on the seed layers at T_s = 300°C and P_{O2} = 1 × 10^{-6} Torr. The typical film thickness including $\lesssim$5 nm-thick seed layer was ~25 nm. The composition of the Ag-Co-TiO_2 nanocomposite film (nominal composition: $Ag_{20}Co_5(TiO_2)_{95}$) was evaluated to be $Ag_6Co_3(TiO_2)_{91}$ by ICP-MS (Thermo Scientific, XSeries2 ICP-MS with New Wave, UP-213 laser ablation system). The total Ag amount of a Ag-Co-TiO_2 film was also estimated precisely with ICP-AES measurement (Thermo Scientific, iCAP 6300 Duo), by dissolving Ag with 30% HNO_3 (Figure 5-2).

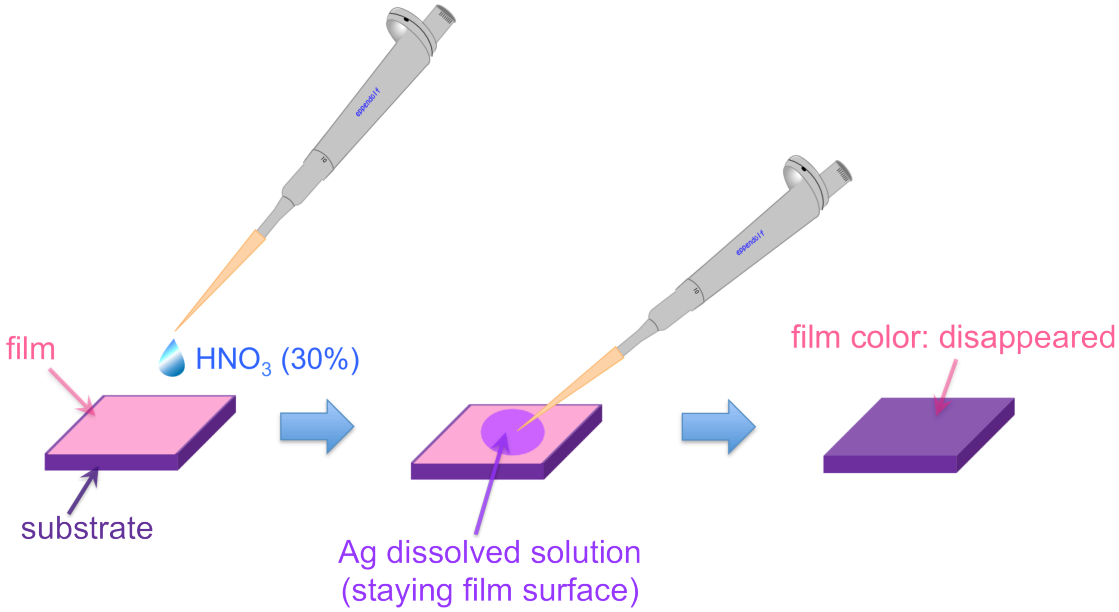

Figure 5-2 All Ag contained in a Ag-Co-TiO_2 film was dissolved by droplets of 30 % HNO_3 solution until the film color totally disappeared. Each droplet was put on the film side, staying on the film surface due to surface tension, then collected by a micropipette.

Cross-sectional and plain view images were taken by bright field scanning transmission electron microscopy at 200kV (JEOL, JEM-2100F HC) with the aid of energy dispersive X-ray analysis (EDX) and electron energy-loss spectroscopy (EELS). Crystal structures of the films were characterized by a X-ray diffraction (XRD) spectrometer with a two dimensional detector (Bruker, AXS with GADDS). Extinction spectrum measurements were performed using a microscopic absorption spectroscopic measurement system. A collimated beam from a halogen lamp mounted on an optical microscope (BX-51, Olympus Co., Japan) was employed as a probe light source for the extinction spectrum measurement. The beam was collimated using a condenser lens of the

microscope. The transmitted beam was collected using a 10× microscope objective lens (a numerical aperture (NA) of 0.3). The probe beam was subsequently coupled to a multichannel photodetector (PMA-11, Hamamatsu Photonics K.K., Japan) after passing through a pinhole (ϕ : 1.0 mm). The recorded spectra were normalized to the spectrum of the incident beam.

Photoelectrochemical measurements were performed using a three-electrode electrochemical measurement system at room temperature. The $Ag_6Co_3(TiO_2)_{91}$ film, a platinum wire and a saturated calomel electrode (SCE) were used as working, counter and reference electrodes, respectively [Y. Nishijima, 2010]. As an electrolyte solution, Ar saturated 0.1 M $KClO_4$ aqueous solution was used without any electron donors. The working electrode was set in a teflon made cell for an electrochemical measurement. The light was introduced through an optical window (ϕ : 2 mm) of the teflon cell. As a light source, a Xenon lamp (Xenon Research Arc Lamp Sources, Newport Co.) was used and the irradiation wavelength was selected by a bandpass filter or a cut filter. In the incident photon-to-photocurrent efficiency (IPCE) measurements, the light monochromatized by bandpass filters (full width at half maximum = 10 nm) was used. In order to extract photocurrent from the working electrode, Nb:STO substrate was back-contacted with In-Ga alloy paste to achieve an ohmic contact.

For references, pure TiO_2 film, Co-TiO_2 film, Ag-TiO_2 film, were fabricated under the same PLD conditions of Ag-Co-TiO_2 films except target; pure TiO_2

target, Co dopedTiO_2 target (nominal composition: $Co_5(TiO_2)_{95}$), Ag doped TiO_2 target (nominal composition: $Ag_{20}(TiO_2)_{95}$) were used, respectively.

5-3. Results and discussion

First I tried to fabricate the Ag nanorod structure capped with anatase, i.e. Ag/Co nanomatch structure embedded in anatase matrix, on the conductive NSTO (100) substrates. Since the Ag/Co nanomatch structure appeared on LSAO substrates at a specific PLD condition as described in the previous chapter, the same PLD conditions were used for films on NSTO substrates. This was the first time to fabricate the Ag and Co co-doped TiO_2 (Ag-Co-TiO_2) films on the substrates, other than LSAO. The surface morphology was observed with SEM and conductive AFM (Figure 5-3 (a)).

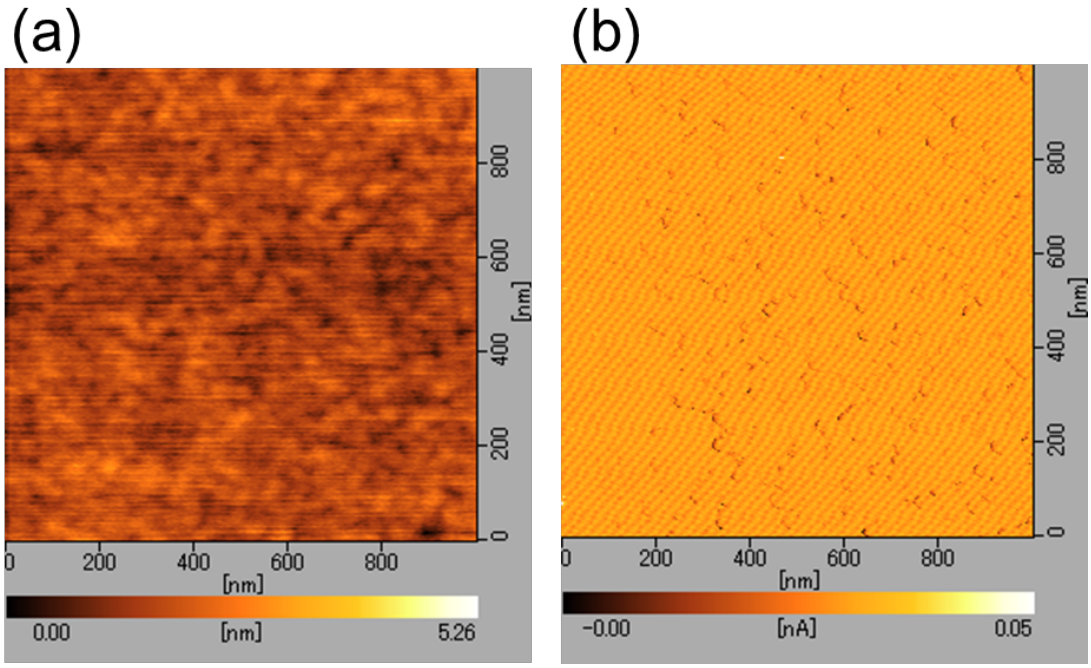

Figure 5-3 (a) Surface morphology of Ag-Co-TiO_2 films measured by AFM, (b) Current mapping measured by conductive AFM at the exactly same place of (a).

The surface was smooth and no large segregation was observed, suggesting that most of the doped metals were embedded in the film matrix. Figure 5-3 (b) was the current mapping measured by conductive AFM (c-AFM), at exact same place with Figure 5-3 (a). Very small value of current was measured, when -0.2 V was applied to the substrate. Some tiny dots appeared. Since the current measurements were also affected by the roughness, it was assumed that the large line or the large (several tens of nm) circles might be due to the surface morphology. From Figure 5-3 (b), it was speculated that some tiny dots of less than 10 nm indicated metal particles in the film.

Since the nm-sized roughness of the film became obstacle in the detecting metallic nanostructure with c-AFM measurements, the higher resolution SEM measurements with larger area were performed. Figure 5-4 was the plain view SEM image of as-deposited Ag-Co-TiO_2 films.

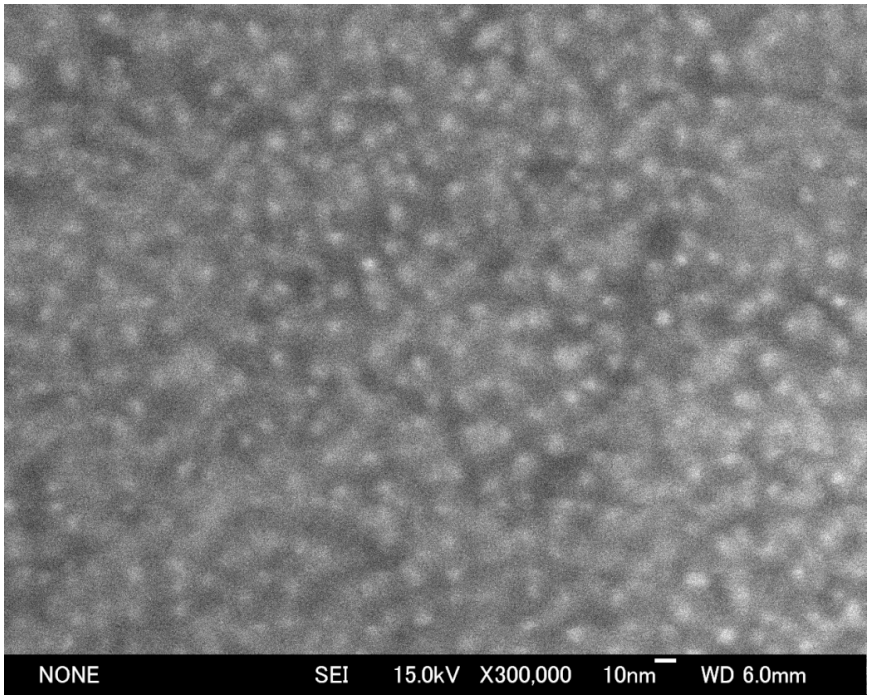

Figure 5-4 SEM image of the surface of Ag-Co-TiO_2 films.

Many white spots (diameter $\leq$ 10 nm), assumed to be metallic nanostructures, were observed. The edge was vaguely imaged, not due to the inadequate focus. The surface was smooth or the height of spots was quite small, being consistent with the previous AFM measurements. This indicates that metallic nanostructures located near the film surface were imaged as spots but not sticking out of the film surface.

In order to investigate the finer nanostructures, the cross-sectional and plain view STEM-EDX measurements were performed on Ag-Co-TiO_2 films (Figure 5-5).

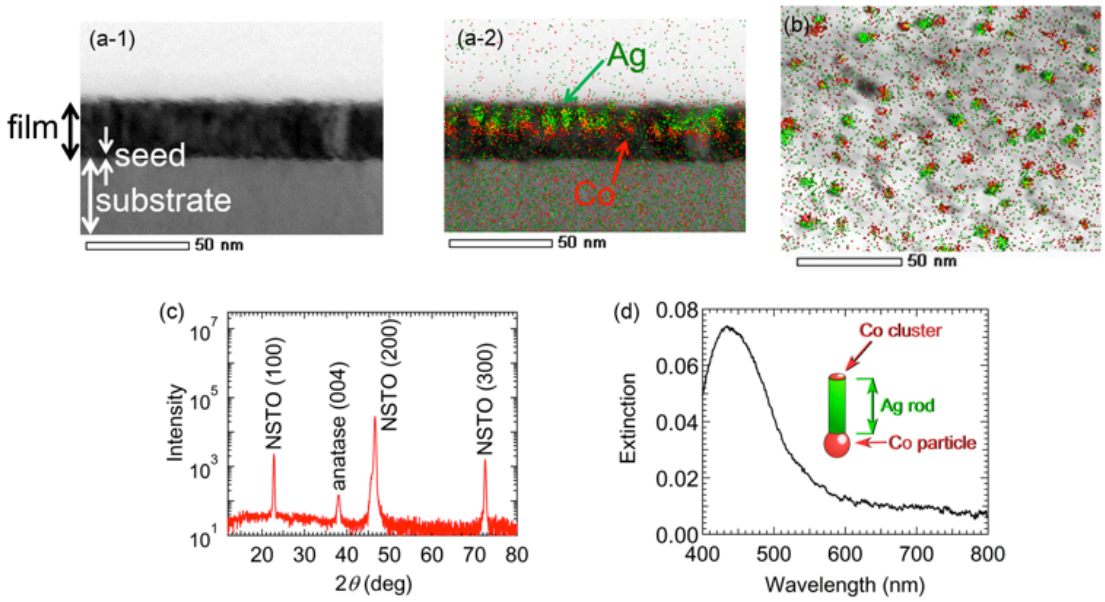

Figure 5-5 (a) Cross–sectional and (b) plain view TEM-EDX images of the Ag-Co-TiO_2 film. (a-1) TEM image without EDX map, (a-2) and (b) TEM images with EDX maps. Ag and Co are depicted in green and red, respectively. (c) θ–2θ XRD pattern of the Ag-Co-TiO_2 film. The peaks from the Nb:STO substrate are labeled by NSTO. (d) Extinction spectrum of the Ag-Co-TiO_2 film. Inset schematically illustrates the shape of Ag-Co nanostructure."

Reprinted with permission from A. Watanabe *et al*, *J. Phys. Chem. Lett.*, vol.5, pp. 25-29, 2014.1., Copyright (2014) American Chemical Society.

The thickness of the film was ~25 nm, including the seed layer of ~2 nm-thick. Figure 5-5 (a-2) showed that Ag nanorods of ~5 nm in diameter and ~10 nm in height were on the Co nanospheres. I succeed in obtaining the characteristic Ag/Co nanomatch structures even on the NSTO substrates. The Ag/Co nanomatch structures were located in the film matrix, ~5 nm apart from the seed layer. The characteristic Ag/Co nanomatch structure was observed when the

thickness of Ag-Co-TiO_2 film fabricated on a NSTO substrate was ~ 25 nm, which was different from the thickness of the film on a LSAO substrate (~ 40 nm), indicating that the thickness of the Ag-Co-TiO_2 film suitable for reproducing the characteristic Ag/Co nanomatch structure is dependent on the substrate. It seemed that the Ag nanorods just below the film surface were denser on the NSTO substrate than those on LSAO substrate in the previous chapter. Moreover no Ag segregates on the film surface when NSTO substrate was used, while some of the Ag structures protruded and segregated a little on the film surface when LSAO substrates were used. This was possibly because the lattice constant of NSTO (the lattice constant of STO: a = 0.3905 nm) substrate was larger than that of LSAO (the lattice constant of LSAO: a = 0.3755 nm, c = 1.262 nm), which was assumed to make the binding of TiO_2 crystals looser and the space of metal nanoparticle became wider. As seen from the plain view STEM–EDX image shown in Figure 5-5 (b), the lateral positions of the Ag nanororods in the film were random (illustrated in Appendix Figure 5A-1 for easier understanding) and the averaged interval between adjacent nanomatches was 10–20 nm. The lateral positions of each Ag nanorod and Co particle were identical, which was the evidence of the nanomatch structures. Some of the Ag particles appeared in oval shapes from the top view, not circular, due to the tilting of the Ag nanorods (Appendix Figure 5A-2). Then the crystal structure was characterized by XRD measurements (Figure 5-5 (c)). The θ-2θ XRD pattern clearly showed anatase 004 peak at 2θ = 38°. No secondary peaks were

observed, indicating that the Ag/Co existed as nano particle form. Since the anatase peak appeared as a spot in the 2θ-χ image in the two dimensional detector, the film matrix was confirmed to be a single crystal of anatase (Appendix Figure 5A-3). Besides in the cross-sectional high resolution TEM image of Ag-Co-TiO_2 films (Figure 5-6), the lattice image shows that the anatase matrix were epitaxially crystalized without amorphous phase formation.

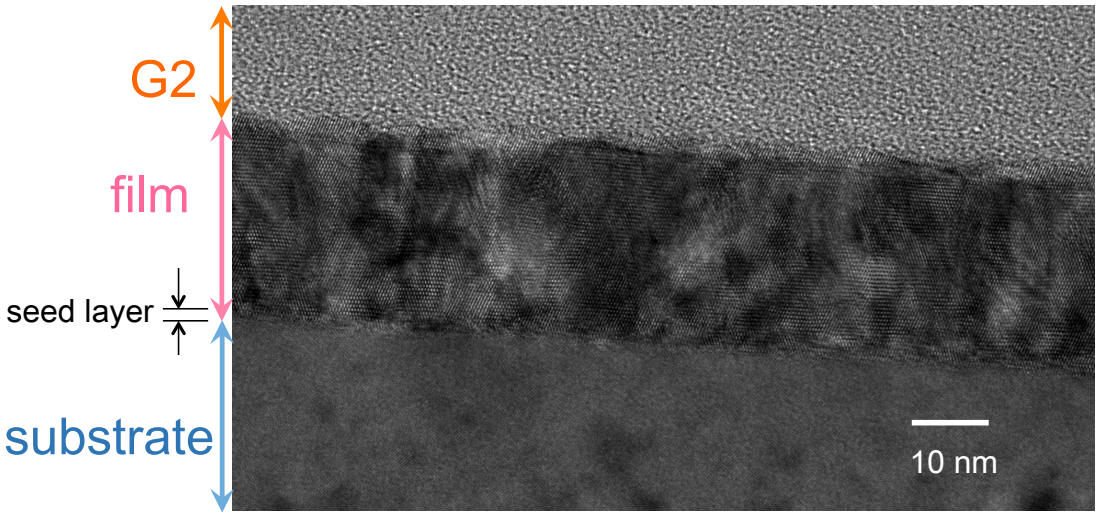

Figure 5-6 Cross-sectional high resolution TEM image of Ag-Co-TiO_2 films.

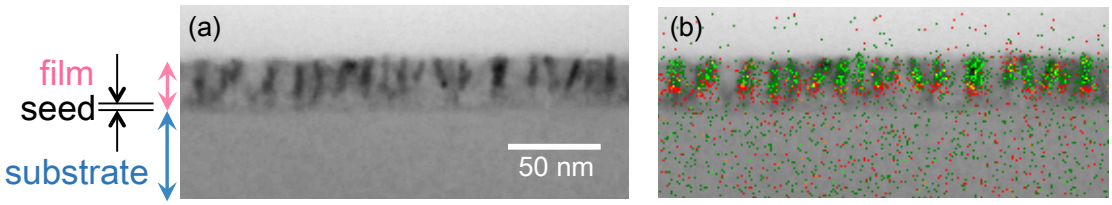

Figure 5-7 Cross–sectional TEM-EDX images of the Ag-Co-TiO_2 film in order to show the reproducibility. (a) TEM image without EDX map, (b) TEM images with EDX maps. Ag and Co are depicted in green and red, respectively.

The reproducibility of the Ag/Co nanostructure was confirmed in Figure 5-7: the cross sectional STEM-EDX image of a Ag-Co-TiO_2 film fabricated on a different day from that of Figure 5-5. The film with ~25 nm in thickness clearly showed characteristic Ag/Co nanostructure (Ag nanorods on the Co nanospheres) embedded in TiO_2 matrix. The density of the Ag/Co nanorods structure seemed smaller than that of Figure 5-5 (a-2), because of the smaller thickness of the TEM sample. Not only EDX but also EELS measurement was conducted in Figure 5-8, in order to confirm whether metal nanostructures were oxidized.

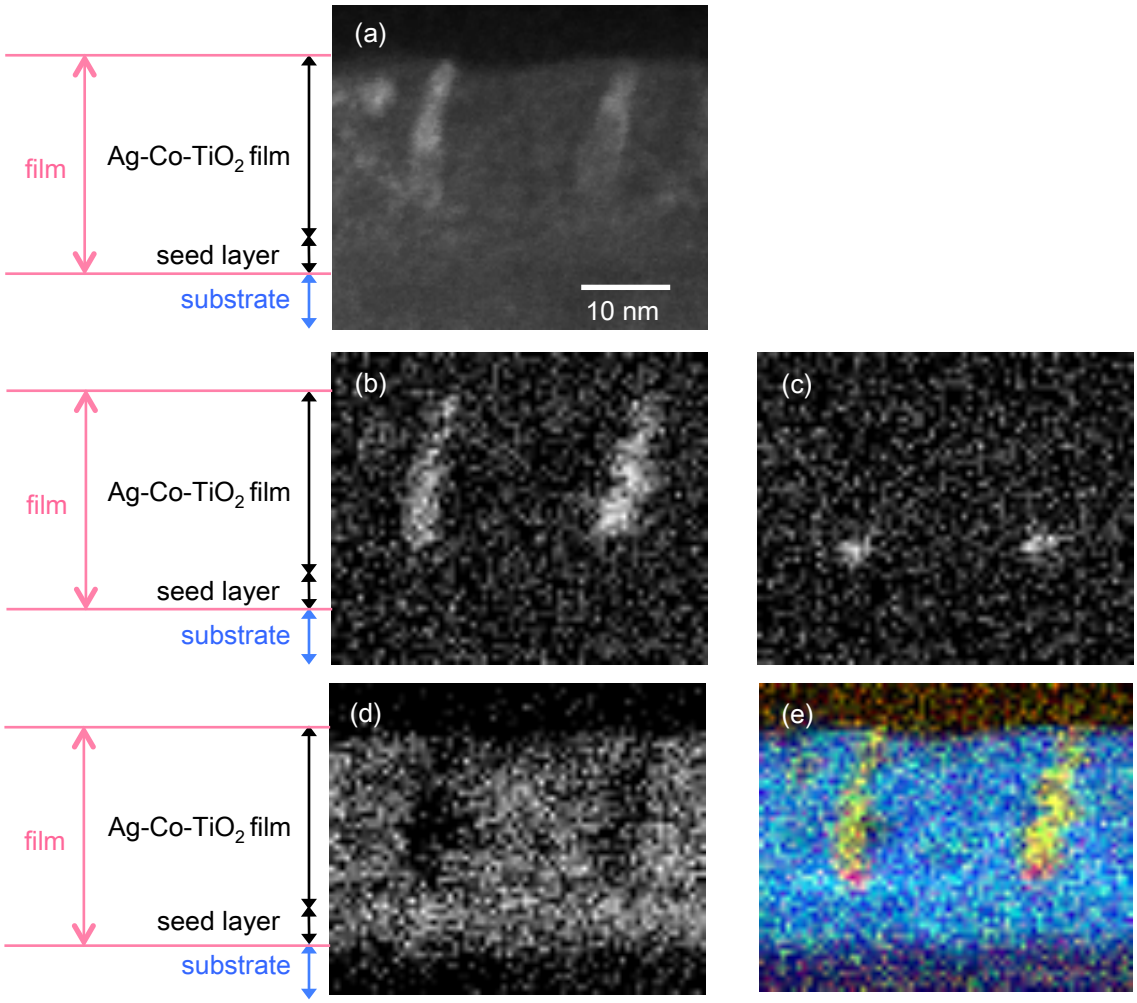

Figure 5-8 (a) Cross section low-angle annular dark-field (LAADF) STEM image, and (b)-(e) EELS images of the Ag-Co-TiO_2 film. EELS mapping image of (b)Ag (M line, 398.3 - 426.3 eV), (c)Co (L line, 771.3-802.0 eV), (d)O (K line, 528.5-559.3 eV), (e) overlayed image of Ag (green), Co (red) and O(blue).

The Ag nanorods were embedded in anatase matrix (Figure 5-8 (b)), manifesting the immiscibility of Ag and Co. The Ag/Co nanostructures were preserved even after the TEM sample making, which took at least several days to polish after ultrasonically washing in acetone. Moreover, the Ag nanorods and Co nanospheres were not oxidized; the oxygen mapping was missing at the place of Ag/Co nanostructures.

In order to investigate the optical property of the Ag-Co nanostructures, an extinction spectrum was measured (Figure 5-5 (d)). The incident light direction was perpendicular to the film surface (Figure 5-9 (a)).

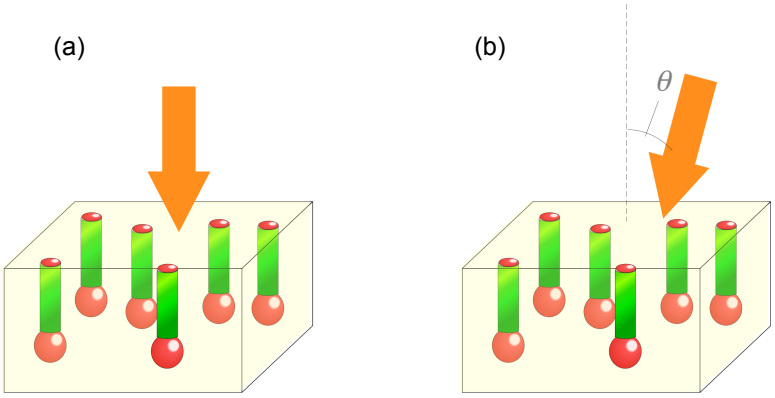

Figure 5-9 Incident light direction, (a) perpendicular to film normal, (b) tilted slightly from the film normal. Reprinted with permission from A. Watanabe *et al*, *J. Phys. Chem. Lett.*, vol.5, pp. 25-29, 2014.1., Supporting information. Copyright (2014) American Chemical Society.

A clear LSPR peak of Ag nanorods was observed at around 400 to 600 nm in wavelength. The LSPR peak of Ag was enhanced and red shifted due to the surrounding environment, totally embedded in anatase matrix [W. L. Shi,

2006][C. Novo, 2008][M. D. Malinski, 2001][Y. J. Jen, 2014]. The peak was broad because the lateral positions of Ag nanorods were random (Appendix Figure 5A-1). The nanorods were almost oriented perpendicular to the film surface; however, some of the Ag rods were tilting. As the incident light direction was perpendicular to the film surface (parallel to the Ag rods), basically only transverse mode was enhanced. However, the oval shape of Ag rods observed in the plain view STEM-EDX images implied the tilting rods seen from the top (Appendix Figure 5A-2). The LSPR spectrum was thought to be the mixture of the transverse and longitudinal modes. However, the two modes were not distinguishable in the spectrum, that is, only a single peak was observed in the extinction spectrum, because the tilt angle was different from a rod to another. Although the incident light direction, θ in Figure 5-9 (b), was changed from 0-10°, almost no spectral change was observed, because some of the rods were originally tilted several degree.

Since the aimed plasmonic Ag nanostructures protected by anatase matrix were obtained, it was expected that the plasmon resonance would assist the photoelectric conversion. The surrounding TiO_2 matrix of anatase fabricated under reductive condition might work favorably, because anatase shows higher photocatalytic activity than rutile due to longer electron/hole pair lifetime [M. Xu, 2011], and TiO_2 with oxygen vacancy shows better photoelectric conversion property than pristine TiO_2 due to more rapid electron transport [H. Chen, 2014].

The current was monitored with photoelectrochemical measurements,

applying 0.1 V vs saturated calomel electrode (SCE) under the irradiation of the 450 nm wavelength light. However no photocurrent enhancement was observed, compared with that of pure TiO_2 films. This was because the silver nanostructures were completely protected by the titania matrix and the surface cobalt oxide (or surface oxidized Co metal) nanoclusters on the top of silver nanorods. I concluded that a tiny Co oxide (or surface oxidized Co metal) covered the other end (the film surface side) of the Ag rods, for the following reason.

Figure 5-10 (1^{st} sweep) was the current voltage curve of the Ag-Co-TiO_2 nano-composite films observed under the dark condition. A clear peak was observed at around 0.2 V versus SCE, which corresponds to the oxidation of surface Co oxide (or surface oxidized Co metal) clusters. The peak intensity decreased as I repeated the scan, indicating that the clusters composed of Co species which were located near the film surface went out into the solution.

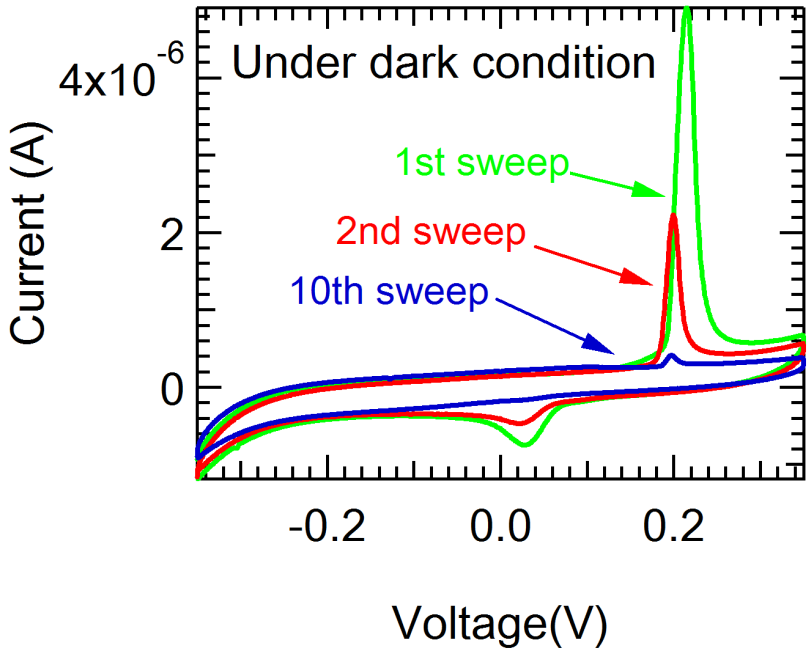

Figure 5-10 Current voltage curve of the nano-composite film observed under the dark condition at original (green), second (red), 10th (blue) scan. The scan rate was 0.05 V/s, scanning from -0.35 V to 0.35 V at room temperature. Modified with permission from A. Watanabe *et al*, *J. Phys. Chem. Lett.*, vol.5, pp. 25-29, 2014.1., Supporting information. Copyright (2014) American Chemical Society.

Moreover, if the Co particles at the bottom (substrate side) dissolve at ~0.2 V, almost all Co should be dissolved into the solution and most of the Ag nanorods located at the surface side should be eliminated altogether. However, the total amount of dissolved Co, until the peak became small enough, was actually only about 10% of the total Co amount in the film; where the sum quantity of electricity was calculated from peak area. This clearly indicates that about 10%

of Co component resides at the surface as Co oxide (or surface oxidized Co metal) clusters. It is thought that the most parts of the clusters, or at least the outermost surfaces of the clusters are oxidized, leading to the higher oxidation potential. Thus I called them as “Co oxide (or surface oxidized Co metal) clusters”. Strictly speaking, not all Co segregates below the Ag rod positions, i.e., small amounts of Co also segregate beside or above the Ag rods, since the metal Co and Ag segregate in a totally self-assembled manner. Though it is not clear why a small amount of Co components reside on the top of Ag rods, Co favors to segregate on the film surface as well as to locate between Ag rod and anatase crystal.

I also fabricated the only Co or Ag doped films as references Co-TiO_2 film and Ag-TiO_2 film. The cross-sectional STEM-EDX images of Co-TiO_2 film was shown in Figure 5-11, Co metal nanoparticles were randomly spread over the film and embedded in the TiO_2 matrix. Figures 5-12 and Figure 5-13 are the current voltage curves of Co-TiO_2 films and Ag-TiO_2 films, respectively.

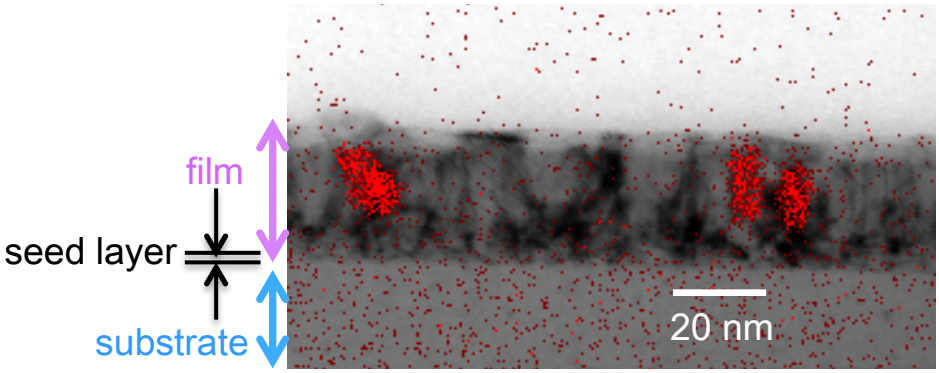

Figure 5-11 Cross–sectional TEM-EDX images of the Co-TiO_2 film, where Co is depicted in red color.

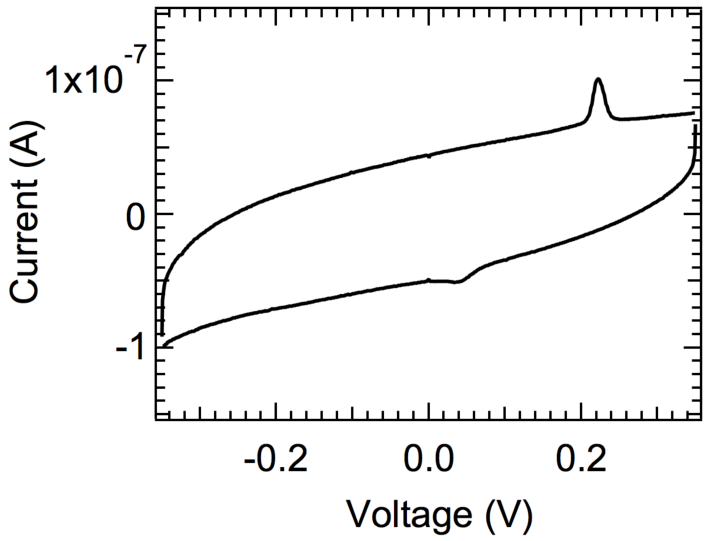

Figure 5-12 Current voltage curves of Co-TiO_2 films. The scan rate was 0.05 V/s, scanning from -0.4 V to 0.35 V at room temperature.

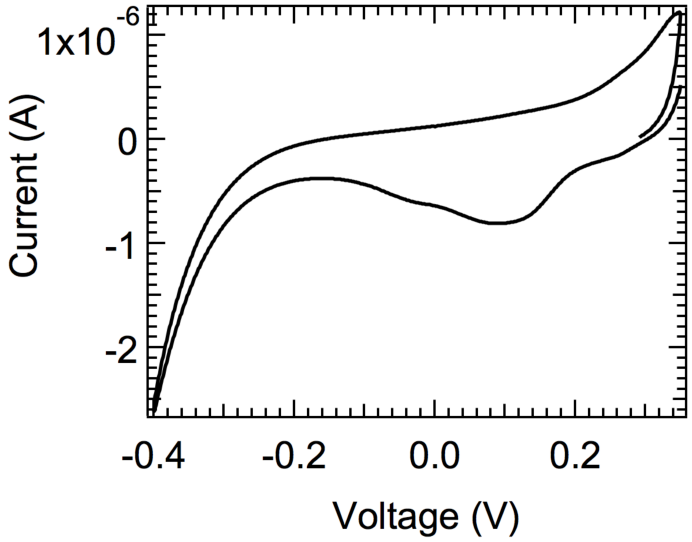

Figure 5-13 Current voltage curves of Ag-TiO_2 films. The scan rate was 0.05 V/s, scanning from -0.4 V to 0.35 V at room temperature.

The oxidation peak position of the former film was as same as that of Ag-Co-TiO_2 film (Figure 5-12). On the contrary, no peak appeared at around 0.2 V vs. SCE in Ag-TiO_2 film (Figure 5-13), supporting that the substance capping the Ag nanorod was Co. Thus it was proved that Ag nanorods were sandwiched by Co nanospheres (5~10 nm in diameter) at the bottom and the tiny nanoclusters composed of Co species (< 5nm size) on the top from the electrochemical measurements. However the tiny Co oxide (or surface oxidized Co metal) clusters were difficult to be seen in the cross sectional STEM-EDX image (Figure 5-7, 5-8) due to the limited spatial resolution. In as-deposited

Ag-Co-TiO_2 films, TiO_2 matrix and the Co oxide (or surface oxidized Co metal) nanoclusters totally capped Ag nanorods and prevented the Ag nanorods from exposure to the air/solutions.

In order to perform the photoelectric conversion, the Ag nanorods should be contact with the solution. (It was proved in the Appendix; the photoelectrochemical measurement of Ag-TiO_2 films and Ag-Co-TiO_2 films capped by thin TiO_2 layer.) In order to remove the cobalt oxide (or surface oxidized Co metal) nanoclusters preferably, we applied the relatively higher voltage than Co oxidation and lower voltage than silver oxidation, applying 0.3 V versus SCE under darkness for 100 seconds. This is hereafter called *initialization*. Inductively coupled plasma-mass spectroscopy (ICP-MS) revealed that during the *initialization*, small amount of cobalt dissolve in the solution. For comparison, 0.3 V versus SCE was also applied to the Co-TiO_2 film and the surface morphology was observed in Figure 5-14 and 5-15. It was obvious that a part of Co was electrochemically dissolved into the solution, even Co were completely embedded in TiO_2 matrix (Figure 5-11).

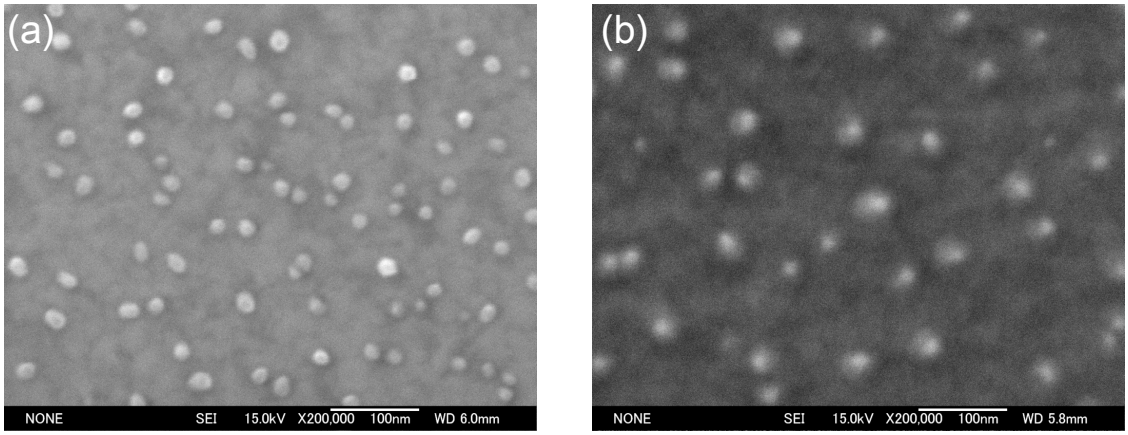

Figure 5-14 Surface morphology of Co-TiO_2 films measured by SEM, (a) as deposited film, (b) after applying 0.3 V versus SCE.

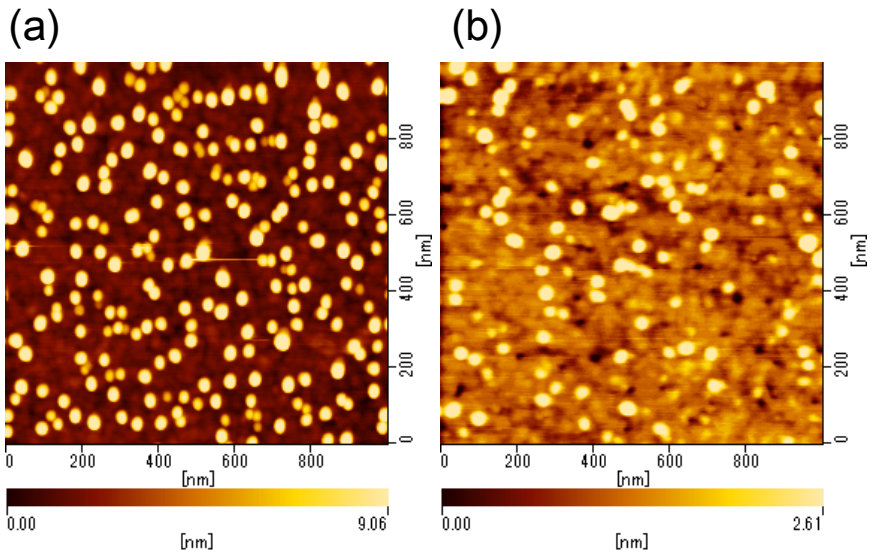

Figure 5-15 Surface morphology of Co-TiO_2 films measured by AFM, (a) as deposited film, (b) after initialization.

The number of the Co particles decreased in both SEM and AFM images, while the spots in SEM image became blurred, and even holes can be seen in AFM image. Thus I concluded that the clusters composed of Co species which located near the film surface in Ag-Co-TiO_2 films dissolved into the solution by *initialization*.

Figure 5-16 (a) showed the linear sweep voltammogram of Ag-Co-TiO_2 films, with/without light irradiation ($420 < \lambda \leq 1300$) after the initialization.

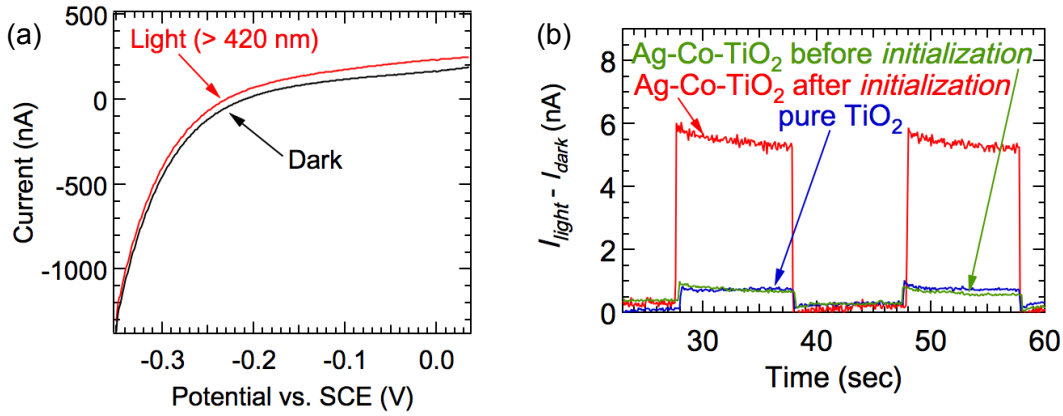

Figure 5-16 (a) Linear–sweep voltammogram of Ag-Co-TiO_2 films, with and without light irradiation after *initialization*. The sweep rate was 0.05 V/s, scanning from -0.4 V to 0.35 V at room temperature. (b) Amperometric *I–t* curves before and after *initialization* under irradiation of light (λ = 450 nm). The working electrode potential (*V*) was set to 0.1 V vs. SCE." Reprinted and modified with permission from A. Watanabe *et al*, *J. Phys. Chem. Lett.*, vol.5, pp. 25-29, 2014.1., Copyright (2014) American Chemical Society

The current was clearly enhanced under the irradiation of light, representing the anodic photocurrent. Amperometric current-time (*I-t*) curves were also measured, before and after the *initialization* (Figure 5-16 (b)). The measurement condition was under light irradiation (λ = 450 nm) and the working electrode potential was set to 0.1 V vs. SCE. Although the current of Ag-Co-TiO_2 films before *initialization* was not enhanced compared with that of pure TiO_2 films, the current of Ag-Co-TiO_2 films after initialization was enhanced seven times. This result proved that the Ag nanorods, originally "sealed" in a TiO_2 matrix by the surface Co oxide (or surface oxidized Co metal) nanoclusters, were successfully unsealed by the initialization process. Here I developed the way to unseal silver nanostructures by removing surface cobalt oxide (or surface oxidized Co metal) nanoclusters. The Ag and Co contents dissolved into solutions during the *initialization* process were estimated to be 10% and 5.5% of total Ag content and Co content in entire film, respectively, using ICP-MS. It was peculated that the nanoscale channels between Ag nanorods and the solution were created by *initialization*. *Initialization* process (generated by a 0.3 V versus SCE relative to the working electrode in the neutral solutions) oxidized not only surface clusters composed of Co species but also a part of Ag [M. Pourbaix, 1974]. The rate of the dissolving was larger in Ag than Co, because the most Ag were distributed densely just below the film surface, while most Co component was located in the substrate side. Once Ag contacted the solutions, the photocurrent could flow due to the photooxidation of Ag (Ag^0 to Ag^+) based on plasmon-induced charge

separation. At the same time, the Ag^+ ions were produced and dissolved into the solution.

I also measured the photocurrent of silver and cobalt nanostructures in other wavelengths of light, then calculated the incident photon-to-photocurrent efficiency, IPCE. Figure 5-17 compared the IPCE action spectrum and the LSPR peak of extinction spectrum shown in Figure 5-5 (d).

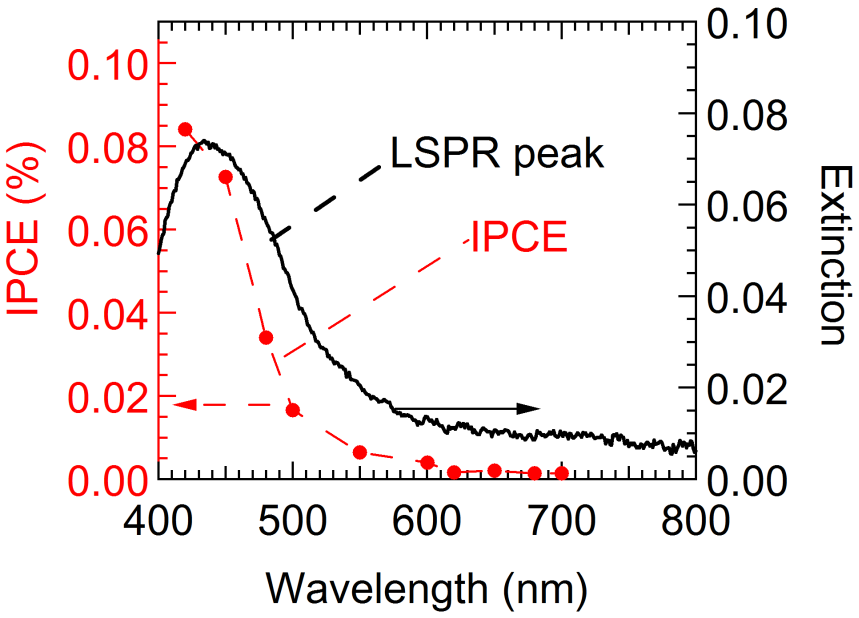

Figure 5-17 IPCE action spectrum (black solid line) and the extinction spectrum (red dotted line). Reprinted with permission from A. Watanabe *et al*, *J. Phys. Chem. Lett.*, vol.5, pp. 25-29, 2014.1., Copyright (2014) American Chemical Society.

Both spectra showed quite similar tendency, that is, an abrupt increase of extinction/IPCE with decreasing wavelength below 600 nm. This result strongly suggested that the photocurrent was enhanced by the effect of plasmon resonance. However, there was some inconsistency at the shorter wavelength region: the extinction spectrum has a peak around λ = 440 nm, while IPCE is monotonically increased with shorter wavelength. It was thought that an interband transition of TiO_2 itself contributed to IPCE at λ = 420 nm. The bandgap of pure TiO_2 is originally 3.2 eV, corresponding to ~390 nm in wavelength. The present Ag-Co-TiO_2 films contained a certain amount of oxygen vacancies in TiO_2 matrix because it was fabricated under a reductive atmosphere: low oxygen pressure. The oxygen vacancies form n-type impurity states near the bottom of the TiO_2 conduction band, reducing the bandgap of TiO_2. However, the IPCE value of the pure TiO_2 film at 420 nm (Appendix Figure 5A-4), without Ag and Co, was smaller than 0.01%. Thus, the large enhancement of photocurrent at 420 nm cannot be explained by only interband transition. Since the tail of the TiO_2 band edge overlaps with the LSPR peak, I speculated that the interaction between interband excitation and LSPR substantially enhances the photocurrent, similar to the previous research on photocatalysis [K. Awazu, 2008].

Since the Ag dissolved as Ag^+ ion accompanying the photoelectric conversion, the Ag/Co metal nanostructures disappeared in STEM-EDX image after long photoelectric measurement (14h) under irradiation of light (λ = 450 nm): Ag and

Co no more detected at all in EDX spectrum (Figure 5-18). The LSPR peak also disappeared because Ag nanorods were already consumed. The surface morphology of the Ag-Co-TiO_2 films, after the photoelectric conversion, was also probed by SEM. As seen in Figure 5-19, there were many holes at the locations where Ag/Co nanomatches had existed; the size of holes were comparable to the size of white spots of Figure 5-4.

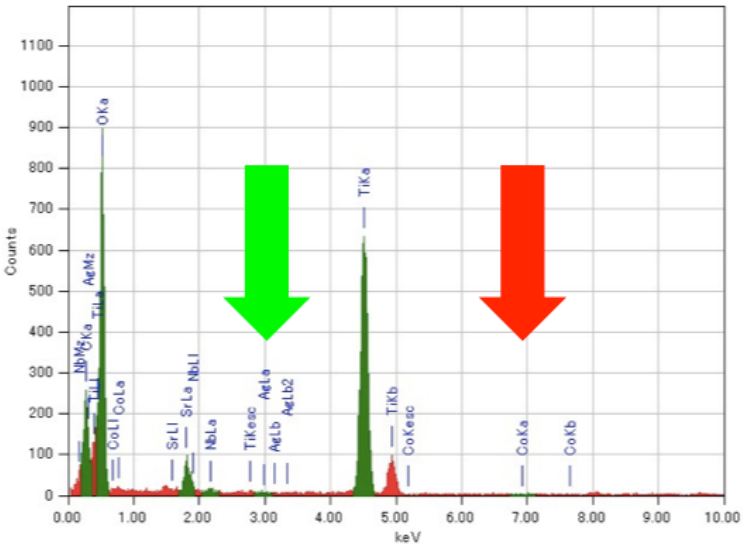

Figure 5-18 EDX spectrum of Ag-Co-TiO_2 films after photoelectric conversion.

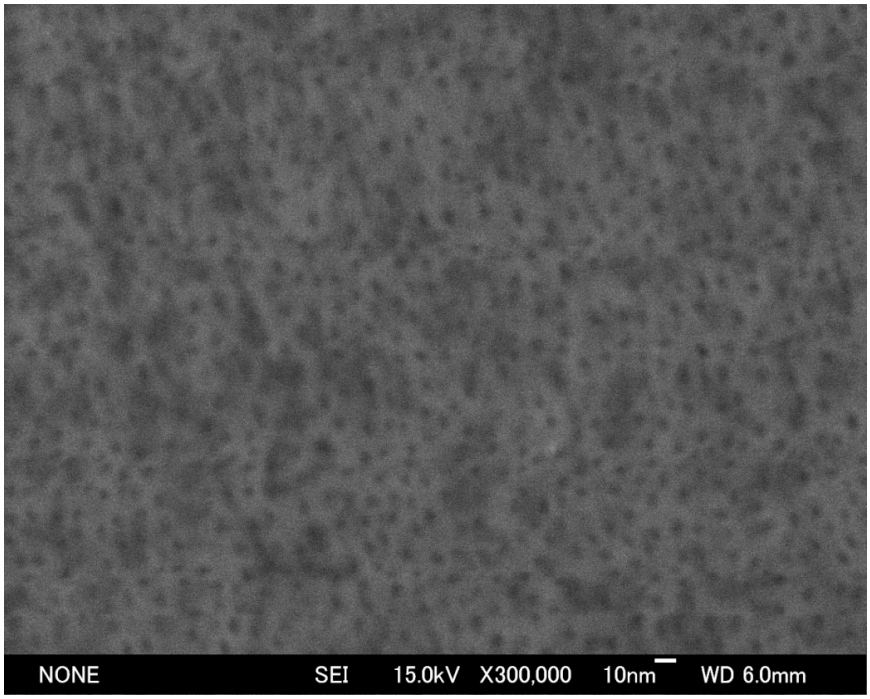

Figure 5-19 Surface morphology of Ag-Co-TiO_2 films after the photoelectric conversion.

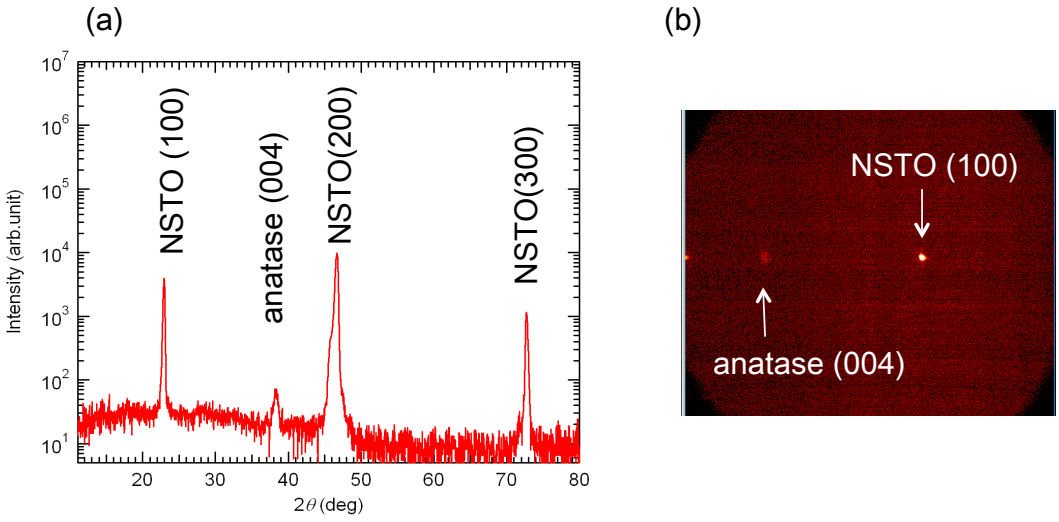

Figure 5-20 (a) θ-2θ XRD pattern and (b) 2θ-χ image (in the two dimensional detector) of Ag-Co-TiO_2 films after the photoelectric conversion.

XRD measurements confirmed that the anatase single crystal structure was still maintained in the film; the remained TiO_2 crystal showed anatase 004 peak as a spot in two dimensional XRD measurements, as shown in the Figure 5-20. The resistivity in the in-plane direction after the photoelectrochemical measurement was approximately 1000 times higher than the initial value, showing that this film is equivalent to insulating pure TiO_2. Although photoelectric conversion would be completed when all the Ag particles dissolved, I obtained the nanoporous anatase single crystal film with small holes less than 10 nm in diameter. This nanoporous film would be also used as a plasmonic devices or photonic crystals, such as gratings.

Deterioration of Ag/Co metal nano structures by oxidation or sulfidation during 14 hours could be neglected. The calculated Ag amount based on the current value was estimated to be 90 % of that contained in the whole film measured by ICP-AES. The value was reasonable, because 10% of Ag content had already dissolved into the solution during the *initialization*. As a consequence, I propose the following photoelectric conversion mechanism (Figure 5-21).

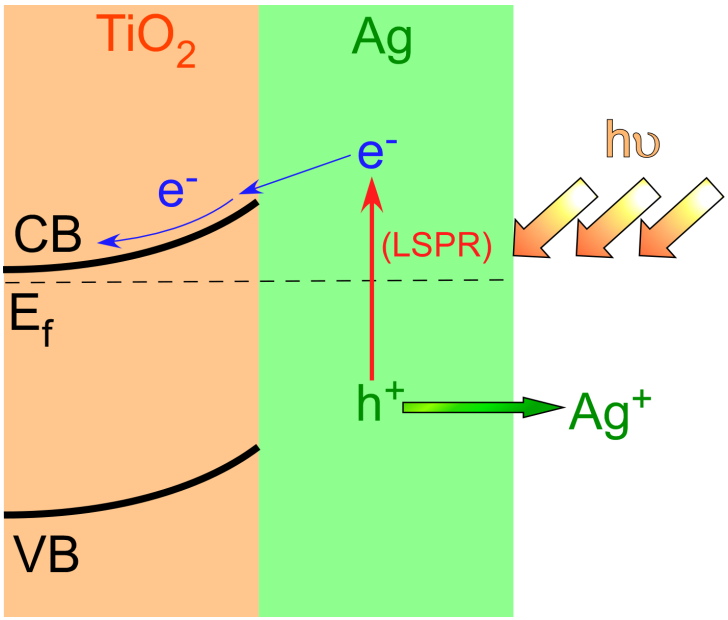

Figure 5-21 The schematic image of the mechanism of photoelectric conversion.

First LSPR of Ag was induced, and then the excited electrons of Ag were transferred from Ag to the conduction band of TiO_2. Accompanied with the generation of the anodic photocurrent, photooxidized Ag dissolved into solutions as Ag^+ ion. As the Ag dissolved into the solution gradually during the photoelectrochemical measurement, the IPCE value would diminish while repeating the scan or even during single scan; it took about 5 minutes for single scan, i.e. measuring photocurrent values from 400 nm to 700 nm. Figure 5-22 shows the relative IPCE values against the IPCE value of a Ag-Co-TiO_2 film at λ = 400 nm of first time sweep. The shape of IPCE spectra in second and third sweep were similar to that in first scan, proving that the spectral shape of the higher value in the shorter wavelength and lower value in longer wavelength was intrinsic behavior of Ag-Co-TiO_2 films, not due to the Ag degradation. Focusing

on each wavelength, the IPCE values decreased by less than 20% from previous scan to the next scan; it seemed large decrease, however, the diminution became smaller with more repetition.

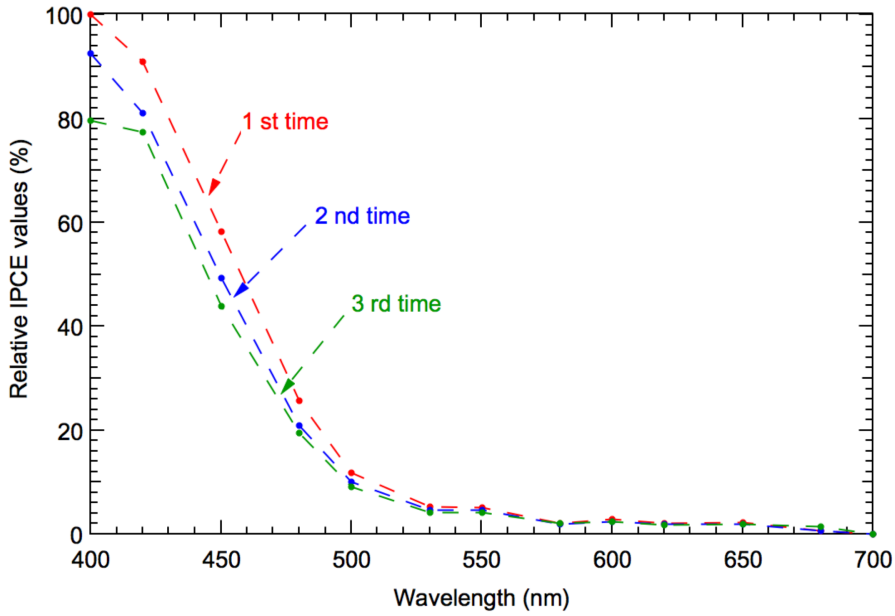

Figure 5-22 Relative IPCE value of a Ag-Co-TiO_2 film, compared with the value of at λ = 400 nm of first time sweep.

Finally the possible applications are discussed here. The remarkable feature we found on the Ag-Co-TiO_2 films is that the silver nanostructures firmly protected for long time, but it can be unsealed when needed. The sealed Ag nano structure is expected to be used in photoelectric conversion, catalysis and sensing, in which the fresh silver surface is needed. As the photoelectric conversion device, the sealed Ag is advantageous compared with bare Ag from the point of preserving Ag. The sealed Ag nanostructure endured even the

shipping and washing, besides it is easy to handle. Ag-Co-TiO_2 film would be suitable for the portable and disposable cell. One problem in the application for the photovoltaic cell is that it cannot be used long time, since Ag is easier to be oxidized than water. However, the lifetime is expected to be elongated by adding a much reductive agent to the solution, which is easier to be oxidized than Ag.

The Ag-Co-TiO_2 films can also be applied in the biosensors such as SERS. So far, once the Ag structure was coated by conventional materials, such as SiO_2 and polymer to preserve Ag nanostructures, it was difficult to remove the coating. In the Ag/Co nanostructures encapsulated in TiO_2, a fresh Ag surface can be prepared by removing the "coating" just before the measurement, which enables Ag nanostructures to react with biomolecules directly. Therefore, the present Ag-Co-TiO_2 system enables both Ag protection and high sensitivity, which is of great advantage over conventional sensors using bare and coated Ag.

5-4. Summary

In summary, I propose the sealed Ag nanorods structure embedded in TiO_2 matrix with long life time, which is extremely durable enough to be washed and transported. It was revealed that this new structure enables us to ‘unseal’ Ag by an electrochemical method, removing surface Co oxide (or surface oxidized Co metal) nanoclusters. I confirmed the Ag contacting to the supporting electrolyte, subsequently succeeded in observing photocurrent generation enhanced by plasmonic resonance of Ag nanorods. The Ag sealed nano structure is expected to used in the applications in plasmonic devices, catalysis, and sensing, in which fresh Ag surface is needed; if it is applied to the biosensors, both Ag protection and good sensitivity will be satisfied to show distinguishing feature compared with conventional ones.

5-5. Appendix ~Photoelectrochemical measurements of Ag-TiO_2 films and Ag-Co-TiO_2 films capped by thin TiO_2 layer~

Ag nanorods were not formed in $Ag_{20}(TiO_2)_{95}$ film due to the absence of Co. Not uniform Ag particles in shape and size are irregularly dispersed in the TiO_2 matrix. Although the Ag nanostructure was different from Ag-Co-TiO_2 film, similar electrochemical measurement was done on Ag-TiO_2 film, in order to know the effect of attachment of Ag and solution. Even after initialization, the IPCE value of Ag-TiO_2 film was as small as that of pure TiO_2 film and photocurrent enhancement by LSPR was not observed, as I expected (Figure 5A-4). According to cross sectional STEM-EDX mapping image of Ag-TiO_2 film after photoelectrochemical measurement, it was revealed that most of the Ag particles remained in the TiO_2 matrix (Figure 5A-5) because Ag particles were completely sealed by TiO_2 matrix. Conversely in Ag-Co-TiO_2 films, the photocurrent enhancement was clearly observed after *initialization*, however Ag dissolved into the solution after photoelectrochemical measurements.

These results indicate that it was not until interior Co oxide (or surface oxidized Co metal) nanoclusters dissolved into solution by *initialization* that Ag rods of Ag-Co-TiO_2 films were exposed to the solution. The enhancement of IPCE value seemed to depend on the efficiency of Ag ionization ($Ag \rightarrow Ag^+$). It was also confirmed by the IPCE values of the Ag-Co-TiO_2 films roughly covered by additional TiO_2 coating on the surface. The TiO_2 coating layer was deposited for 1minute just after the Ag-Co-TiO_2 film fabricated, at the same substrate

temperature (T_S = 300°C) and oxygen pressure (P_{O2} = 1 × 10^{-6} Torr). Since the deposition time was short, the TiO_2 top film might be mottled appearance, with less than 1 nm in thickness. However, unsealing was prevented to some extent at the places covered by the top TiO_2 thin layer; the IPCE value was smaller than that of Ag-Co-TiO_2 films (after *initialization*) and larger than that of Ag-TiO_2 films (Figure 5A-4).

As consequence, in original Ag-Co-TiO_2 films without TiO_2 coating, the fact that Ag particles distributed near the surface intensively helps most Ag particles to contact the solution; this unique structure enabled most Ag particles to contribute to the charge separation.

Appendix Figures

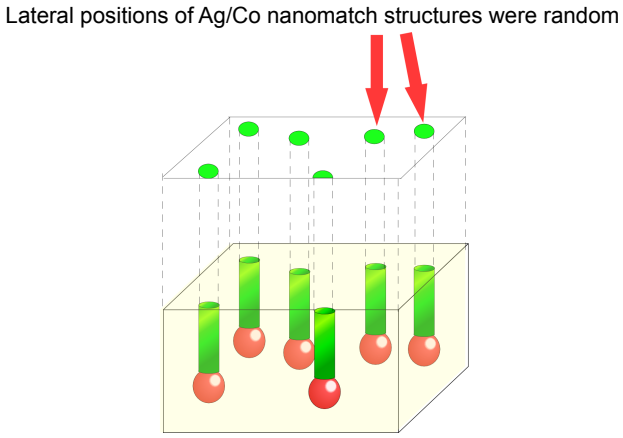

Figure 5A-1 Illustration of randomness of Ag/Co nanostructures.

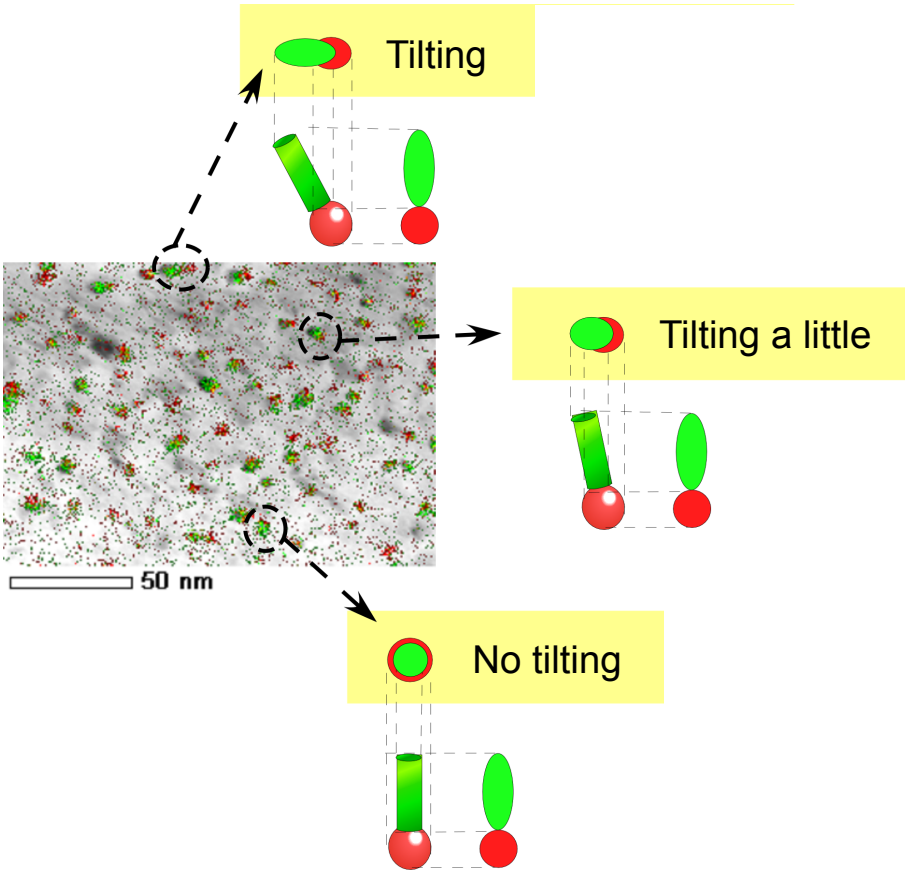

Figure 5A-2 Tilting of Ag/Co nanostructures which can be read from the cross sectional STEM-EDX image.

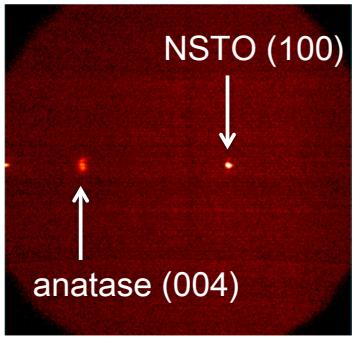

Figure 5A-3 2θ-χ image (in the two dimensional detector) of as deposited Ag-Co-TiO_2 films.

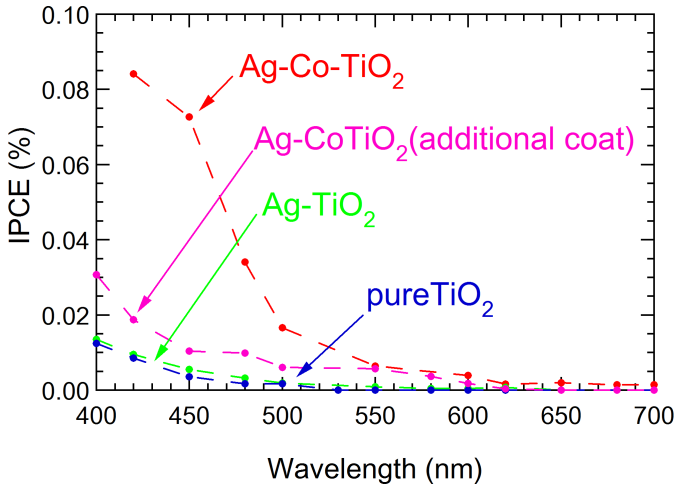

Figure 5A-4 IPCE spectra of Ag-TiO_2 films and Ag-Co-TiO_2 films additionally coated by TiO_2, overlaid on those of Ag-Co-TiO_2 films (Figure 5-17) and pure TiO_2 films.

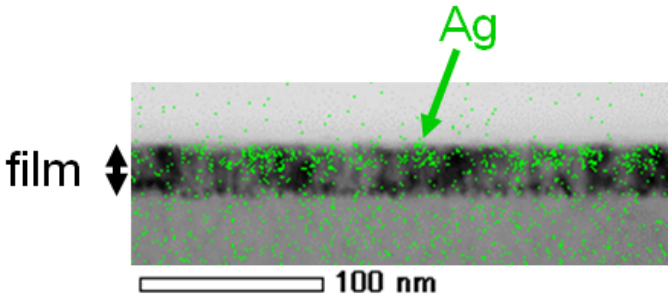

Figure 5A-5 Cross-sectional TEM-EDX image of Ag-TiO_2 film, after the photoelectrochemical measurement, where Ag was depicted with green color.

Chapter 6: Summary and future prospects

I investigated the structural and electrochemical properties of nanocomposite films composed of Ag/Co metal nanostructure and TiO_2 matrix (Ag-Co-TiO_2 films). In order to utilize the plasmonic Ag nanostructures in practical applications, it should be protected from ambient condition by dielectrics; the chemical deterioration of Ag nanoparticle has been a critical problem in plasmonic research field. I established the reproducible way to fabricate Ag/Co nanomatch structure embedded in TiO_2 film by pulsed laser deposition (PLD) method. It was clarified that the structure of Ag/Co nanostructures can be controlled by the PLD condition and the characteristic Ag/Co nanomatch structures appeared only at a specific condition (of composition and substrate temperature), where Co plays an important role in defining the two dimensional positions at which Ag nanorods segregate. The Ag nanostructure changed from rod-like to spherical and the size became larger, as the Ag content of PLD target increased. Ag-Co-TiO_2 films showed a broad absorption peak, which was confirmed to be localized surface plasmon resonance (LSPR) peak of Ag nanostructure, by finite-difference time-domain (FDTD) calculation. The LSPR peak systematically shifted to longer wavelengths with increasing the Ag content of PLD target.

Then I proposed the Ag-Co-TiO_2 nanocomposite film with characteristic Ag/Co nanomatch structures embedded in TiO_2 matrix as a promising electrode material. Since the Ag nanostructure was firmly protected by TiO_2 matrix, the Ag

nanostructure can be preserved for a long time being beneficial to shipping, and can be washed. Moreover I found that the Ag nanostructure was electrochemically unsealed, whenever the fresh Ag surface is needed. I indeed made the Ag nanostructures contact with the supporting electrolyte, and subsequently observed photocurrent enhanced by plasmon resonance of Ag nanorods; Ag nanostructure which can be sealed and unsealed like canned goods was developed here for the first time. This Ag-Co-TiO_2 nanocomposite film would be useful in various applications, including not only photoelectric conversion but also photocatalysis and plasmonic sensor such as SERS, where fresh Ag surface improves the properties.

I hope that this work will be helpful to realize these applications utilizing the metal nanocomposite films with protecting Ag nanostructures in the future.

References

A

[J. T. Abiade, 2008] J. T. Abiade, G. X. Miao, A. Gupta, A. A. Gapud, and D. Kumer, *Thin Solid Films*, **516**, 2082 (2008).

[A. V. Alekseeva, 2006] A. V. Alekseeva, V. A. Bogatyrev, B. N. Khlebtsov, A. G. Mel'nikov, L. A. Dykman, and N. G. Khlebtsov, *Colloid Journal*, **68**, 661 (2006).

[M. G. Albrecht, 1977] M. G. Albrecht and J. A. Creighton, *J. Am. Chem. Soc.*, **99**, 5215 (1977).

[R. A. Alvarez-Puebla, 2012] R. A. Alvarez-Puebla, E. R. Zubarev, N. A. Kotov, L. M. Liz-Marzán, *Nano Today*, **7**, 6 (2012).

[K. Artmann, 1942] K. Artmann, *Z. Physik.*, **119**, 529 (1942).

[H. A. Atwater, 2010] H. A. Atwater and A. Polman, *Nat. Mater.*, **9**, 205 (2010).

[K. Awazu, 2008] K. Awazu, M. Fujimaki, C. Rockstuhl, J. Tominaga, H. Murakami, Y. Ohki, N. Yoshida, and T. Watanabe, *J. Am. Chem. Soc.*, **130**, 1676 (2008).

[K. Awazu, 2009] K. Awazu, X. Wang, M. Fujimaki, J. Tominaga, S. Fujii, H. Aiba, Y. Ohki, and T. Komatsubara, *Nucl. Instrum. Methods. Phys. Res. B.*, **267**, 941 (2009).

B

[N. Bahlawane, 2011] N. Bahlawane, K. Kohse-Höinghaus, T. Weimann, P. Hinze, S. Röhe, M. Bäumer, *Angew. Chem.,* **50**, 1 (2011).

[M. L. Balmer, 1995] M. L. Balmer, F. F. Lange, V. Jayaram, and C. G. Levi, *J. Am. Ceram. Soc.*, **78**, 1489 (1995).

[L. L. Beecroft, 1997a] L. L. Beecroft and C. K. Ober, *Chem. Mater.*, **9**, 1302 (1997).

[L. L. Beecroft, 1997b] L. L. Beecroft and C. K. Ober, J. Macromol. *Sci.-Pure Appl. Chem.*, **A34**, 573 (1997).

[J. I. Beltran, 2003] J. I. Beltran, S. Gallego, J. Cerda, J. S. Moya, M. C. Muñoz, *Phys. Rev. B.*, **68**, 075401 (2003).

[J. I. Beltran, 2004] J. I. Beltran, S. Gallego, J. Cerda, J. S. Moya, M. C. Muñoz, J. *Phys. Chem. B.*, **108**,15432 (2004).

[H. A. Bethe, 1944] H. A. Bethe, *Phys. Rev.***, 66**, 163 (1944).

[G. Binning, 1982] G. Binning, H. Rohrer, *Helv. Phys. Acta*., **55**, 726 (1982).
[C. F. Bohren, 1983] C. F. Bohren and D. R. Huffman, *Absorption and Scattering of Light by Small Particles*, John Wiley & Sons, Inc., New York (1983).
[S. I. Bozhevonyi, 2006] S. I. Bozhevonyi, V. S. Volkov, E. Devaux, J. Y. Laluet, and T. W. Ebbesen, *Nature*, **440**, 508 (2006).
[F. Brouers, 1993] F. Brouers, J. P. Clerc, G. Giraud, J. M. Laugier, Z. A. Randriamantany, *Phys. Rev. B.*, **47**, 666 (1993).
[D. K. Burge, 1969] D. K. Burge, J. M. Bennett, R. L. Peck, and H. E. Bennett, *Surf. Sci.*, **16**, 303 (1969).
[D. Buso, 2009] D. Buso, L. Palmer, V. Bello, G. Mattei, M. Post, P. Mulvaney, and A. Martucci, *J. Mater. Chem.*, **19**, 2051 (2009).

C

[G. Carotenuto, 2000] G. Carotenuto, G. P. Pepe, and L. Nicolais, *Eur. Phys. J. B.*, **16**, 11 (2000).
[A. Castelo, 2012] A. Castelo, C. N. Afonso, E. Pesce, and E. Piscopiello, *Nanotechnology*, **23**, 105603 (2012).
[E. Céspedes, 2010] E. Céspedes, D. Babonneau, O. Lyon, J. Sánchez-Marcos, S. Rouzière, C. Prieto, L. Olivi, and A. Traverse, *J. Appl. Phys.*, **107**, 104306 (2010).
[G. H. Chan, 2007] G. H. Chan, J. Zhao, E. M. Hicks, G. C. Schatz, and R. P. Van Duyne, *Nano Lett.*, **7**, 1947 (2007).
[G. S. Chang, 2006] G. S. Chang, E. Z. Kurmaev, D. W. Boukhvalov, L. D. Finkelstein, D. H. Kim, T. W. Noh, A. Moewes, and T. A. Callcott, *J. Phys. Condens. Matter*, **18**, 4243 (2006).
[K. L. Chavez, 2001] K. L.Chavez, D. W. Hess, *J. Electrochem. Soc.*, **148**, G640 (2001).
[H. Chen, 2014] H. Chen, Z. Wei, K. Yan, Y. Bai, and S. Yang, *J. Phys. Chem. Lett.*, **5**, 2890 (2014).
[J. R. Cole, 2006] J. R. Cole and N. J. Halas, *Appl. Phys. Lett.*, **89**, 153120 (2006).

D

[M. C. Daniel, 2004] M. C. Daniel and D. Astruc, *Chem. Rev.*, **104**, 293 (2004).

E

[T. W. Ebbesen, 1998] T. W. Ebbesen, H. J. Lezec, H. F. Ghaemi, T. Thio, and P. A. Wolff, *Nature*, **391**, 667 (1998).

[EERE, 2011] "2010 Solar Technologies Market Report, November 2011, Energy Efficiency & Renewable Energy", U.S. Department of ENERGY (2011).

F

[W. G. Fahrenholtz, 2000] W. G. Fahrenholtz, D. T. Ellerby, R. E. Loehman, *J. Am. Ceram. Soc.*, **83**, 1279 (2000).

[Y. Fang, 2008] Y. Fang, N. H. Seong, and D. D. Dlott, *Science,* **321**, 388 (2008).

[U. Fano, 1938] U. Fano, *Ann. Phys.*, **32**, 393 (1938).

[V. E. Ferry, 2008] V. E. Ferry, L. A. Sweatlock, D. Pacifici, and H. A. Atwater, *Nano Lett.*, **8**, 4391 (2008).

[U. C. Fischer, 1989] U. C. Fischer and D. W. Pohl, *Phys. Rev. Lett.*, **62**, 458 (1989).

[M. Fleischmann, 1974] M. Fleischmann, P. J. Hendra, A. J. McQuilla, *Chem. Phys. Lett.*, **26**, 163 (1974).

[D. Fromm, 2004] D. P. Fromm, A. Sundaramurthy, P. J. Schuck, G. Kino, and W. E. Moerner, *Nano. Lett.*, **4**, 957 (2004).

[T. Fukumura, 2001] T. Fukumura, Z. Jin, M. Kawasaki, T. Shono, T. Hasegawa, S. Koshihara, and H. Koinuma, *Appl. Phys. Lett.*, **78**, 958 (2001).

[M. Fujimaki, 2007] M. Fujimaki, Y. Iwanabe, C. Rockstuhl, X. Wang, K. Awazu, and J. Tominaga, *J. J. Appl. Phys.*, **46**, L1080 (2007).

[A. Fujishima, 1972] A. Fujishima and K. Honda, *Nature*, **238**, 37 (1972).

G

[M. Garcia del Muro, 2008] M. Garcia del Muro, Z. Konstantinovic, M. Varela, X. Batlle, and A. Labarta, *J. Nanomat.*, 475168 (2008).

[F. F. Ge, 2010] F. F. Ge, X. M. Wang, L. H. Cao, J. Li, H. L. Zhang, H. P. Wang,Y. Dai, H. B. Wang, J. Shen, and W. D. Wu, *Nanoscale. Res. Lett.*, **5**, 834

(2010).
[N. G. Gleeneltch, 2012] N. G. Greeneltch, A. S. Davis, N. A. Valley, F. Casadio, G. C. Schatz, R. P. Van Duyne, and N. C. Shah, *J. Phys. Chem. A.*, **116**, 11863 (2012).
[S. C. B. Gopinath, 2013] S. C. B. Gopinath, K. Awazu, M. Fujimaki, K. Shimizu, T. Shima, *Plos One*, **8**, e69121 (2013).
[T. E. Graedel, 1985] T. E. Graedel, J. P. Franey, G. J. Gaultieri, G. W. Kammolott, D. L. Malm, *Corros. Sci.*, **25**, 1163 (1985).
[T. E. Graedel, 1992] T. E. Graedel, *J. Electrochem. Soc.*, **139**, 1963 (1992).
[M. Gratzel, 2005] M. Gratzel, *Inorg. Chem.*, **44**, 6841 (2005).
[M. A. Green, 1993-2014] M. A. Green, K. Emery *et al*, *Prog. Photovol. Res.*, "Solar cell Efficiency Tables (Version 1-44)" (1993-2014).
[M. A. Green, 2010] M. A. Green, *Prog. Photovolt: Res. Appl.*, **19**, 473 (2010).

H
[C. L. Haynes, 2003] C. L. Haynes and R. P. Van Duyne, *J. Phys. Chem. B.*, **107**, 7426 (2003).
[A. J. Haes, 2004] A. J. Haes, S. Zou, G. C. Schatz, and R. P. Van Duyne, J. *Phys. Chem. B.*, **108**, 6961 (2004).
[N. Hagura, 2010] N. Hagura, W. Widiyastuti, F. Iskandar, K. Okuyama, *Chemical Engineering Journal*, **156**, 200 (2010).
[Y. Hamanaka, 2004] Y. Hamanaka, A. Nakamura, L. M. Liz-Marzan, P. Mulvaney, *Appl. Phys. Lett.*, **84**, 4938 (2004).
[Y. Han, 2011] Y. Han, R. Lupitskyy, T. M. Chou, C. M. Stafford, H. Du, and S. Sukhishvili, *Anal. Chem.*, **83**, 5873 (2011).
[F. Hao, 2007] F. Hao, C. L. Nehl, J. H. Hafner, and P. Nordlander, *Nano Lett.*, **7**, 729 (2007).
[S. Haruta, 2011] S. Haruta, H. Misawa, K. Ueno, Y. Yokota, H. Uehara, H. Hiratsuka, H. Horiuchi, T. Okutsu, *J. Photochem. Photobiol. A.*, **221**, 268 (2011).
[C. L. Haynes, 2001] C. L. Haynes and R. P. Van Duyne, *J. Phys. Chem. B.*, **105**, 5599 (2001).
[A. Hessel, 1965] A. Hessel and A. A. Oliner, *Appl. Opt.*, **4**, 1275 (1965).
[M. Hillenkamp, 2007] M. Hillenkamp, G. D. Domenicantonio, O. Eugster, and C.

Félix, *Nanotechnology*, **18**, 015702 (2007).
[E. F. Hillinski, 1988] E. F. Hillinski, P. A. Lucas, Y. Wang, *J. Chem. Phys.*, **89**, 3435 (1988).
[G. Hodes, 2012] G. Hodes, *J. Phys. Chem. Lett.*, **3**,1208 (2012).
[M. P. Horvath, 1992] M. P. Horvath and L. Takacs, *IEEE Trans. Magn.*, **28**, 3186 (1992).

I

[M. Ihara, 2010] M. Ihara, M. Kanno, S. Inoue, *Physica. E.*, **42**, 2867 (2010).
[K. Ikemiya, 2011] K. Ikemiya, Y. Hirose, and T. Hasegawa, *J. Phys. Chem. C.*, **115**., 1776 (2011).
[K. Ikemiya, 2014] K. Ikemiya, K. Konishi, E. Fujii, T. Kogure, M. Kuwata-Gonokami, and T. Hasegawa, *Opt. Mat. Exp.*, **4**, 1564 (2014).
[H. Im, 2011] H. Im, S. H. Lee, N. J. Wittenberg, T. W. Johnson, N. C. Lindquist, P. Nagpal, D. J. Norris, and S. H. Oh, *ACS Nano*, **8**, 6244 (2011).
[D. B. Ingram, 2011] D. B. Ingram and S. Linic, *J. Am. Chem. Soc.*, **133**, 5202 (2011).
[H. Inouye, 1998] H. Inouye, K. Tanaka, I. Tanahashi, and K. Hirao, *Phys. Rev. B.*, **57**, 11334 (1998).
[Y. Inouye, 1994] Y. Inouye, S. Kawata, *Opt. Lett.,* **19**, 159 (1994).
[D. Iuşan, 2009] D. Iuşan, M. Kabir, O. Grånäs, O. Eriksson, and B. Sanyal, *Phys. Rev. B.*, **79**, 125202 (2009).

J

[J. D. Jackson, 1999] J. D. Jackson, *Classical Electrodynamics.* John Wiley & Sons, Inc., New York (1999).
[D. L. Jeanmaire, 1977] D. L. Jeanmaire and R. P. Van Duyne, *J. Electroanal. Chem.,* **84**, 1 (1977).
[Y. J. Jen, 2014] Y. J. Jen, M. J. Lin, Y. F. Chau, and C. Y. Jheng, *Thin Solid Films*, **567**, 38 (2014).
[JEOL HP] http://www.jeol.co.jp/en/science/sem.html
[Z. Jin, 2003] Z. Jin, Y. Z. Yoo, T. Sekiguchi, T. Chikyow, H. Ofuchi, H. Fujioka, M. Oshima, and H. Koinuma, *Appl. Phys. Lett.*, **83**, 39 (2009).

K

[M. Kagawa, 1984] M. Kagawa, Y. Imamura, S. Usui, and Y. Shono, *J. Mat. Sci. Lett.*, **3**, 699 (1984).

[M. Kanehara, 2009] M. Kanehara, H. Koike, T. Yoshonaga, and T. Teranishi, *J. Am. Chem. Soc.*, **131**, 17736 (2009).

[K. L. Kelly, 2003] K. L. Kelly, E. Coronado, L. L. Zhao, G. C.Schatz, *J. Phys. Chem. B.*, **107**, 668 (2003).

[C. H. Kim, 2011] C. H. Kim, S. H. Cha, S. C. Kim, M. Song, J. Lee, W. S. Shin, S. J. Moon, J. H. Bahng, N. A. Kotov, and S. H. Jin, *ACS Nano*, **4**, 3319 (2011).

[D. H. Kim, 2002] D. H. Kim, J. S. Yang, K. W. Lee, S. D. Bu, T. W. Noh, S. J. Oh, Y. W. Kim, J. S. Chung, H. Tanaka, H. Y. Lee, and T. Kawai, *Appl. Phys. Lett.*, **81**, 2421 (2002).

[F. Kim, 2002] F. Kim, J. H. Song, and P. Yang, *J. Am. Chem. Soc*., **124**, 14316 (2002).

[S. Kim, 2008] S. Kim, J. Jin, Y. J. Kim, I. Y. Park, Y. Kim, and S. W. Kim, *Nature*, **453**, 757 (2008).

[C. Kittel, 1976] C. Kittel, *Introduction to Solid State Physics*, Wiley, New York (1976).

[P. Kluth, 2006] P. Kluth, B. Johannessen, G. J. Foran, D. J. Cookson, S. M. Kluth, and M. C. Ridgway, *Phys. Rev. B*., **74,** 014202 (2006).

[K. Kneipp, 1997] K. Kneipp, Y. Wang, H. Kneipp, L. T. Perelman, I. Itzkan, R. R. Dasari, and M. S. Feld, *Phys. Rev. Lett.*, **78**, 1667 (1997).

[M. Kobiyama, 2003] M. Kobiyama, *The basic theory of optical films –Fresnel coefficient, Herpin matrix-*, Optronics Co. Ltd., Tokyo, 2003 (Chapter 5.2.2).

[V. G. Kravets, 2014] V. G. Kravets, R. Jalil, Y. J. Kim, D. Ansell, D. E. Aznakayeva, B. Thackray, L. Britnell, B. D. Belle, F. Withers, I. P. Radko, Z. Han, S. I. Bozhevolnyi, K. S. Novoselov, A. K. Geim & A. N. Grigorenko, *Scientific Reports*, **4**, 5517 (2014).

[U. Kreibig, 1995] U. Kreibig and M. Vollmer, *Optical Properties of Metal Clusters*, Springer-Verlag, (1995).

[E. Kretchmann, 1968] E. Kretchmann and H. Raether, *Z. Naturfors.*, **23a**, 2135 (1968) Fig. 1.

[E. Kretschmann, 1971] E. Kretschmann, Z. *Physik.*, **241**, 313 (1971).

[J. T. Krug, 1999] J. T. Krug II, G. D. Wang , S. R. Emory , and S. Nie, *J. Am. Chem. Soc.*, **121**, 9208 (1999).
[S. Kühn, 2006] S. Kühn, U. Håkanson, L. Rogobete, and V. Sandoghdar, *Phys. Rev. Lett.*, **97**, 017402 (2006).
[A. P. Kulkarni, 2010] A. P. Kulkarni, K. M. Noone, K. Munechika, S. R. Guyer, and D. S. Ginger, *Nano Lett.*, **10**, 1501 (2010).
[M. K. Kumar, 2011] M. K. Kumar, S. Krishnamoorthy, L. K. Tan, S. Y. Chiam, S. Tripathy, and H. Gao, *ACS Catal.*, **1**, 300 (2011).

L

[K. S. Lee, 2006] K. S. Lee, and M. A. El-Sayed, *J. Phys. Chem. B.*, **110**, 19220 (2006).
[I. Levin, 2006] I. Levin, J. Li, J. Slutsker, and A. L. Roytburd, *Adv. Mater.*, **18**, 2044 (2006).
[T. Li, 2013] T. Li, R. Larciprete, S. Turchini, N. Zema, A. Bonanni, and A. D. Trolio, *J. Phys. Chem. C.*, **117**, 687 (2013).
[H. Lin, 2012] H. Lin, S. P. Centeno, L. Su, B. Kenens, S. Rocha, M. Sliwa, J. Hofkens, and H. Uji-I, *Chem. Phys. Chem.*, **13**, 973 (2012).
[S. Link, 1999] S. Link, Z. L. Wang, and M. A. El-Sayed, *J. Phys. Chem. B.*, **103**, 3529 (1999).
[S. Link, 2011] P. Christopher, D. B. Ingram, S. Linic, *J. Phys. Chem. C*., **19**, 9173 (2010).
[B. A. Lippmann, 1954] B. A. Lippmann and A. Oppenheim, *Tech. Res. Group N. Y.* (1954).
[N. Liu, 2011] N. Liu, M. Hentschel, T. Weiss, A. Alivisatos, and H. Giessen, *Science*, **17**, 1407 (2011).
[D. H. Lowndes, 2006] D. H. Lowndes, D. B. Geohegan, A. A. Puretzky, D. P. Norton, and C. M. Rouleau, *Science*, **273**, 898 (1996).
[L. Lu, 2006] L. Lu, A. Kobayashi, K. Tawa, and Y. Ozaki, *Chem. Mater.*, **18**, 4894 (2006).
[X. Luo, 2004] X. G. Luo and T. T. Ishihara, *Appl. Phys. Lett.*, **84**, 4780 (2004).
[J.J. Mock, 2003] J. J. Mock, D. R. Smith, and S. Schultz, *Nano. Lett.*, **3**, 485 (2003).

[J. M. Luther, 2011] J. M. Luther, P. K. Jain, T. Ewers, and A. P. Alivisatos, *Nat. Mater.*, **10**, 361 (2011).

M

[M. D. Macmahon, 2005] M. D. Macmahon, R. Lopez, H. M. Mayer III, L. C. Feldman, R. F. Huglund Jr., *Appl. Phys. B.*, **80**, 915 (2005).

[M. D. Malinski] M. D. Malinsky, K. L. Kelly, G. C. Schatz, R. P. Van Duyne, *J. Am. Chem. Soc.*, **123**, 1471 (2001).

[P. B. Malla, 1991] P. B. Malla, P. R. Ravindranathan, S. Komarneni, and R. Roy, *Nature*, **351**, 555 (1991).

[S. A. Maier, 2007] S. A. Maier, *Plasmonics*, Springer, New York (2007).

[G. Manickam, 2012] G. Manickam, R. K. Vijayaraghavan, L. Kerr, C. Doyle, D. E. Williams, S. Daniels, *Analyst.*, **137**, 5265 (2012).

[D. Manikandan, 2003] D. Manikandan, S. Mohan, P. Magudapathy, K. G. M. Nair, *Physica B-Cond. Mater.*, **325**, 86 (2003).

[J. Margueritat, 2006] J. Margueritat, J. Gonzalo, C. N. Afonso, M. I. Ortiz, and C. Ballesteros, *Appl. Phys. Lett.*, **88**, 093107 (2006).

[J. Margueritat, 2007] J. Margueritat, J. Gonzalo, C. N. Afonso, G. Bachelier, A. Mlayah, A. S. Laarakker, D. B. Murray, and L. Saviot, *Appl. Phys. A.,* **89**, 369 (2007).

[P. Matheu, 2008] P. Matheu, S. H. Lim, S. Serkacs, C. McPheeters, and E. T. Yu, *Appl. Phys. Lett.*, **93**, 113108 (2008).

[L. Maya, 1996] L. Maya, M. Paranthaman, T. Thundat, ML. Bauer, *J. Vac. Sci. Tech*, **14**, 15 (1996).

[G. M. McClelland, 1987] G. M. McClelland, R. Erlandsson, and S. Chiang, *Rev. Prog. in Quant. Nondestr. Eval.*, **6A**, 1307 (1987).

[D. Meissner, 1983] D. Meissner, R. Memming, and B. Kastening, *Chem. Phys. Lett.*, **96**, 34 (1983).

[G. Mie, 1908] G. Mie, *Ann. de Phys.*, **25**, 377 (1908).

[A. Morales-Rodríguez, 2003] A. Morales-Rodríguez, A. Bravo-Leon, A. Domínguez-Rodríguez, S. Lopez-Esteban, J. S. Moya, M. Jiménez-Melendo, *J. Eur. Ceram. Soc.*, **23,** 2849 (2003).

[J. S. Moya, 2007] J. S. Moya, S. Lopez-Esteban, and C. pecharroman,

Progress in Materials Science, **52**, 1017 (2007).

N

[H. Nabika, 2010] H. Nabika, M. Takase, F. Nagasawa, and K. Murakoshi, *J. Phys. Chem. Lett.*, **1**, 2470 (2010).

[K. Naoi, 2004] K. Naoi, Y. Ohko, T. Tatsuma, *J.Am.Chem.Soc.*, **126**, 3664 (2004).

[S. Nie, 1997] S. Nie and S. R. Emory, *Science*, **275**, 1102 (1997).

[Y. Nishijima, 2010] Y. Nishijima, K. Ueno, Y. Yokota, K. Murakoshi, H. Misawa, *J. Phys. Chem. Lett.* **1**, 2031 (2010).

[Y. Nishijima, 2012] Y. Nishijima, K. Ueno, Y. Kotake, K. Murakoshi, H. Inoue, and H. Misawa, *J. Phys. Chem. Lett.*, **3**, 1248 (2012).

[H. Nogawa, 2010] H. Nogawa, A. Chikamatsu, Y. Hirose, S. Nakao, H. Kumigashira, M. Oshima, T. Hasegawa, *J. Phys. D: Appl. Phys.*, **44**, 365404 (2011).

[P. Nordlander, 2004] P. Nordlander, C. Oubre, E. Prodan, K. Li and Stockman, *Nano Lett.*, **4**, 899 (2004).

[C. Novo, 2008] C. Novo, A. M. Funston, I. Pastoriza-Santos, L. M. Liz-Marzán, P. Mulvaney, *J. Phys. Chem. C.*, **112**, 3 (2008).

[C. Nylander, 1982] C. Nylander, B. Liedberg, and T. Lind, *Sensors and Actuators*, **3**, 79 (1982/83).

O

[T. W. H. Oates, 2013] T. W. H. Oates, M. L. Losurdo, S. Noda, K. Hinrichs, *J. Phys. D: Appl.Phys.*, **46**, 145308 (2013).

[K. Okamoto, 2013] K. Okamoto, B. Lin, K. Imazu, A. Yoshida, K. Toma, M. Toma, and K. Tamada, *Plasmonics*, **8**, 581 (2013).

[T. Okamoto, 2010] T. Okamoto and K. Kajikawa, *Plasmonics*, Kodansha, Tokyo (2010).

[T. Okamoto, 2004] T. Okamoto, F. H'Dhili, and S. Kawata, *Appl. Phys. Lett.*, **85**, 3968 (2004).

[M. M. Oliveira, 2005] M. M. Oliveira, D. Ugarte, D. Zanchet, AJG. Zarbin, J J. *Colloid. Interf. Sci.*, **292**, 429 (2005).

[A. Otto, 1968] A. Otto, Z. *Physik.*, **216**, 398 (1968).
[C. Oubre, 2004] C. Oubre and P. Nordlander, *J. Phys. Chem. B.*, **108**, 17740 (2004).

P

[A. B. Pakhomov, 1995] A. B. Pakhomov, X. Yan, B. Zhao, *Appl. Phys. Lett.*, **67**, 3497 (1995).
[C. H. Palmer, 1961] C. H. Palmer, Jr., *J. Opt. Soc. Am.*, **51**, 1438 (1961).
[B. Palpant, 1998] B. Palpant, B. Prevel, J. Lerme, E. Cottancin, M. Pellarin, M. Treilleux, A. Perez, J. L. Vialle, and M. Broyer, *Phys. Rev. B.*, **57**, 1963 (1998).
[S. Pillai, 2010] S. Pillai and M. A. Green, *Sol. Energy Mater. Sol. Cells.*, **9**, 205 (2010).
[R. J. Peráez, 2013] R. J. Peráez, A. Castelo, C. N. Afonso, A. Borrás, J. P. Espinós, S. Riedel, P. Leiderer, and J. Boneberg, *Nanotechnology*, **24**, 365702 (2013).
[D. Pines, 1952] D. Pines and D. Bohm, *Phys. Rev.*, **85**, 338 (1952).
[D. Pines, 1956] D. Pines, *Rev. Mod, Phys.*, **28**, 184 (1956).
[S. Pisov, 2008] S. Pisov, O. Melikhova, and M. Hou, *Comput. Phys. Commun.,* **179,** 102 (2008).
[M. Pourbaix, 1974] M. Pourbaix, *Atlas of elactrochemical equilibria in aqueous solutions*, National Association of Corrosion Engineers, Section 12.2, Section 14.2, (1974).
[E. Prodan, 2003] E. Prodan, P. Nordlander, and N. J. Halas, *Nano Lett*., **3**, 1411 (2003).
[E. M. Purcell, 1973] E. M. Purcell, and C. R. Pennypacker, *Astrophys. J.*, **186**, 705 (1973).

R

[B. P. Rand, 2004] B. P. Rand, P. Peumans, and S. R. Forrest, *J. Appl. Phys.*, **96**, 7519 (2004).
[O. M. Rayleigh, 1907] O. M. Rayleigh, *Proc. Roy. Soc. A.* (London), **79**, 399 (1907).
[V. Resta, 2009] V. Resta, C. N. Afonso, E. Piscopiello, and G. Van Tendeloo,

Phys. Rev. B., **79**, 235409 (2009).
[R. H. Ritchie, 1957] R. H. Ritchie, *Phys. Rev.*, **106**, 874 (1957).
[C. Rockstuhl, 2008] C. Rockstuhl, S. Fahr, and F. Ledrer, *J. Appl. Phys.*, **104**, 123102 (2008).

S

[R. Sachan, 2012] R. Sachan, S. Yadavali, N. Shirato, H. Krishna, V. Ramos, G. Duscher, S. J. Pennycook, A. K. Gangopadhyay, H. Garcia**,** and R Kalyanaraman**,** *Nanotechnology*, **23**, 275604 (2012).
[H. Sang, 1995] H. Sang, S. Y. Zhang, H. Chen, G. Ni, J. M. Hong, X. N. Zhao, Z. S. Jiang, and Y. W. Du, *Appl. Phys. Lett*., **67**, 2017 (1995).
[B. Sanyal, 2008] B. Sanyal, R. Knut, O. Grånäs, D. M. Iuşan, O. Karis, and O. Eriksson, *J. Appl. Phys.*, **103**, 07D130 (2008).
[D. Sarid, 2010] D. Sarid and W. Challener, *Modern Introduction to Surface Plasmons, Theory, Mathematica, and Applications*, Cambridge University Press, New York (2010).
[G. Sauer, 2005] G. Sauer, G. Brehm, S. Schneider, H. Graener, G. Seifert, K. Nielsch, J. Choi, P. Göring, U. Gösele, P. Miclea, and R. B. Wehrspohn, *J. Appl. Phys.*, **97**, 024308 (2005).
[D. M. Schaadt, 2005] D. M. Schaadt, B. Feng. And E. T. Yu, *Appl. Phys.Lett.*, **86**, 063106 (2005).
[J. A. Schuller, 2010] J. A. Schuller, E. S. Barnard, W. Cai, Y. C. Jun, J. S. White, and M. L. Brongersma, *Nat. Mater.*, **9**, 193 (2010).
[J. S. Sekhon, 2011] J. S. Sekhon, and S. S. Verma, *Plasmonics*, **6**, 311 (2011).
[R. L. Seliger, 1979] R. L. Seliger, J. W. Ward, V. Wang, and R. L. Kubena, *Appl. Phys. Lett.*, **34**, 310 (1979).
[R. Seoudi, 2011] R. Seoudi, A. Shabaka, Z. A. El Sayed, and B. Anis, *Physica E.*, **44**, 440 (2011).
[R. Serna, 2001] R. Serna, J. Gonzaro, A. Suárez-Gracía, C. N. Afonso, J. P. Barnes, A. K. Petford-Long, R. C. Doole, and D. Hole, *J. Microscopy.*, **201**, 250 (2001).
[K. Setoura, 2012] K. Setoura, D. Werner, and S. Hashimoto, *J. Phys. Chem. C.*, **116**, 15458 (2012).

[R. Serna, 1999] R. Serna, C. N. Afonso, J. M. Ballesteros, A. Naudon, D. Babonneau, and A. K. Petford-Long, *Appl. Surf. Sci.*, **138**, 1 (1999).
[X. She, 2004] X. She and M. J. Flytzani-Stephanopoulos, *Catal*., **237**, 79 (2006).
[W. Shi, 2006] W. Shi, H. Zeng, Y. Sahoo, T. Y. Ohulchanskyy, Y. Ding, Z. L. Wang, M. Swihart, and P. N. Prasad, *Nano Lett.*, **6**, 875 (2006).
[A. S. B. Sombra, 1992] A. S. B. Sombra, *Solid State Commun.*, **82**, 805 (1992).
[C. Sönnichsen, 2002] C. Sönnichsen, T. Franzl, T. Wilk, G. von Plessen, J. Feldmann, O. Wilson and P. Mulvaney, *Phys. Rev. Lett.*, **88**, 077402 (2002).
[W. Srituravanich, 2005] W. Srituravanich, S. Durant, H. Lee, C. Sun, and X. Zhang, *J. Vac. Sci. Technol., B.*, **23**, 2636 (2005).
[S. D. Stadridge, 2009] S. D. Standridge, G. C. Shatz, and J. T. Hupp, *J. Am. Chem. Soc.*, **131**, 8407 (2009).
[S. Szunerits, 2008] S. Szunerits, X. Castel, R. Boukherroub, *J. Phys. Chem. C*., **112**, 15813 (2008).

T

[T. Takahashi, 2013] T. Takahashi, A. Kudo, S. Kuwabata, A. Ishikawa, H. Ishihara, Y. Tsuboi, and T. Torimoto, *J. Phys. Chem. C.*, **117**, 2511 (2013).
[H. Takele, 2006] H. Takele, H. Greve, C. Pochstein, V. Zaporojtchenko, F. Faupel, *Nanotechnology*, **17**, 3499 (2006).
[I. Tanahashi, 2007] I. Tanahashi, *Bull. Chem. Soc. Jpn.*, **80**, 2019 (2007).
[S. Tanemura, 2003] S. Tanemura, L. Miao, P. Jin, K. Kaneko, A. Terai, and N. Nabatova-Gabain, *Appl. Surf. Sci.*, **212-213**, 654 (2003).
[Y. Tian, 2004] Y. Tian, T. Tatsuma, *Chem. Commun*., **16**, 1810 (2004).
[Y. Tian, 2005] Y. Tian and T. Tatsuma, *J. Am. Chem. Soc.*, **127**, 7632 (2005).
[F. J. Tsai, 2010] F. J. Tsai, J. Y. Wang, J. J. Huang, Y. W. Kiang, and C. C. Yang, *Opt. Exp.*, **18**, A207 (2010).
[A. E. Tselev, 1999] A. E. Tselev, N. I. Polushkin, Y. K. Verevkin, A. A, Gorbunov, V. N. Petryakov, and W. Pompe, *Appl. Phys. A.*, **69**, S819 (1999).
[W. H, Tuan, 1995] W. H. Tuan, H. H. Wu, T. J. Yang, *J. Mater. Sci.*, **30**, 855 (1995).

U

[K. Ueda, 2001] K. Ueda, H. Tabata, and T. Kawai, *Appl. Phys. Lett.*, **79**, 988 (2001).

[K. Ueno, 2005] K. Ueno, V. Mizeikis, S. Juodkazis, K. Sasaki, and H. Misawa, *Opt. Lett.*, **30**, 2158 (2005).

[K. Ueno, 2006] K. Ueno, S. Juodkazis, V. Mizeikis, K. Sasaki, H. Misawa, *J. Am. Chem. Soc.*, **128**, 14226 (2006).

[K. Ueno, 2008] K. Ueno, S. Juodkazis, T. Shibuya, Y. Yokota, V. Mizeikis, K. Sasaki, H. Misawa, *J. Am. Chem. Soc.*, **130**, 6928 (2008).

[K. Ueno, 2013] K. Ueno, H. Misawa, *J. Photochem. Photobiol. C.*, **15**, 31 (2013).

[T. Ung, 2001] T. Ung, L. M. Liz-Marzán, and P. Mulvaney, *J. Phys. Chem.*, 105, 3441 (2001).

V

[R. P. Van Duyne, 1993] R. P. Van Duyne, J. C. Hulteen, and D. A. Treichel, *J. Chem. Phys.*, **99**, 2101 (1993).

W

[L. Wang, 2011] L. Wang, W. Xiong, Y. Nishijima, Y. Yokota, K. Ueno, H. Misawa, G. Bi, J. R. Qiu, *Optics Express*., **19**, 10640 (2011).

[Q. Wang, 2004] Q. Wang, Q. Sun, B. K. Rao, and P. Jena, *Phys. Rev. B.*, **69**, 233310 (2004).

[Q. Wang, 2004] Q. Wang, Z. T. Song, W. L. Liu, C. L. Lin, and T. H. Wang, *Appl. Surf. Sci.*, **230**, 8 (2004).

[Y. Wang, 1990] Y. Wang, A. Suna, J. McHugh, E. F. Hillinski, P. A. Lucas, R. D. Johnson, *J. Chem. Phys.*, **92**, 6927 (1990).

[A. Watanabe, 2014a] A. Watanabe, K. Ikemiya, A. Chikamatsu, Y. Hirose, and T. Hasegawa, *Chem. Lett.*, **43**, 225 (2014).

[A. Watanabe, 2014b] A. Watanabe, Y. Kotake, Y. Kamata, A. Chikamatsu, K. Ueno, H. Misawa, and T. Hasegawa, *J. Phys. Chem. Lett.*, **5**, 25 (2014).

[M. Westphalen, 2000] M. Westphalen, U. Kreibig, J. Rostalski, H. Luth, and D. Meissner, *Sol. Energy Mater. Sol. Cells.*, **61**, 97 (2000).

[K. A. Willets, 2006] K. A. Willets and R. P. Van Duyne, *Annu. Rev. Phys. Chem.*, **58**, 267 (2006).
[R. W. Wood, 1902] R. W. Wood, *Phil. Mag.*, **4**, 396 (1902).

X
[M. Xu, 2011] M. Xu, Y. Gao, E. M. Moreno, M. Kunst, M. Muhler, Y. Wang, H. Idriss, and C. Wöll, *Phys. Rev. Lett.*, **106**, 138302 (2011).

Y
[S. C. Yang, 2010] S. C. Yang, H. Kobori, C. L. He, M. H. Lin, H. Y. Chen, C. Li, M. Kanehara, T. Teranishi, and S. Gwo, *Nano Lett.*, **10**, 632 (2010).
[K. S. Yee, 1966] K. S. Yee, *IEEE Trans. Anttenas Propagat.*, **14**, 302 (1966).
[W. J. Yoon, 2010] W. J. Yoon, K. Y. Jung, J. W. Liu, T. Duraisamy, R. Revur, F. L. Teixeira, S. Sengupta, and P. R. Berger, *Sol. Energy Mater.*, **94**, 128 (2010).
[J. Yu, 2009] J. G. Yu, G. P. Dai, and B. B. Huang, *J. Phys. Chem. C.*, **113**, 16394 (2009).

Z
[E. J. Zeman, 1987] E. J. Zeman and G. C. Schartz, *J. Phys. Chem.*, **91**, 634 (1987).
[J. Zhang, 2007] J. Zhang, Y. Fu, M. H. Chowdhury, and J. R. Lakowicz, *Nano Lett.*, **7**, 2101 (2007).
[F. Zhou, 2008] F. Zhou, Z. Y. Li, and Y. Liu, *J. Phys. Chem. C.*, **112**, 20233 (2008).
[X. Zhou, 2010] X. Zhou, C. Hu, X. Hu, T. Peng, and J. Qu, *Phys. Chem. C.*, **114**, 2746 (2010).
[R. L. Zong, 2004] R. L. Zong, J. Zhou, Q. Li, B. Du, B. Li, M. Fu, X. Qi, L. Li, and S. Buddhudu*, J. Phys. Chem. B.***, 108**, 16713 (2004).

Acknowledgement

I would like to express my gratitude to all those who helped me to complete this paper.

First of all, I would like to thank Professor Hasegawa for giving me an opportunity to study plasmonic nanocomposite materials and sparing his time for discussions about this study with informative suggestions. I also appreciate to Dr. Chikamatsu, Dr. Hirose, Professor Fukumura and Dr. Nakao for their advices in thin film fabrication, and to Dr. Kamisaka for instructing me the theoretical approach in ab initio calculation. I'd like to thank Dr. Ikemiya for discussions and coaching me PLD skills. Members of Hasegawa Laboratory also helped me.

I am deeply grateful to Professor Misawa, Professor Ueno in Hokkaido University, who gave me fruitful discussions and a lot of precious advices. Their instructions were essential to this work. I also profoundly thank to members of Misawa Laboratory. During my stay in Misawa Laboratory for experiments, Dr. Oshikiri, Dr. Uehara and Dr. Shi gave me suggestions in optical measurements. Mr. Kotake and Mr. Kamata always helped me to collect data smoothly and had animated discussions for me. I also want to thank Professor Hatanaka in Academia Sinica for instructing me the basics of plasmonic field when I started this research.

I owe important debt to instructors in Research Hub for Advanced Nano Characterization. Especially, Mr. Ito patiently supported me for a year when I acquired TEM sample making skills, even if I failed many times. I also profoundly thank to Mr. Hoshi, who instructed me about TEM measurements both theoretically and technically, and his points of views often enlightened me during discussions. Dr. Tsunakawa, Mr. Ibe, Dr. Matsumoto, and Mr. Oshikawa gave me many advices in both TEM measurements and TEM sample making. Dr. Tohei and Dr. Kumamoto supported me technically in measurements using JEM-2800. Mr. Ohtsuka, Mr. Kakegawa, and Mr. Moroyama helped me and encouraged me during SEM measurements.

I would like to thank Dr. Kusamoto in Nishihara Laboratory for letting me use the electrochemical setup and his kind supports during measurements. I also appreciate Dr. Sakae and Mr. Kato in Analytical Chemistry Student Laboratory,

School of Engineering, giving me tutorials and technical advices in ICP measurements.

I also want to express thanks to professor Wright of Academic English for Chemistry course, for his through and enthusiastic coaching on scientific English writing.

Finally, I would like to give my special thanks to my families who supported me for a long time with tolerant love. My husband not only encouraged me but also gave me scientific suggestions in physics and optics throughout of this work. My parents always cheered me up and supported my long student life both mentally and financially.